CHALMERS
UNIVERSITY OF TECHNOLOGY

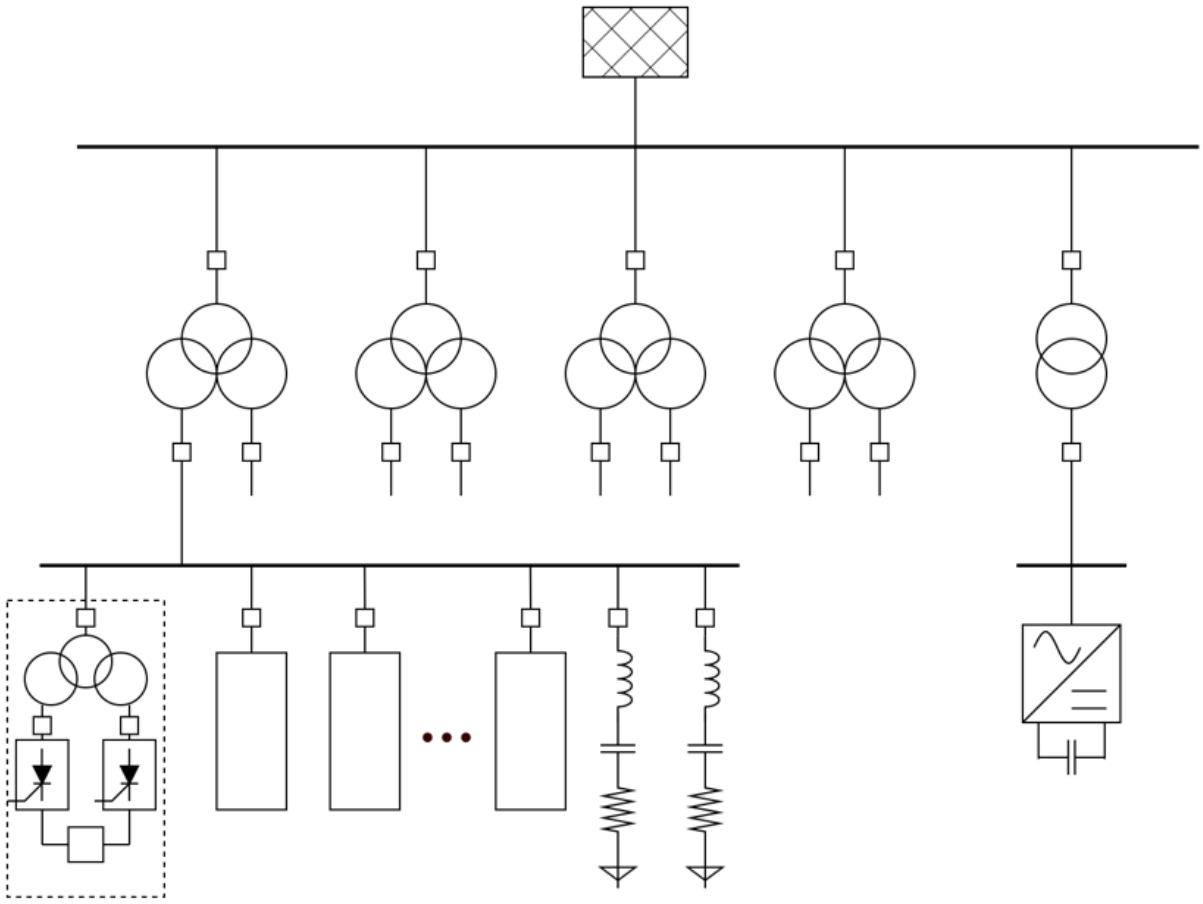

Power Grid Integration of GigaWatt-scale Hydrogen Production

Master of Science Thesis

ENRIQUE VAN DYKE

Department of Electrical Engineering
Division of Electric Power Engineering
Chalmers University of Technology
Gothenburg, Sweden 2024
www.chalmers.se

Master's thesis 2024

POWER GRID INTEGRATION OF GIGAWATT-SCALE HYDROGEN PRODUCTION

ENRIQUE VAN DYKE

CHALMERS
UNIVERSITY OF TECHNOLOGY

Department of Electrical Engineering
Division of Electric Power Engineering
Chalmers University of Technology
Gothenburg, Sweden 2024

Design and analysis of industrial power plant with sets of electrolyzers that reach GigaWatt-scale

ENRIQUE VAN DYKE

Supervisor: Tarik Dervišić, Hitachi Energy
Examiner: Massimo Bongiorno, Electrical Engineering Department

Master's Thesis 2024
Department of Electrical Engineering
Division of Electric Power Engineering
Chalmers University of Technology
SE-412 96 Gothenburg
Telephone +46 31 772 1000

Typeset in LaTeX
Printed by Chalmers Reproservice
Gothenburg, Sweden 2024

Power Grid Integration of GigaWatt-scale Hydrogen Production
ENRIQUE VAN DYKE
Department of Electrical Engineering
Division of Electric Power Engineering
Chalmers University of Technology

Abstract

Climate change is one of the most pressing issues that humanity faces today. The urgent need to mitigate green-house gas emissions has triggered an unprecedented expansion of renewable energy sources, consequently, creating an opportunity to revolutionize our energy systems. In this context, green hydrogen emerges as a potential candidate to decarbonize hard-to-electrify industries, such as iron & steel, high-temperature heat applications, petrochemical, transport and aerospace sector.

This thesis endeavors to explore the technical feasibility of gigawatt scale hydrogen production by examining a proposal of plant design, implementing a model for electrolyzer systems available in the market and selecting an AC/DC topology for the rectifier.

The elected station is connected to the HVAC transmission grid through a step-down distribution system with two voltage levels, 400 and 33 kV. This grid is assumed to have a high short circuit capacity given the high demand of power and its design needs to comply with grid code requirements and international standards (IEC, IEEE).

The driver for standardization and cost savings, while matching electrolyzer's technology with adequate electrical infrastructure, led to the decision of implementing alkaline water electrolyzers. Besides, an accurate model definition required a solid understanding of the electrical and thermal fundamentals of electrolysis.

The electrolyzer voltage and current requirements defined the criteria for selecting the converter's topology. The final choice was the 12-pulse thyristor rectifier given its high efficiency, reliability and good control of the current. Low-order harmonic cancellation excluding those harmonic orders with $12h\pm1$ with $h = 1, 2, 3 ...$ was an attractive feature, but required the use of tuned-LC filters for the 11th-13th and 23rd-25th harmonics.

A look-up table is implemented for the electrolyzer model next with a per-unit current controller for the 12-pulse thyristor rectifier. This set-up makes it easily reimplementable in future projects, since it enables the implementation of this controller for any electrolyzer system, independently of its specifications. All models and simulations are performed using the power system analysis software DIgSILENT PowerFactory.

Finally, the correct rating of different components used in the station and grid code compliance was verified performing different simulations: a load flow analysis, a dynamic ramp-up simulation to nominal capacity and lastly transient analysis of the station in spontaneous events like load rejection.

Keywords: electrolyzer, alkaline, model, hydrogen, GW-scale, 12-PTR, station

Acknowledgements

First and foremost, I would like to express my sincere gratitude to my supervisor Tarik Dervišić for his dedication and support during the realization of this thesis. Also, for his invaluable patience and feedback. Additionally, this endeavor would not have been possible without my examiner Massimo Bongiorno, who generously provided feedback and his expertise in the subject.

I would also like to thank Björn Wickman for an insightful discussion on the electric properties of fuel cells and electrolyzers, which was ultimately key in helping me build the electrolyser modelling. I am also grateful to my colleague, Shemsedin who provided guidance, introduced me to the PowerFactory modelling tool and provided moral support.

Special thank you to my work managers Joachim Andersson, Fredrik Sjögren and Leila Manshaei who were always helpful and kindly offered their time to discuss a myriad of topics but above all inspired me and provided personal advice.

A big shoutout to my whole Hitachi Energy's Power Consulting team in Gothenburg, especially Emily Baruffaldi and Kelly Antoniadou, without whom this would not have been possible.

Many thanks to my family and friends. To my parents, for their invaluable guidance and belief in me, my grandmother for her kind spirit and my sister Graciela for her priceless support, enthusiasm and editing skills. To my friends Lander Vallejo and Gaizka Barrasa for their late night feedback sessions and empathy. Lastly, I want to express my heartfelt gratitude to Laura Martinez de Guinea, who stood by my side during the final completion of this thesis. I cannot emphasize enough how much I owe you for your kind support and help.

Enrique Van Dyke, Gothenburg, August 2024

Contents

List of Figures

List of Tables

List of Acronyms

Below is the list of acronyms that have been used throughout this thesis listed in alphabetical order:

AEM	Anion Exchange Membrane
AWE	Alkaline Water Electrolyzer
BP	Band Pass
CAPEX	Capital Expenditure
CCUS	Carbon Capture, Utilization and Storage
CHP	Combined Heat and Power
CV	Control Volume
DCC	Demand Connection Code
GDL	Gas Diffusion Layer
GW	Giga Watt
H2	Hydrogen
HTE	High Temperature Electrolyzer
HVAC	High Voltage Alternating Current
HVDC	High Voltage Direct Current
IEA	International Energy Agency
IEC	International Electrotechnical Commission
IEEE	Institute of Electrical and Electronics Engineers
IGBT	Insulated-Gate Bipolar Transistor
IMC	Internal Model Controller
kW	Kilo Watt
LCOE	Levelized Cost of Electricity
LCOH	Levelized Cost of Hydrogen
MEA	Membrane Electrode Assembly
MW	Mega Watt
PCC	Point of Common Coupling
PEM	Proton Exchange Membrane
PFSA	Perfluorosulfonic acid
PF	Power Factor
PI	Proportional-Integral
PLL	Phase-Locked Loop
PTL	Porous Transport Layer
POX	Partial Oxidation
PTR	Pulse Thyristor Rectifier

PWM	Pulse Width Modulation
RMS	Root Mean Square
SLD	Single line diagram
SMR	Steam Methane Reforming
SPE	Solid Polymer Electrolyte
SOE	Solid Oxide Electrolyzer
STATCOM	Static Synchronous Compensator
SVC	Static VAr Compensator
TDD	Total Demand Distortion
THD	Total Harmonic Distortion
VSC	Voltage Source Converter

Nomenclature

Below is the nomenclature of parameters and variables that have been used throughout this thesis.

Variables

E_r, E_{th}	Reversible and Thermoneutral Potential	V
E_{cell}, E_{loss}	Cell voltage and over-voltage	V
T	Temperature	K
P	Pressure	bar
Δh	Net specific enthalpy	kJ mol^{-1}
Δg	Net specific Gibbs energy	kJ mol^{-1}
Δs	Net specific entropy	J $(mol\ K)^{-1}$
h_f^o	Standard enthalpy of formation	kJ mol^{-1}
h	Specific enthalpy (T, P)	kJ mol^{-1}
h^o	Standard specific enthalpy	kJ mol^{-1}
s	Specific entropy (T, P)	J $(mol\ K)^{-1}$
s_{gen}	Specific generated entropy	J $(mol\ K)^{-1}$
q_{CV}	Specific heat transfer	kJ mol^{-1}
w_{CV}	Specific work	kJ mol^{-1}
z	Number of electron moles	-
F	Faraday constant	C mol^{-1}
R	Universal gas constant	J $(mol \cdot K)^{-1}$
ΔN	Net number of gaseous moles	-
J_{cell}	Cell current density	A m^{-2}
$J_{0,an}, J_{0,ca}$	Anode and cathode exchange current density	A m^{-2}
η_F	Faraday or current efficiency	-
$\dot{m}_{H_2}, \dot{m}_{ideal,H_2}$	Real and ideal hydrogen mass flow	kg/s
M_{H_2}	Hydrogen molecular weight	kg mol^{-1}
n_{series}	Number of electron moles	-
r_1	Ohmic parameter 1	$\Omega\ m^2$
r_2	Ohmic parameter 2	$\Omega\ m^2/^oC$
s	Coefficient of electrode overvoltage	V
t_1	Overvoltage coefficient 1	m^2/A
t_2	Overvoltage coefficient 2	$m^2\ ^oC/A$
t_3	Overvoltage coefficient 3	$m^2\ ^oC^2/A$
a_1	Faraday efficiency coefficient 1	%

a_2	Faraday efficiency coefficient 2	A/m^2
a_3	Faraday efficiency coefficient 3	$A\ (m^2\ ^oC)^{-1}$
a_4	Faraday efficiency coefficient 4	A^2/m^4
a_5	Faraday efficiency coefficient 5	$A^2(m^4\ ^oC)^{-1}$
α	Firing angle	rad
L_c	Commutation inductance	mH
V_{d0}	Ideal no-load DC voltage	V
ΔV_d	Voltage drop in the commutation reactance	V
V_d	6-PTR DC voltage	V
V_{LL}	RMS line to line voltage	V
I_d	6-PTR DC current	A
$\hat{I}_{A(1)}$	Peak fundamental current	A
$\hat{I}_{A(h)}$	Peak current for its corresponding harmonic order	A
h	Harmonic order	-
R_{load}	Electrolyzer equivalent resistance	Ω
r_{load}	Electrolyzer equivalent resistance in per unit	pu
L_{load}	Electrolyzer equivalent inductance	mH
l_{load}	Electrolyzer equivalent inductance in per unit	pu
R_{base}	Electrolyzer base resistance	Ω
t_{rise}	Rise time	s
K_P	Controller integration constant	-
K_I	Controller proportional constant	-
α_c	Bandwidth	rad/s
i_{ref}	Reference current	pu
V_{bus}	Bus voltage of the electrolyzer systems	kV
$I_{n,bus}$	Nominal bus current of electrolyzer systems	kA
I_{SCC}	Short-circuit current	kA
$S_{n,T}$	Rated apparent power of transformers	MVA
$N_{sys,total}$	Total number of electrolyzer systems	-
$N_{sys,branch}$	Number of electrolyzer systems per branch	-
$P_{n,station}$	Total station active power capacity	MW
$P_{n,sys}$	Individual active power demand of each electrolyzer system	MW
$S_{n,branch}$	Apparent power demand from each transformer branch	MVA
$S_{n,sys}$	Individual apparent power demand of each electrolyzer system	MVA
$S_k^{''}$	Grid's short-circuit capacity	MVA
$I_k^{''}$	Grid's short-circuit current	kA
$\bar{Z}_1$	Grid's Thevenin positive sequence impedance	Ω
R_1	Grid's Thevenin resistance	Ω
X_1	Grid's Thevenin reactance	Ω
U_{nom}	Grid's nominal voltage	kV
$S_{n,2TR}$	Rated apparent power of 33/3.11kV transformers	MVA
$S_{n,3TR}$	Rated apparent power of 400/33kV 3-winding transformers	MVA
$\cos\varphi_{sys}$	Electrolyzer system power factor	-
Q_f	Filter rated reactive power	MVAr

V_f	Filter rated voltage	kV
f_r	Filter resonant frequency	Hz
q	Filter quality factor	-
X_L, X_C	Filter inductive and capacitive reactances	Ω
L_f, C_f, R_f	Filter inductance, capacitance and resistance	mH,µF,Ω
Q_{max}, Q_{min}	Station maximum and minimum reactive power demand	MVAr
Q_{st}	STATCOM rated reactive power	MVAr
$Q_{3TR,max}$	Maximum reactive power flow through 400/33kV 3-winding transformer	MVAr
$Q_{3TR,min}$	Minimum reactive power flow through 400/33kV 3-winding transformer	MVAr

1

Introduction

Climate change is one of the biggest challenges that humanity faces in the 21st century. Continuous escalation of greenhouse gas (GHG) emissions caused by technology development, population growth and well-being improvement since the First Industrial Revolution has become a global threat to international security and stability [1].

Although the first world conference about the environment was in 1972 held by the United Nations in Stockholm [2], it was not until 1997 when the first international agreement for reducing GHG emissions was adopted: the Kyoto Protocol. In this treaty [3], the different parties recognized that global warming was happening and that human-source CO_2 emissions were causing it. This delay was caused by disinformation, uncertainty and conflicts of interest in the matter. For example, in the 70's ExxonMobil publicly misled climate science while simultaneously having internal assessments forecasting a continuous increase in global temperatures [4], [5]. After that came the well-known Paris Agreement in 2015, where all parties committed to reduce their emissions with differences between developing and developed countries. The headline of the agreement was to avoid a global temperature increase below 2°C, preferably 1.5°C, compared to pre-industrial levels and reaching a zero emissions scenario by 2050 [6].

Since then, some major events happened like USA withdrawal from Paris Agreement in 2017 during Donald Trump's Presidency [7] and its return in 2021 with Joe Biden [8]. COVID19 prompted a temporary reduction in carbon emissions [9]. In 2022, Russia's invasion of Ukraine accelerated the energy crisis in Europe, pressing on oil and gas supplies already stressed due to the fast recovery of the economy post-pandemic [10] and finally, pending to see the effects of the Israel-Gaza conflict currently underway.

China has led the growth in energy demand worldwide during the last two decades with its subsequent repercussion in CO_2 emissions. However in 2023, China's population growth came to a halt [11] whilst India will surpass it by 2025 [12]. This shift joined with India's industrialization represents an opportunity to reduce CO_2 emissions as India increases its share of renewables (35% by 2030, 15% PV solar[13]) and adopts cleaner energy practices and sustainable development strategies.

The Paris Agreement led to increased investment in renewable energy and energy efficiency measures, including electrification of transportation, industry, and buildings. This electrification trend led to a wave of deployment of electric vehicles and the growth of renewable energy sources such as wind and solar power, which has contributed actively to reduce GHG emissions. However, there are specific sectors and activities where emissions are significant and electrification is not always the way to go, such as agriculture and the

chemical, cement, steel and aerospace industries. This is where hydrogen comes in and plays a key role in the green and sustainable energy system of the future.

According to the International Energy Agency (IEA) [14], electricity and heat generation accounted for roughly 40% of total emissions in 2022, transport 23%, industry 23%, buildings 10% and other activities 5%. From industry [15], iron & steel account for 28%, cement 27% and petrochemical 15%. Hydrogen has a great potential to substitute fossil fuels in many of these sectors such as iron & steel, petrochemical and transport.

Global hydrogen demand reached 94 megatonnes (Mt) in 2021 where 42% was employed in refining, 36% in ammonia production, 16% in methanol production and 6% in iron & steel production [16]. Unfortunately, as it is shown in the "current status of hydrogen production" of the Global Hydrogen Review 2022 [17], natural gas is the main route to produce hydrogen via steam methane reforming (SMR) representing 62%. The second major contributor is coal via Partial Oxidation (POX) accounted for 19%, practice mainly done in China, and lastly hydrogen as by-product of reforming at refineries 18%.

Overall, 99% of all hydrogen produced in 2021 came from fossil-fuel sources, while low-emission hydrogen only accounted for 1 Mt (0.7%), from which almost all was fossil fuels with carbon capture, utilization and storage (CCUS), with only 35 kilotons (kt) of hydrogen produced from electricity via water electrolysis. The reason why hydrogen is almost entirely produced using fossil fuels is because it is extremely cheap. According to a publication made by S&P [18], the actual cost of fossil fuel-based hydrogen is around 1.80$/kg. Blue hydrogen produced with SMR and CCUS is around 2.40 $/kg. By the other hand, green hydrogen produced with renewable resources costs between 3 $/kg and 6.55 $/kg, according to the European Commission hydrogen strategy [19].

Consequently, the main challenge for water electrolysis is to reduce its levelized cost of production (LCOH). Three key factors are necessary in order to produce cheap green hydrogen: reduce the capital expenditure (CAPEX) of the electrolyzer plant, improve electrolyzer stack efficiency and most importantly to use renewable energy with low levelized cost of electricity (LCOE).

The great need for sustainable energy storage solutions to replace high energy density fossil fuels is another factor that drives a lot of attention. Green hydrogen is an energy vector with very desirable properties such as high energy density, versatility and abundance.

There are several ways of producing hydrogen. The most popular methods have already been mentioned, but there are two other technologies to produce sustainable hydrogen that are worth mentioning since they could help expand hydrogen infrastructure: Plasma Enhanced Gasification [20] and High Temperature Gas-cooled Reactor [21].

Today's total energy supply according to World Energy Outlook 2022 developed by IEA [13] is 624.2 EJ. This value is expected to increase by 18.55% by 2050 following Stated Policies Scenario (STEPS) scenario. From this increase, the International Renewable Energy Agency (IRENA) estimates that in order to keep a 1.5°C scenario in 2050, 10% of the final energy demand must be supplied by hydrogen accounting for 74 EJ per year [22], equivalent to 600 Mt of hydrogen per annum, 6 times todays' hydrogen supply. This escalation is already being pushed forward by the energy crisis 2021-2023, which promises to become a historic turning point towards a cleaner and more secure energy system [23].

The main contributors for hydrogen escalation are growth in policy support boosted by Europe's post–COVID-19 recovery plan, and increase in gas natural prices boosted by Russia's invasion of Ukraine [10]. These 2 main factors provide economic, climate and security arguments to invest in cost-competitive and sustainable technologies, creating a positive outcome for humanity and the environment.

At today's date the largest electrolyzer hydrogen production site is being constructed in China by Sinopec with a total production capacity of 300 MW, connected to a photovoltaic power plant. This plant will be able to produce 20 kt of H_2 per year after its entry in operation in June 2023 [24]. By contrast the biggest single stack electrolyzer constructed so far is commissioned by HydrogenPro in Herøya, Norway, capable of producing 850 tons of H_2 per year [25], with an equivalent power input of 5 MW.

1.1 Aim

The main objective of this master thesis is to design and model a GW-scale electrolyzer station using a single electrolyzer technology as well as perform steady-state and dynamic simulations to ensure adequate, safe, reliable and uninterruptible hydrogen supply.

The electrochemical principals behind hydrogen electrolyzers are reviewed in order to develop a solid virtual twin of the device. The basic load of the station is a 1.9 MW electrolyzer, which is connected into modules, forming bigger loads and enabling a GW-scale plant. As any other electrified industry, the station is connected to the transmission grid, so grid code compliance is considered in the design.

1.2 Problem Description

Green hydrogen production anticipates to grow considerably in the coming years. The objective of covering 12% of 2050 total energy supply with sustainable hydrogen stated by IRENA [22] implies the installed capacity of electrolyzers to increase from 510 MW today to 720 GW in 2030 and 3670 GW in 2050 according to IEA [13]. This expansion is expected to be accompanied with its corresponding enlargement in renewable energy installed capacity [22].

If these projections were accomplished, it means a rise of annual manufacturing capacity production to at least 60 GW by 2030. Based on these assessments, GW-scale electrolyzer stations can become a reality in the coming years. Thus, it is of interest to get a deeper understanding of large-scale electrolyzer stations and analyze their technical feasibility.

Besides, these power stations must meet grid code requirements while at the same time be competitive from an economical point of view. Hence the purpose of this master thesis is to verify the first statement. Thanks to cheap renewable energy and technology development in 2050, it is assumed that the second statement will also be fulfilled, since the main operating cost of hydrogen is electricity cost [26].

1.3 Scope

The thesis begins by examining the current state of electrolyzer technology. It provides a technology classification based on the operating temperature and electrolyte, comparing materials used, performance, and technological maturity. Notably, the focus of the thesis is on AWE and PEM electrolyzers, which are the most established and developed in terms of technology maturity and commercial development. Therefore, these two types are the main subjects of further benchmarking and analysis.

From the outset, it is important to clearly define the boundaries and the complexity of the model. An electrolyzer stack needs a broad infrastructure to operate: electrical power supply, AC/DC converter, water and gas treatment systems, compressor, and hydrogen storage. Nevertheless, the thesis scope covers only the first two components. Besides, an accurate model of the electrolyzer demands an electrical and thermal model. However, due to the project's focus on the electrical aspects, the thermal dynamics are omitted in this project, and only operation at constant temperature is considered.

A power electronics study identified the most relevant converter topologies for electrolyzer applications. After selecting the 12-pulse thyristor rectifier and studying its working principle, the converter's Electromagnetic Transient (EMT) analysis was left out of the scope. Afterward, the controller implementation is carried out through a system analysis of the converter-electrolyzer interaction using only RMS simulation and average value calculations on the DC side.

Station design for the GW-scale electrolyzer plant included evaluating different station proposals available in two main projects. These single-line diagrams (SLD) are all connected to the High Voltage (HV) transmission grid through a 400 kV Point of Common Coupling (PCC). These diagrams differ in the bus voltage levels inside the station, the transformers' power rating, and the parallel connection of the HV transformers. Finally, only one candidate is proposed for further analysis and simulation.

A subsection states the grid code requirements that an industry must comply with so the Transmission System Operator (Svenska Kraftnät) allows its connection to the HV grid. Several documentation sources, like the Demand Connection Code (DCC), IEEE, and IEC standards for harmonic distortion, were considered. The covered grid code compliance categories are harmonics and distortions, power factor correction, and voltage regulation.

Station design included selecting and rating HV components such as transformers, filters, converters, and reactive power compensation devices. However, this project excluded switchgear selection, so no short-circuit analysis or protection coordination studies were carried out. This also led to the implementation of a single busbar for Point of Common Coupling (PCC) instead of more complex substation schemes like sectionalized single busbars or double busbars.

Afterward, the station operation is tested in multiple scenarios. For example, its design is validated in a steady state through a load flow analysis, its dynamic operation is achieved through a ramp-up simulation, and its voltage regulation capabilities are demonstrated through load rejection events. Voltage variations at the PCC were excluded to reduce the number of simulations. Lastly, the economic evaluation of this project is left outside of the scope, mainly focused on the technical feasibility.

1.4 Societal, ethical and ecological aspects

The environmental benefit of substituting "grey and black" hydrogen with clean green hydrogen is clear: it creatively addresses hard-to-electrify sectors in the climate crisis. Nevertheless, it is necessary to consider its societal consequences and ethical dilemmas.

First, a direct consequence of the clean energy transition is an employment shift. Industries in power generation, renewables, power grid, energy efficiency, e-fuels, and biogas expect unparalleled growth. Contrarily, Big Oil & Gas corporations face a loss of profits that echos into a loss of employment unless a purpose shift is implemented. However, some of these emerging sectors including hydrogen production offer a good opportunity for job relocation of those dedicated to the fossil-fuel industry today [27].

An example at national perspective of how this could be achieved is Norway's vision for decarbonization. In 2022, Norwegian petroleum export revenues were roughly 50%, supplying 25% of Europe's oil and natural gas demand. Norway intends to cut emissions to 80-95% by 2050 [28], with hydrogen playing a key role [29].

Secondly, clean water consumption is another factor to consider, since it is a globally valued resource and is very scarce in some countries. Increase of clean water demand due to massive hydrogen electrolyzers adoption might cause inequality and unfair distribution within semiarid-desertic countries where fresh-water availability is an issue.

According to UN [30], as of today, more than 2 billion people live in countries experiencing high water stress that might exacerbate with population growth and climate change effects. To ensure reliable water supply in the coming years, these countries expect to expand their water management infrastructure, especially sea water purification and wastewater management [31]. This might ensure water availability, but depreciate hydrogen supply. Nonetheless, the solution could be the use of solar radiation in semiarid-desertic countries where PV and solar-thermal energy are cheap sources of electricity. Chile, for example, could be a good proof of concept since it has the driest nonpolar desert in the world (Atacama Desert) and water scarcity issues. Despite this, its government presented in 2020 its ambitious National Green Hydrogen Strategy [32] which aims to produce world's cheapest green hydrogen by 2030.

Thirdly, some fuel cells and electrolyzers technologies require rare-earth metals. Iridium and platinum electrodes are widely used in commercial electrolyzers which poses an unsustainable practice in the long term since they are considered as "endangered" species among metals [33]. Naturally, new catalysts might appear in the market as technology develops. For example, a 2022 study [34] by RIKEN CSRS in Japan found a rare metal-free catalyst based on Co_2MnO_4, lasting around 1500 hours with a current density of 0.2 A/cm^2. This performance is superior to other non-rare metal catalysts; although it still stays behind iridium catalysts with longer lifetimes.

Lastly, safety guidelines and protocols are crucial to consider when using hydrogen due to its flammability and explosiveness, though it is non-toxic compound that rapidly dissipates in case of leak [35]. The Hydrogen tools report [36] discusses potential incident scenarios and appropriate prevention and mitigation measures.

1.5 Method

The benchmarking between AWE and PEM begins with an individual technology description, emphasizing their fundamental differences. All key performance indicators are summarized and tabulated, and a decision is made to implement one of the technologies for the GW-scale station.

Creating an accurate model was a meticulous process that required a deep understanding of the electrical and thermal basics of electrolysis. This thoroughness translated into a comprehensive scientific literature review covering thermodynamics, electrochemistry, and energy systems modeling. These topics are important because they impact the stack efficiency and current-voltage characteristics.

The technical specifications for a commercial MW-scale electrolyzer, such as current-voltage characteristics, were unavailable. Therefore, the MW-scale electrolyzer model was derived from the performance of the PHOEBUS plant kW-scale electrolyzer. Adjustments were made to design parameters such as electrode effective area and number of cells in series to match the hydrogen production rate and power input requirements of the Nel Hydrogen A485-stack while ensuring compliance with the maximum rating limitations. Subsequent power upgrades like larger modular units (A3880) provided by Nel Hydrogen, and load agglomeration enabled the simulation of larger equivalent loads.

The current controller design follows the Internal Model Control (IMC) tuning method, and the system analysis includes a temperature test and ramp-up sequence test with different tuned control parameters. The controller is designed per unit, ensuring its universal implementation independently of the electrolyzer ratings, thereby providing reassurance about its adaptability.

All simulations are conducted using the power system software PowerFactory (DIgSILENT). It is considered a solid power system analysis software similar to PSS/E and PSCAD. Proficient in RMS simulations with an extensive and comprehensive library of components while combining various power system analysis tools within one platform. In contrast, PSS/E presents a steeper learning curve and less flexibility than PowerFactory, making it a less attractive option. PSCAD, while excellent for detailed electromagnetic transient (EMT) simulations, is not a good choice for RMS simulations and larger-scale stability studies such as PowerFactory.

The electrical component rating process involved two stages: an initial rating determined through simplified calculations, followed by validation through load flow calculations and dynamic simulations such as ramp-up sequences and load rejection studies.

For grid code compliance, every category is validated through specific studies and the implementation of necessary equipment. Harmonic distortion is evaluated through a harmonic analysis and fulfilled through implementing passive filters. Power Factor Correction is evaluated through a load flow analysis and ramp-up sequence, where a combination of capacitor banks and MVAr compensators maintain a null exchange of reactive power with the grid. Finally, voltage regulation requirements are accomplished by implementing a STATCOM at PCC, and its performance is reviewed through load rejection studies.

2

State of the art

Water electrolysis is a chemical reaction occurring within an insulating container filled with water. This aqueous solution must increase its electrical conductivity in order to allow a free transfer of ions, so a soluble salt or ionic compound, such as potassium, sodium, or bicarbonate, is added. This combination with water forms an electrolyte, creating an alkaline medium that serves as a conductive environment for ions. Then two electrodes are introduced into the container and submerged in this aqueous phase. Upon applying a voltage difference across both electrodes, a redox reaction occurs, leading to the splitting of water into its fundamental elements: hydrogen and oxygen.

$$H_2\,O\,(l) \longrightarrow H_2\,(g) + \tfrac{1}{2}\,O_2\,(g)$$

Electrolysis concept is a straightforward procedure, but the chemical (electrodes, electrolyte) and operating (temperature and pressure) conditions in which it happens vary considerably depending on the technology. It can be classified according to their electrolyte, charge carrier, operating temperature etc. The number of experimental technologies is extensive as well, however, the attention will be focused only on the most mature. In Figure 2.1, it is shown a popular classification of electrolyzer technologies according to their electrolyte type and operating temperature.

High-temperature electrolyzers (HTE) present big advantages against low-temperature technologies in terms of efficiency. Since electrolysis occurs at high temperatures, water is present in steam phase, which decreases the reaction net exchange enthalpy and Gibbs-free energy. This results in a lower energy input into the reaction which results in higher efficiency. Nevertheless, this high temperature operating range is impractical for universal application, which results only interesting for intensive-energy industries like iron&steel or traditional thermal plants like geothermal, nuclear or CHP. Besides its technology is still in R&D phase compared to low-temperature electrolyzers.

A comparison of the efficiencies, materials used, technology maturity and expected number of hours of operation is described in Table 2.1. In terms of technology maturity and commercial development, only AWE and PEM electrolyzers are fully established and developed, so only these will be subject of further discussion and analysis.

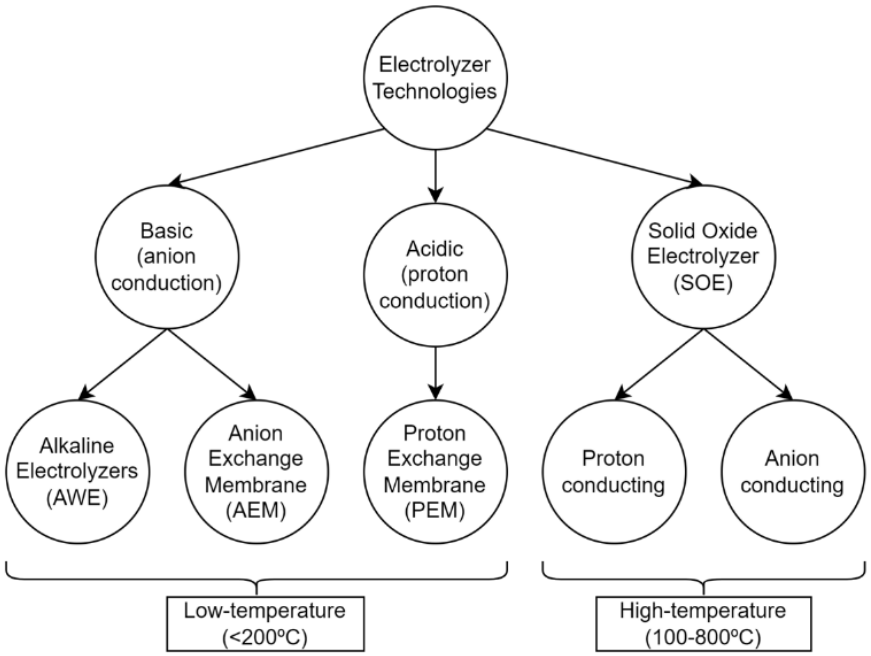

Figure 2.1: Electrolyzer classification according to electrolyte and operating temperature.

Table 2.1: Water Electrolysis Technology Description [37],[38],[39].

Parameter	AWE	PEM	AEM	SOE
Charge carrier	OH^-	H^+	OH^-	O^{2-}
Electrolyte	20–40 wt% KOH /NaOH	Solid polymer electrolyte (PFSA)	DVB polymer with 1M KOH/NaOH	Yttria stabilized Zirconia (YSZ)
Anode	Nickel coated stainless steel	IrO_2, RuO_2	NiFeCo alloys	Perovskites (LSCF, LSM)
Cathode	Nickel coated stainless steel	Platinum carbon	Nickel	Ni/YSZ
Separator	Asbestos/Zirfon	Nafion	Fumatech	Solid electrolyte YSZ
Gas Diffusion layer	Nickel mesh	Titanium mesh /carbon cloth	Nickel foam /carbon cloth	Nickel mesh /foam
Bipolar Plates	Ni-coated stainless steel	Pt/Au-coated titanium	Ni-coated stainless steel	Co-coated stainless steel
Current density	0.2–0.8 A cm^2	1–2 A cm^2	0.2–2 A cm^2	0.3–1 A cm^2
Cell Area	<3 m^2	<0.15 m^2	<0.03 m^2	<0.02 m^2
Voltage efficiency	50-78% (LHV)	50-83% (LHV)	50–59% (LHV)	89% (LHV)
Specific stack energy consumption	4.2–4.8 kWh/Nm^3	4.4–5.0 kWh/Nm^3	-	3.4 kWh/Nm^3
Temperature limits	70–90 °C	50–80 °C	40–60 °C	700–850 °C
Gas pressure	1–10 bar	15–30 bar	<30 bar	1 bar
Lifetime stack	(60-90) 000 h	(50-80) 000 h	30 000 h	20 000 h
Lifetime system	20–30 years	10–20 years	-	-
Development status	Mature	Commercialized	R&D	R&D

2.1 Alkaline Water Electrolyzer (AWE)

Alkaline electrolyzers are considered the most mature option in the market today. Its large development began in the 1920s and 1930s with the expansion of the chemical industry [40], providing several decades of refinement and optimization, contributing to their established reputation as a reliable and well-understood choice for hydrogen production.

They are characterized by using an alkaline electrolyte, typically, potassium hydroxide with a concentration between 25-30% where it reaches its maximum conductivity at 80°C [41]. This salt dissolved in water increases its pH forming a basic aqueous phase with free hydroxide ions. To separate both electrodes typically a 252-463 µm Zirfon diaphragm soaked with KOH solution is employed [38],[42]. Then, these are pressed onto the separator following a zero-gap cell design [43], reducing the surface-specific cell resistance. These electrodes are typically stainless steel plates with nickel alloy coating. Nickel (Ni) is frequently used due to its catalytic activity, corrosion resistance, conductivity, but most importantly because of its availability, low cost and proven stability in high pH mediums.

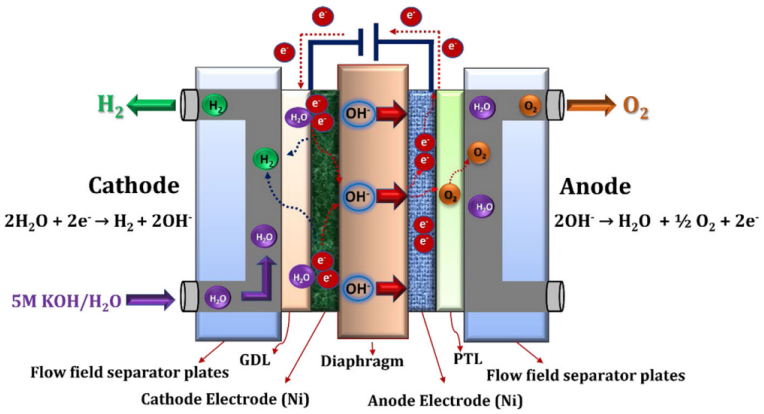

Figure 2.2: AWE cell working principle [37].

In Figure 2.3, it is shown the typical system infrastructure required for the AWE operation [44]. The electrolyte circuit (grey) consists of two gas separators, where the excess fluid is recovered and reintroduced into the circuit. In the H_2 piping network (purple), a scrubber, deoxidizer and dryer are used to remove traces of electrolyte and water, while improving the gas purity. Besides, since most AWE work at low pressure, a compressor is usually added before the process or a storage tank ahead to increase the delivery pressure.

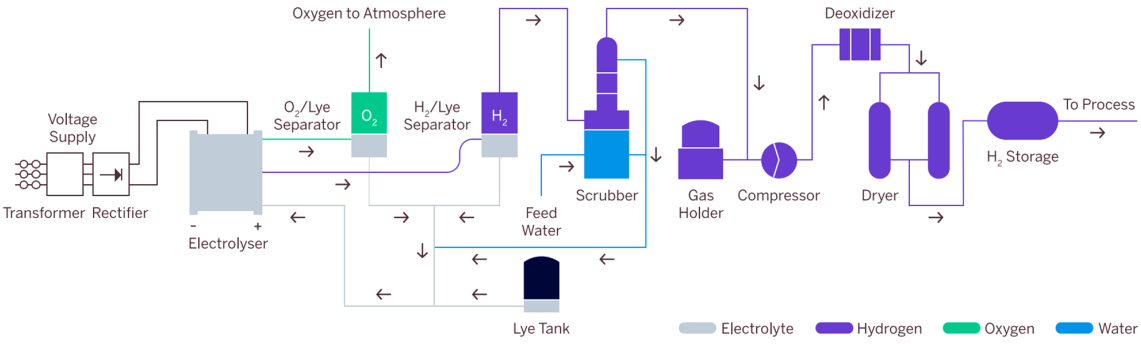

Figure 2.3: Typical AWE system architecture [44].

2.2 Proton Exchange Membrane Electrolyzer (PEM)

PEM technology emerged as an alternative to AWE for hydrogen production in mid-20th century. A breakthrough in ion-conducting membranes occurred in the late 1960s with Dr. Walther G. Grot's development of Nafion, a perfluorosulfonic acid (PFSA)-based copolymer membrane. This innovation paved the way for PEM fuel cells and electrolyzers, whose main driver was the possibility to generate oxygen with high differential pressure, which was an indispensable tool for aerospace and submarine life support applications[40].

Overall, PEM's key advantage lies in utilizing a solid polymer electrolyte (SPE). The most used SPE in the market today is still the Nafion ionomer family [45] with PFSA-membrane. Despite the corrosive environment, this technology employs durable catalysts, typically platinum (Pt) nanoparticles in the cathode and iridium oxide (IrO_2) nanoparticles in the anode. These particles are then integrated into carbon paper and sintered titanium plates forming the electrodes.

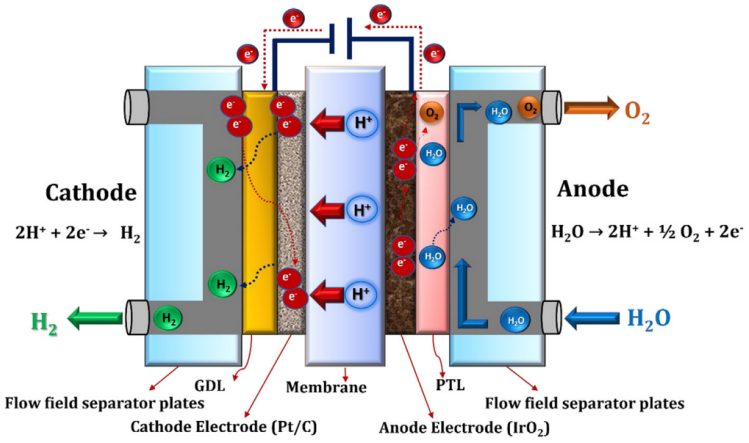

Figure 2.4: PEM cell working principle [37].

The resulting membrane electrode assembly (MEA) enables a significant advantage, since it has enough mechanical strength to allow differential pressure across the electrodes. In Figure 2.5, Nel Hydrogen provides schematics for PEM electrolyzer system infrastructure [44]. Here, hydrogen gas is generated at elevated pressures up to 30 barg which corresponds to the process delivery pressure. Oxygen gas is produced at pressures close to ambient.

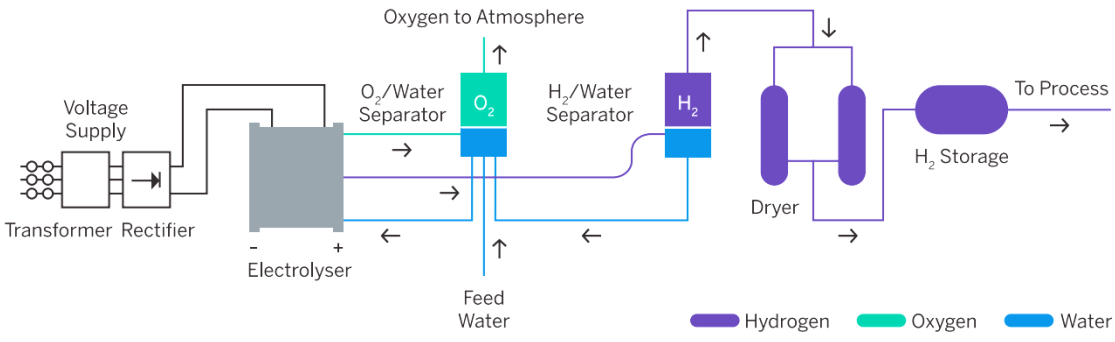

Figure 2.5: Typical PEM electrolyser system architecture [44].

2.3 Economic and Performance Evaluation

The most mature technologies available in the market have already been presented and its characteristics stated. Therefore, it is necessary to compare both technologies, understand their differences and also to ponder their advantages and disadvantages against their compatibility with the electric power source typology, the transmission connection either AC or DC and the scale of hydrogen production.

2.3.1 Investment costs

The first driver for building a station with such big dimensions as GW-scale is investment cost, long term stability and the possibility to implement large scale systems which should reduce the station's CAPEX.

Currently, the investment cost for AWE stands around 500–1000 USD/kW [37], [38] and the system's lifespan reaches between 60 000 - 90 000 hours [46]. In comparison, PEM boasts a stack lifetime of 50 000 - 80 000 hours with minimal performance decline [38]. The hydrogen production cost for PEM is between 700 and 1400 USD/kW [37], [38].

A key factor contributing to the higher cost of PEM compared to AWE is the elevated expense of cell components. PEM electrolyzers employ noble metals like IrO_2 in the anode and Pt in the cathode, which are more expensive than their counterpart Ni predominantly used in AWE technology. Not to mention the bipolar plates made of Pt/gold-coated titanium, which may account for 25% of total system capital cost [38]. To illustrate, a 1.9 MW PEM water electrolyzer operating at 2 A cm^{-2}, assuming an Ir loading of 5 mg cm^{-2} and Pt loading of 2 mg cm^{-2} [38], requires approximately 2.47 kg of Ir and 0.95 kg of Pt. The anticipated cost of the catalysts goes around 435 000 USD (147.5 USD/gram and 30 USD/gram respectively as of August 2023 [47]), which means 206.75 USD/kW and a 15% portion of CAPEX. In contrast, the cost of Ni fluctuates between 0.02 and 0.04 USD/gram as of 2020 to 2023 [47].

Finally there is the scale factor. According to Nel Hydrogen catalogue [44], it is offered stacks MC500 (PEM) and A485 (AWE), both units capable of generating 490 Nm^3/h. Afterwards, stacks can be mounted in series or parallel groups to reach higher production rates. In PEM technology two of the biggest systems available in the market are Silyzer 300 (Siemens) with 2 000 Nm^3/h and MC5000 (Nel Hydrogen) with 4 920 Nm^3/h [37]. On the AWE side, Nel Hydrogen offers an electrolyzer system A4000 with 3 880 Nm^3/h. After this comparison, it is logical to conclude that both technologies have similar economies of scale.

2.3.2 Operating conditions

If the operating conditions for both AWE and PEM is compared in Table 2.1, it is clear that both technologies do not operate at the same range. The great advantage of PEM technology is that it can operate at higher pressures than AWE, in the range of 30-70 barg as well as it enables differential pressure between anode and cathode. For example, in Nel Hydrogen catalogue [44], their example PEM Hydrogen plant works at 30 barg in the H_2 side and at almost atmospheric pressure in the O_2 side. This, however, may reduce the efficiency since it will require a thicker membrane to improve the mechanical stability [38].

In terms of temperature, both technologies work in similar ranges despite the difference of pressure. The low operating pressure for AWE usually requires a compressor downstream that increases the delivery pressure till even 200 barg [44].

Another detail to highlight is that PEM water re-circulation circuit requires only distilled and de-ionized water to operate, while AWE needs a separate circuit to re-mix the lye (potassium hydroxide) into the feed water supply, observe Figure 2.3. Nevertheless, both electrolyzers are facing corrosive environments (alkaline and acidic respectively) and are sensitive to water impurities.

2.3.3 Performance

It is also important to compare the performance of both technologies. The range of efficiencies (LHV) vary, but it usually comprises between 50-78% for AWE and 50-83% for PEM. Nonetheless, this efficiency comparison found in the literature [37], [38] is not a definitive or case-closed comparison, since it comprises a large spectrum of sources. It is also important to turn to commercial manufacturers for specification request like Nel Hydrogen who reports efficiencies at stack around 3.8-4.4 kWh Nm^{-3} (AWE) and 4.5 kWh Nm^{-3} (PEM) [44], equivalent to 67-77% (LHV).

On the other hand, AWE and PEM work in different ranges of current density as it was shown in Table 2.1 and these are well settled. If the curves of AWE and PEM are plotted operating in the same range, it is obtained the results that Schalenbach *et al.* [42] performed in 2016 as displayed in Figure 2.6.

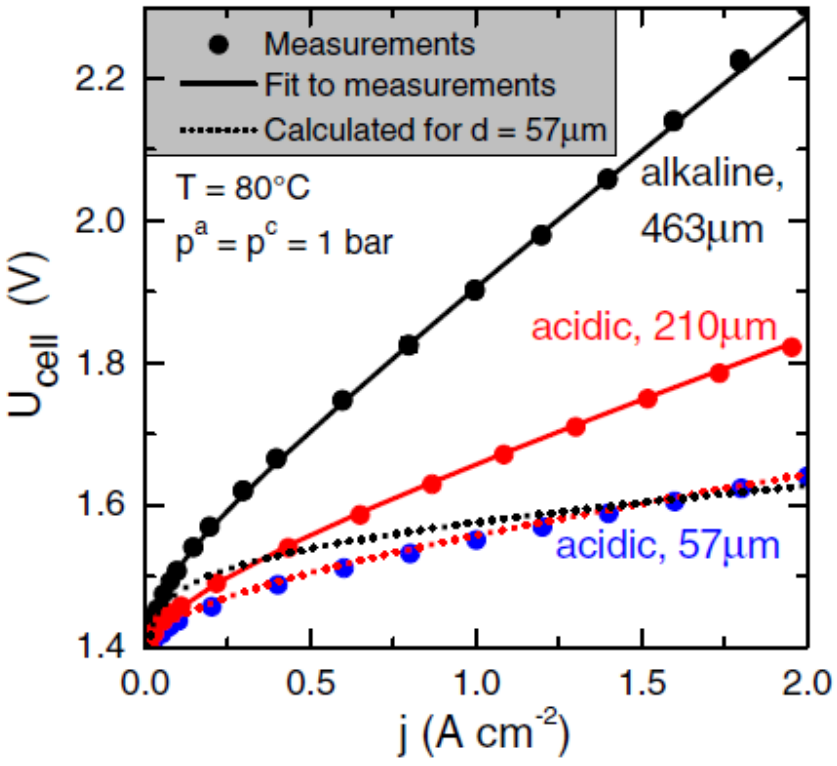

Figure 2.6: Overvoltage for AWE and PEM in the same current density range [42].

The red and blue dotted lines correspond to acidic cells with Nafion membranes of different thicknesses (210 µm and 57 µm) and the dotted black line for an alkaline cell with a diaphragm thickness of 463 µm. The objective of this study was to compare the voltage curves for two equivalent cells with the same thickness (57 µm) for both, membrane and diaphragm, according to their model [42].

AWE electrolyzers working principle consists on using hydroxil ions OH^- as charge carrier with a KOH solution permeating through the porous structure of the diaphragm. This method carries the risk of gas intermixing (H_2 and O_2) between both chambers known as crossover. To reduce this risk thicker diaphragms and spacers are used, however, this increases the total ohmic resistance of the cell harming the efficiency [38]. Since it is not viable to reduce the diaphragm thickness to comparable dimensions to Nafion membranes, then the alternative is to work at lower current densities with the same voltage range and efficiency than PEM. In order to increase the power to comparable levels then the electrode area is increased. This logic leads to a relatively bulky design for alkaline stacks and quite compact for PEM, but since the cost of components and materials for AWE is fairly more economical than PEM, this is an adequate approach.

This relatively high crossover in AWE through the diaphragm limits its operating pressure, as well as the main reason why AWE may not perform differential pressure between cathode and anode. This problem also relates to the lower H_2 purity in AWE (99.5-99.99%) compared to PEM's (99.9-99.99%) [37].

Lastly, it is important to compare the dynamic performance of both technologies.

Table 2.2: Performance comparison [38], [37].

Parameter description	AWE	PEM
Load range of nominal load	15-100%	5-120%
Start up time	1-10 min	1 s-5 min
Shutdown time	1-10 min	Seconds
Ramp-up speed	0.2-20%/s	100%/s
Ramp-down speed	0.2-20%/s	100%/s

This table shows a superior performance of PEM respect to AWE, in terms of dynamic response to changes in H_2 demand. If the nature of renewable sources is analyzed, it is characterized for intermittent production and operating at minimum and maximum capacity during short periods of time. PEM electrolyzers seem to be better suited to meet these requirements given their energy efficient stand-by operation, their short cold-start times and wide loading range (5-120%) [46].

The Puertollano green hydrogen plant is a good proof of concept for this logic. This Iberdrola project commissioned in 2022 enabled the connection of 100 MW photovoltaic solar plant with a 20 MWh, 5 MW lithium-ion battery system and 20 MW capacity PEM electrolytic hydrogen production system [48].

2.4 Summary

In conclusion, since the aim of this thesis is to propose and model a hypothetical GigaWatt electrolytic station connected to the High Voltage AC transmission grid, the economies of scale for a plant of this size require the solution with lowest investment cost, more scalability and longer lifetime.

Applying the maximum CAPEX costs stated in Table 2.3 and considering 1 GW of electrolyzer capacity, implementing AWE can lead to a reduction of 380 million USD of investment cost over PEM. Another argument is the non-intermittent condition of supply which does not require any high performance response.

These factors push the balance for selection of AWE as the candidate for model development in the substation. Nonetheless, as it is seen in subsequent sections, this model is not limited by its technology and it is exchangeable for PEM electrolyzers.

All the information stated in this chapter is summarized in the table below, highlighting the key differences between both technologies.

Table 2.3: Performance comparison [38], [37].

Parameter description	AWE	PEM
Temperature	70-90°C	50-80°C
Pressure	<30 bar	<70 bar
Nominal current density	0.2-0.8 A/cm^2	1-2 A/cm^2
Efficiency (LHV)	50-78%	50-83%
Gas purity	>99.5%	99.99%
CAPEX	500-1000 USD/kW	700-1400 USD/kW
Operating stack lifetime	60 000 - 90 000 h	50 000-80 000 h
Load range of nominal load	15-100%	5-120%
Start up time	1-10 min	1 s-5 min
Shutdown time	1-10 min	Seconds
Ramp-up speed	0.2-20%/s	100%/s
Ramp-down speed	0.2-20%/s	100%/s

Although the alkaline electrolyzer technology is an old concept as it was first introduced by Troostwijk and Diemann in the year 1789 [40], there is still research and great breakthroughs coming out for this technology.

The latest achievement is the alkaline capillary-fed electrolysis technology [49], originally conceived in 2021 at University of Wollongong, Australia [50]. Professor Gerry Swiegers and Gordon Wallace, lead researchers of the team, later founded Hysata, a spin-out company of the university, to commercialize this new technology.

Its unique concept of water electrolysis comes from the introduction of capillary-induced transport along a porous inter-electrode separator, creating a bubble-free operation at the electrodes. This leads to a breakthrough in terms of efficiency, with a cell voltage of 1.51 V at 0.5 A cm^{-2}, 85ºC and a stack energy consumption of 40.4 kWh/kg compared to 47.5 kWh/kg in commercial electrolysis cells [49].

3

Thermodynamic and Electrochemical Analyses

An electrolyzer is an electrochemical device and its performance depends on many factors beyond the electrical, such as thermodynamics, chemical kinetics and equilibrium, acid-base theory and fluid mechanics. Even so, this section will focus only on analyzing the electrical and thermodynamic principles behind its behavior. Most of the theory developed in this chapter is based on the book Comprehensive Energy Systems, Chapter 4.25 Electrolyzers by Ibrahim Dincer and Abdullah A. AlZahrani [51]. This analysis is valid for both AWE and PEM electrolyzers equally.

3.1 Thermodynamics applied to chemical reactions

To analyze the thermodynamic behavior of the electrolyzer, boundaries are defined by placing a control volume (CV) over it to track the amount of substance entering and exiting, as depicted in Figure 3.1. There is one inlet for water and two separate outlets for the gas products.

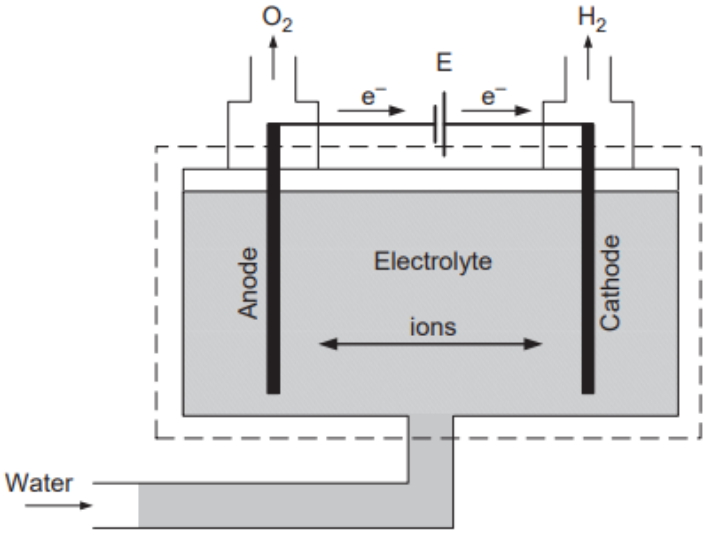

Figure 3.1: Control volume of the electrolyzer [51].

Assuming the conservation of mass and a steady-flow process, it is possible to apply the First and Second Law of Thermodynamics expressed respectively as

$$\dot{Q}_{in} + \dot{W}_{in} + \sum_{in} \dot{m} * h = \dot{Q}_{out} + \dot{W}_{out} + \sum_{out} \dot{m} * h \tag{3.1}$$

$$\dot{S}_{gen} = \sum_{out} \dot{m} * s - \sum_{in} \dot{m} * s - \frac{\dot{Q}_{in} - \dot{Q}_{out}}{T} \tag{3.2}$$

where Q is the heat flow, W the work, S_{gen} the entropy generation inside CV, T the CV temperature, $\dot{m}$ the mass flow, h the specific enthalpy and s the specific entropy. Subscript *in* and *out* represent the flow of either heat, work or substances going inwards and outwards the CV respectively. These expressions may be further simplified defining the net flow with subscript CV resulting in

$$\dot{Q}_{CV} + \dot{W}_{CV} = \sum_{out} \dot{m} * h - \sum_{in} \dot{m} * h \tag{3.3}$$

$$\dot{S}_{gen} = \sum_{out} \dot{m} * s - \sum_{in} \dot{m} * s - \frac{\dot{Q}_{CV}}{T} \tag{3.4}$$

In order to have a better understanding of what it means to have net positive and negative flow of heat and work in the CV, the sign criteria is mentioned in Table 3.1.

Table 3.1: Sign criteria for heat transfer and work.

$\dot{Q}_{CV} = \dot{Q}_{in} - \dot{Q}_{out}$	$\dot{Q}_{CV} > 0$: Endothermic process	$\dot{Q}_{CV} < 0$: Exothermic process
$\dot{W}_{CV} = \dot{W}_{in} - \dot{W}_{out}$	$\dot{W}_{CV} > 0$: Consumes work	$\dot{W}_{CV} < 0$: Produces work

Expressions (3.3) and (3.4) need to be adapted for chemical reactions environments. In addition to sensible and latent energy, which are associated with temperature and phase changes, the substances' molecules also possess chemical energy that varies by modifying their molecular composition. For the electrolysis reaction, First and Second Laws of Thermodynamics can be reformulated by substituting the mass flows $\dot{m}$ for molar flows $\dot{n}$ and expressing the specific enthalpy terms based on their enthalpy of formation h_f^o.

$$\dot{Q}_{CV} + \dot{W}_{CV} = \dot{n}_{H_2}(h_f^o + h - h^o)_{H_2} + \dot{n}_{O_2}(h_f^o + h - h^o)_{O_2} - \dot{n}_{H_2O}(h_f^o + h - h^o)_{H_2O} \tag{3.5}$$

$$\dot{S}_{gen} = (\dot{n}s_{H_2}) + (\dot{n}s_{O_2}) - (\dot{n}s_{H_2O}) - \frac{\dot{Q}_{CV}}{T} \tag{3.6}$$

Standard enthalpy of formation h_f^o may be understood as the enthalpy of a substance at a specified state due to its chemical composition. All elements in their natural states like hydrogen gas, oxygen gas and solid carbon in the form of graphite, have a h_f^o of zero at

standard conditions of pressure and temperature (25°C and 1 atm). Furthermore, expression (3.5) can be expressed per mol of hydrogen produced, which gives the stoichiometric coefficients and all properties expressed on specific terms (per mol terms).

$$q_{CV} + w_{CV} = (h_f^o + h - h^o)_{H_2} + \frac{1}{2}(h_f^o + h - h^o)_{O_2} - (h_f^o + h - h^o)_{H_2O} = \Delta h \tag{3.7}$$

$$q_{CV} = T(s_{H_2} + \frac{1}{2}s_{O_2} - s_{H_2O}) - Ts_{gen} = T(\Delta s - s_{gen}) \tag{3.8}$$

All variables defined in the previous and in the following equations are listed in Table 3.2:

Table 3.2: Thermodynamic variables.

Parameter description	Parameter	Unit
Net specific enthalpy	Δh	kJ mol^{-1}
Net specific Gibbs energy	Δg	kJ mol^{-1}
Net specific entropy	Δs	J (mol K)$^{-1}$
Standard enthalpy of formation	h_f^o	kJ mol^{-1}
Specific enthalpy (T, P)	h	kJ mol^{-1}
Standard specific enthalpy	h^o	kJ mol^{-1}
Specific entropy (T, P)	s	J (mol K)$^{-1}$
Specific generated entropy	s_{gen}	J (mol K)$^{-1}$
Specific heat transfer	q_{CV}	kJ mol^{-1}
Specific work	w_{CV}	kJ mol^{-1}

Applying the different species properties of Table 3.3, it is possible to calculate the net enthalpy Δh and entropy Δs of electrolysis at standard conditions using equation (3.7), (3.8):

$$\Delta h^o = h_{f,H_2}^o + \frac{1}{2}h_{f,O_2}^o - h_{f,H_2O}^o \tag{3.9}$$

$$\Delta s^o = s_{H_2} + \frac{1}{2}s_{O_2} - s_{H_2O} \tag{3.10}$$

which results in a Δh^o of 285.826 kJ mol^{-1} and $\Delta s^o = 0.163$ kJ (mol K)$^{-1}$. Since electrolysis Δh^o is positive, the reaction is an endothermic reaction in standard conditions, which means that it needs a heat flow or work of 285.826 kJ into the system per mol of hydrogen produced in order to keep the system's temperature constant.

Table 3.3: Thermodynamic properties for liquid water, hydrogen and oxygen under standard conditions [51].

Substance	Enthalpy of formation h_f [kJ mol^{-1}]	Gibbs free energy g_f [kJ mol^{-1}]	Entropy s [J (mol K)$^{-1}$]
Water(l)	- 285.826	- 237.180	69.92
Hydrogen	0	0	130.68
Oxygen	0	0	205.14

Two different scenarios are compared: one where the process occurs in an adiabatic system (no heat flow is allowed) and another where the process is reversible (no generated entropy or irreversibilities). In both scenarios, equations (3.7) and (3.6) are applied.

Table 3.4: Impact of an adiabatic system and reversible process on electrolysis.

Adiabatic system $q_{CV} = 0$	Reversible process $s_{gen} = 0$
$w_{CV} = \Delta h = 285.826$ kJ mol^{-1}	$q_{CV} = T\Delta s = 48.697$ kJ mol^{-1}
$s_{gen} = \Delta s = 0.163$ kJ (mol K)$^{-1}$	$\dot{w}_{CV} = \Delta g = 237.13$ kJ mol^{-1}

From these results, it is possible to get three conclusions:

- The necessary work w_{CV} for electrolysis is greater in an adiabatic process than in a reversible process.
- In a reversible process, work w_{CV} equals to the free Gibbs energy of reaction Δg.
- Electrolysis free Gibbs energy Δg is positive, which means that at standard conditions, it is a non-spontaneous reaction.

3.2 Reversible and Thermoneutral Potentials

After evaluating the thermodynamics of the electrolyzer, the next step is analyzing its electrical correlation. By merging equation (3.7), (3.8) and adding the definition of Gibbs free energy Δg, it is possible to obtain the relationship between this last variable and the work applied to the electrolytic cell w_{CV}.

$$w_{CV} = \Delta h - T\Delta s + Ts_{gen} = \Delta g + Ts_{gen} \tag{3.11}$$

In principle, electrochemical cells convert chemical energy to electrical energy and vice versa, so it is possible to correlate the necessary work of the reaction w_{CV} with the potential given by the cell E_{cell}. This results in equation (3.12), where w_{CV} is equal to the product of E_{cell} and the total charge transferred during the reaction zF, being z the number of electron moles pero mol of hydrogen produced and F the Faraday constant.

$$w_{CV} = zFE_{cell} \tag{3.12}$$

By amalgamating equation (3.11) and (3.12), it is possible to define an equation that establishes a relationship between the net Gibbs free energy Δg, and the reversible voltage E_r. The overvoltage term E_{loss} accounts for the reaction's irreversibilities and E_r represents the minimum voltage required to start the electrolysis reaction.

$$E_{cell} = \frac{\Delta g}{zF} + \frac{Ts_{gen}}{zF} = E_r + E_{loss} \tag{3.13}$$

Yet, this operating point does not provide any information about the thermal behavior of the electrolyzer. Either if electrolysis is an endothermic or exothermic process depends

on the thermoneutral voltage E_{th}. Furthermore, it is possible to modify the cell potential definition with E_{th} as the main input as shown in equation (3.14).

$$E_{cell} = \frac{\Delta h}{zF} - \frac{T\Delta s}{zF} + \frac{Ts_{gen}}{zF} = E_{th} - \frac{T\Delta s}{zF} + E_{loss} \tag{3.14}$$

When the electrolytic cell is operated above E_{th}, the reaction becomes exothermic, and heat must be removed from the cell for maintaining constant temperature operation which is known as "isothermal operation". On the other hand, operating under E_{th} demands absorption of heat to keep isothermal operation [52]. Applying standard conditions of pressure and temperature, the following potentials are calculated using the values provided in Table 3.4, with E_r^o equal to 1.23 V and E_{th}^o to 1.48 V. This principle is displayed in Figure 3.2.

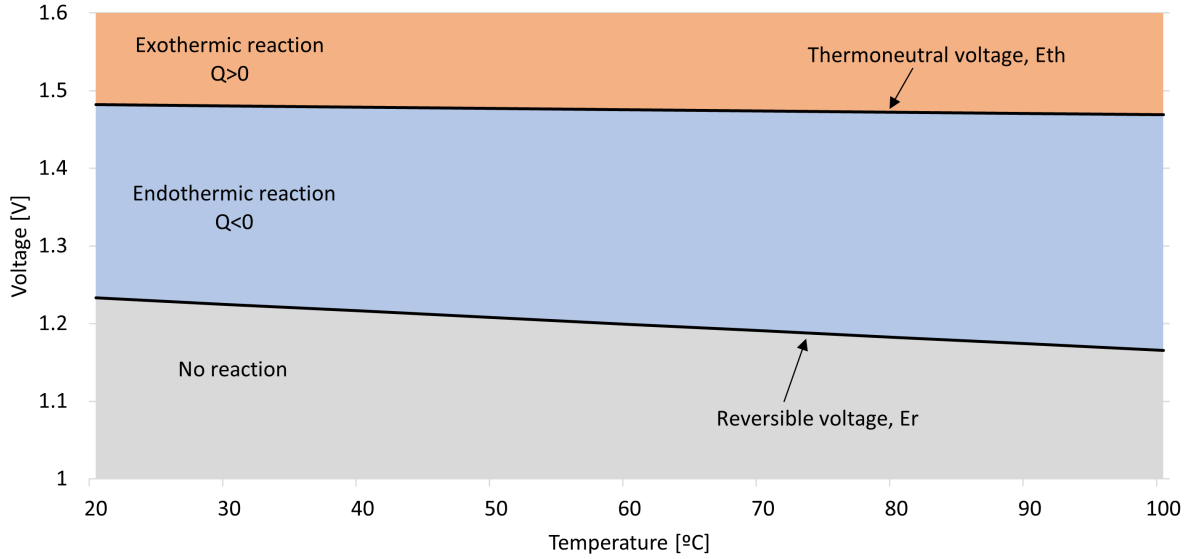

Figure 3.2: Reversible and thermoneutral potential versus temperature at atmospheric pressure.

Although it is important to consider the thermoneutral voltage E_{th} when defining the thermal model, working under endothermic operation is not a concern since the heat demand is mitigated by the irreversibilities of the reaction E_{loss}. To operate above the thermoneutral voltage, manufacturers usually apply a minimum loading limit which for AWE is around 15% [44]. This ensures that the electrolyzer always functions as an exothermic and refrigerated device.

Both potentials E_r and E_{th} are not constant. They depend on the electrolyzer operating pressure and temperature. Therefore, it is necessary to study this effect, for which task the equations stated below will be used. Those are derived in the reference book [51].

$$\frac{\partial E_r}{\partial T} = \frac{1}{zF} * \frac{\partial \Delta g}{\partial T} = -\frac{\Delta s}{zF} \tag{3.15}$$

$$\frac{\partial E_r}{\partial P} = \frac{1}{zF} * \frac{\partial \Delta g}{\partial P} = \frac{\Delta v}{zF} = \frac{\Delta NRT}{zF}\frac{1}{P} \tag{3.16}$$

Some conclusions may be obtained from both equations. First, equation (3.15) results into a constant, which is -0.0008464 V/K at standard conditions using the data from Table 3.3, and gives E_r a linear dependence respect to temperature. On the other side, it shows a logarithmic behavior with pressure according to equation (3.16). If both expressions are integrated between the standard point of operation and the objective temperature and pressure, equation (3.15) and (3.16) are derived:

$$E_r(T, P_o) = \int_T^{T_o} \frac{\partial E_r}{\partial T}\, dT = E_r^o - \frac{\Delta s}{zF} * (T - T_o) \tag{3.17}$$

$$E_r(T, P) = \int_P^{P_o} \frac{\partial E_r}{\partial P}\, dP = E_r(T, P_o) + \frac{\Delta N R T}{zF} \ln \frac{P}{P_o} \tag{3.18}$$

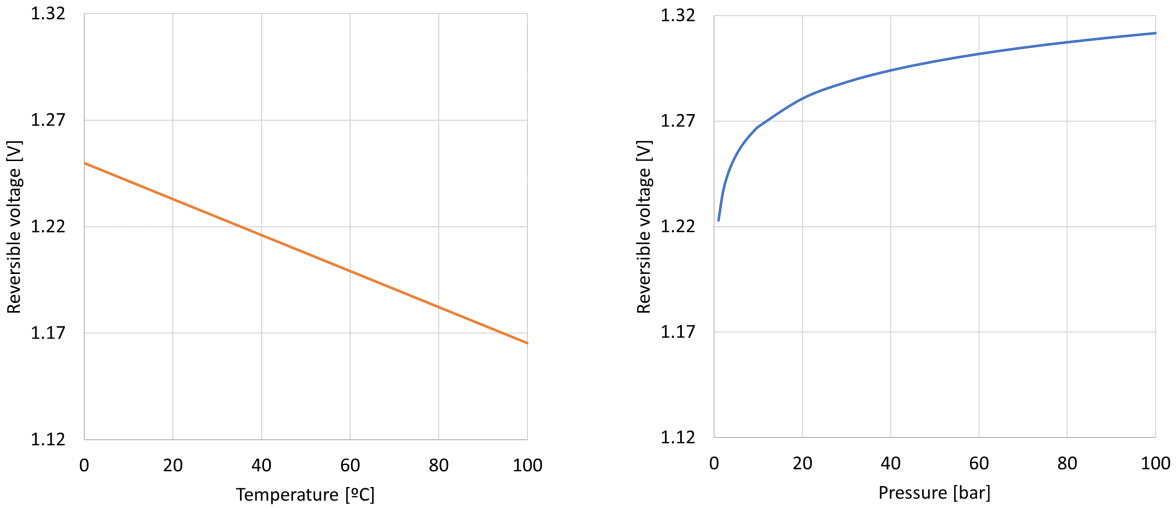

(a) At atmospheric pressure (1 bar).

(b) At ambient temperature (25°C).

Figure 3.3: Effects of operating pressure and temperature on the reversible voltage.

A conclusion gained from Figure 3.3b is why in PEM electrolyzers the minimum loading limit is closer to 5% unlike 15% in AWE. Since PEM electrolyzers usually work at pressures around 30 bar or more, it increases its reversible voltage, which gets E_r closer to E_{th} than its counterpart AWE working at atmospheric pressure.

Besides the operating temperature and pressure, there is one last factor that may modify the reversible cell potential: the reactant concentration. This effect is calculated through the Nernst equation, which allows to calculate E_r in case of a differential pressure between the electrolyzer's cathode and anode as may happen in PEM electrolyzers.

$$E_r = E_r^o + \frac{RT}{zF} \ln \frac{p_{H_2} p_{0_2}^{\frac{1}{2}}}{p_{H_2O}} \tag{3.19}$$

The results obtained from these equations agree with the ones published by Hammoudi *et al.* [53] and Adibi *et al.* [54]. In both studies the reversible voltage increases accordingly with the pressure and decreases with temperature as shown in Figure 3.4.

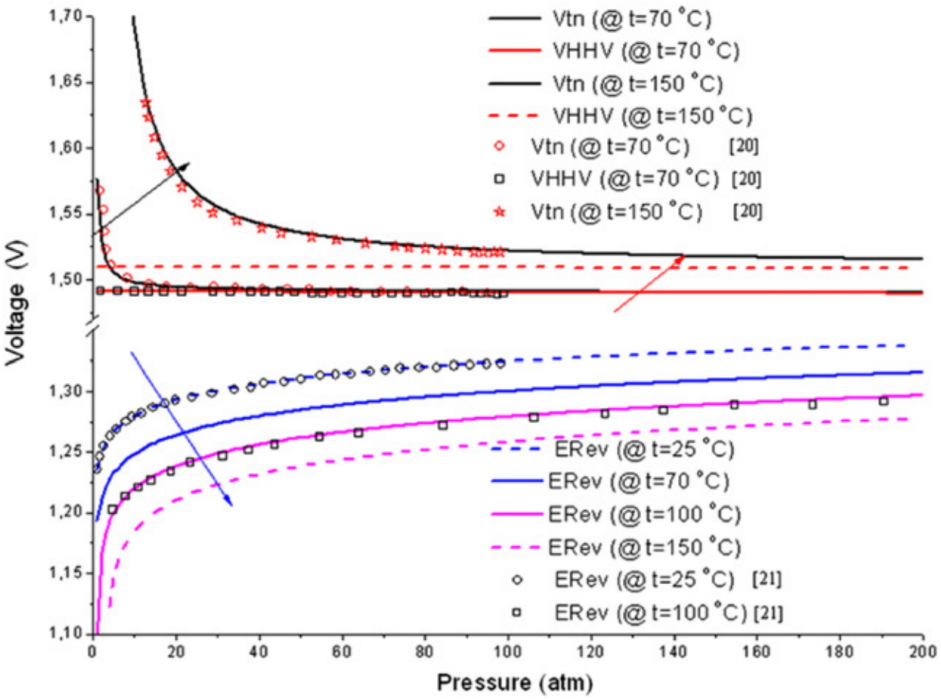

Figure 3.4: Pressure and temperature effect on reversible and thermoneutral potentials [53].

A simple analysis of thermoneutral potential E_{th} dependence with temperature at atmospheric pressure can be done by reformulating the enthalpies in equation (3.7) into equation (3.20). The results are obtained by applying the enthalpy of formation of electrolysis, the enthalpy of components at standard conditions and at operating conditions (NIST thermophysical experimental data [55]).

$$\Delta h = \Delta h_f + (h - h^o)_{H_2} + \frac{1}{2}(h - h^o)_{O_2} - (h - h^o)_{H_2O} \tag{3.20}$$

Table 3.5: Enthalpy for water, hydrogen and oxygen at atmospheric pressure versus temperature.

Temperature [K]	290	300	310	320	330	340	350	360
$h_{H_2}(g)$ [J mol^{-1}]	7691.2	7979.4	8268.3	8557.7	8847.7	9138.1	9428.8	9719.8
$h_{O_2}(g)$ [J mol^{-1}]	8432.4	8726.5	9021.1	9316.2	9611.9	9908.2	10205	10503
$h_{H_2O}(l)$ [J mol^{-1}]	1275.9	2029.5	2782.5	3535.5	4288.8	5042.9	5798	6554.3
Δh [kJ mol^{-1}]	286.09	285.77	285.45	285.13	284.82	284.5	284.19	283.87
E_{th} [V]	1.483	1.481	1.479	1.478	1.476	1.474	1.473	1.471

These values obtained from tabulated experimental data can be compared with the results acquired from the empirical equation deduced by Hammoudi *et al.* in [53]. When both methods are compared, the difference in each temperature step is lower than 1 mV.

To study the thermoneutral potential dependence with pressure requires a more advanced model as presented in articles [53] and [54]. Nevertheless, the results of that analysis can be observed in Figure 3.4.

3.3 Polarizations and efficiency

The main purpose of this chapter is to develop the overvoltage term E_{loss} introduced in equation (3.13). This accounts for the reaction's irreversibilities and the efficiency decrease of the cell. It can be classified into three main types of polarizations:

3.3.1 Activation losses

The activation polarization is attributed to the charge transfer that happens at the electrode surface. An analogy for this overvoltage is a resistance in the electrochemical reaction occurring at the electrode–electrolyte interface in both the anode and cathode. The real reason of this overvoltage is due to the fact that there are elementary reactions happening at the molecular level, in contrast to the simplistic cathodic and anodic reactions shown in the schematics of section 2. Its value is determined by the Butler-Volmer equation (3.21) and can be separated into cathode and anode overpotentials known as Tafel equations.

$$J_{cell} = J_o[\exp\left(\frac{zF}{RT}\alpha_{an}\eta_{act,an}\right) - \exp\left(-\frac{zF}{RT}\alpha_{ca}\eta_{act,ca}\right)] \tag{3.21}$$

$$\eta_{act,an} = \frac{RT}{\alpha_{an}zF}\ln\left(\frac{J_{cell}}{J_{o,an}}\right) \qquad \eta_{act,ca} = \frac{RT}{\alpha_{ca}zF}\ln\left(\frac{J_{cell}}{J_{o,ca}}\right)$$

3.3.2 Ohmic losses

The ohmic polarization is more intuitive than the rest since it presents a linear behavior respect to the current density and fulfills Ohm's Law. The ions moving through the electrolyte and membrane/diaphragm find ionic resistance in its path as well as the electrons through the electrodes. The sum of all these components, since they are all in series, gives the total electric resistance.

$$\eta_{ohm} = I_{cell}R_{tot} = I_{cell}\sum_i \frac{\delta_i}{\sigma_i A} = J_{cell}\sum_i \frac{\delta_i}{\sigma_i} \tag{3.22}$$

In the case of AWE, the ohmic resistance R_{tot} mainly depends on the electrolyte conductivity σ which depends on the molarity and temperature [41]. In PEM electrolyzers it is similar but on the thickness δ and conductivity of the membrane σ instead [56].

3.3.3 Concentration losses

The concentration polarization is an overvoltage attributed to the lack of reactants at the electrode-electrolyte interface. In electrolysis, the overvoltage is typically negligible due to the abundance of reactants in the electrolyzer: the electrodes are fully immersed in water, ensuring a wide supply of reactants. Nevertheless, this effect becomes noticeable at high loadings due to the accumulation of gas bubbles in the membrane, resulting in an exponential voltage increase.

The sum of the reversible cell potential and the overvoltages stated above gives the cell potential. Dividing the reversible potential by the cell potential gives the voltage efficiency η_V, also known as low heating value (LHV) efficiency η_{LHV} of the electrolyzer.

$$\eta_V = \frac{E_r}{E_{cell}} = \frac{E_r}{E_r + E_{loss}} \tag{3.23}$$

Another type of efficiency measured against the thermoneutral voltage E_{th} instead of E_r is known as high heating value (HHV) efficiency η_{HHV}, which considers the necessary heat at voltages lower than E_{th} to maintain isothermal operation. This method is not as popular as LHV since it gives efficiencies greater than 100% at voltages lower than E_{th}.

An analysis of temperature and pressure on the reversible and thermoneutral voltage has already been made, but these can impact the polarization terms as well. As shown in Figure 3.5a, the cell voltage decreases with temperature since all potentials decrease with it accordingly. In the case of pressure, it increases mainly due to the reversible voltage and it is displayed in Figure 3.5b.

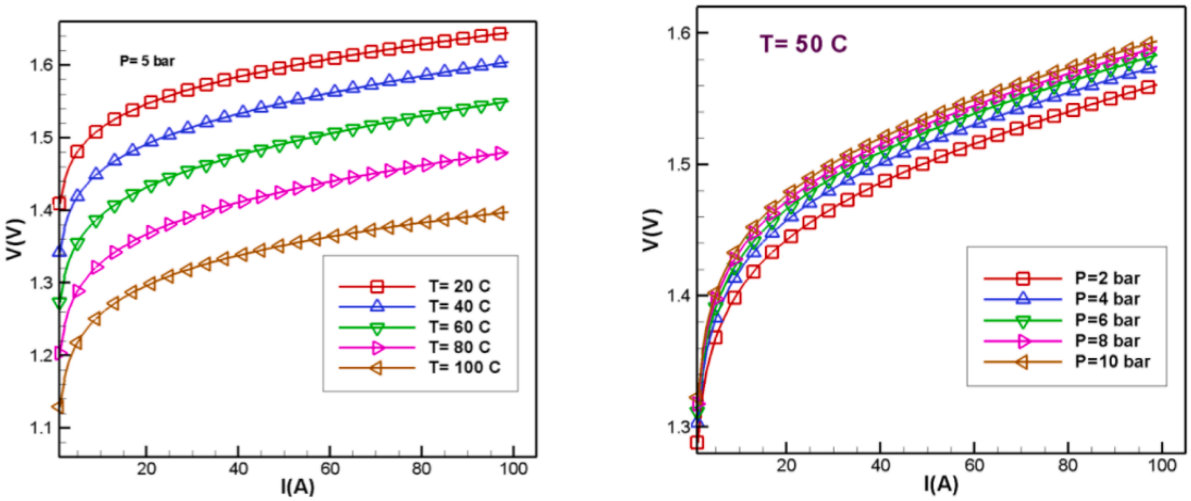

(a) Temperature effect on cell voltage.

(b) Pressure effect on cell voltage.

Figure 3.5: Cell voltage dependence on temperature and pressure [54].

3.4 Faraday's Law of Electrolysis

Besides his great contributions to electromagnetism with his fundamental law of induction formulated in 1831, Michael Faraday also made important discoveries in electrochemistry. The famous English scientist formulated two laws for electrolysis that combined (3.24) allows to calculate the ideal production of hydrogen $\dot{m}_{ideal,H_2}$ with only the cell current I_{cell} as input, being M_{H_2} the molecular weight of hydrogen and n_{series} the number of cells in series.

$$\dot{m}_{ideal,H_2} = \frac{M_{H_2} n_{series}}{zF} I_{cell} \tag{3.24}$$

Although most of the times this expression can be directly implemented to calculate the hydrogen production, this law needs a correction factor that accounts for physical phenomena that reduces hydrogen production. This factor is popularly named Faraday or current efficiency η_F, which has a value of 92-98% in most of the operating range.

This factor is measured empirically using a mass flow meter, either Coriolis [57] or thermal bypass, and it is divided by the theoretical mass flow $\dot{m}_{ideal,H_2}$ given by equation (3.24). Both kinds of flow meter technologies are found and explained in the Bronkhorst catalog [58]. Other measuring set-ups can be implemented using volume flow meters, like differential pressure or vortex, in combination with thermal and pressure sensors.

$$\eta_F = \frac{\dot{m}_{H_2}}{\dot{m}_{ideal,H_2}} * 100 \tag{3.25}$$

The physical phenomena causing this reduction in hydrogen production are parasitic currents, gas crossover and gas leakage. Gas leakage is generally negligible and gas crossover is very important in PEM electrolyzers, where differential pressure between the anode and cathode may be used. According to Hug *et al.* [59], the crossover flow can be determined doing a simple test where the anode side is operated under normal conditions, but the technician closes the cathode side using a valve as displayed in Figure 3.6.

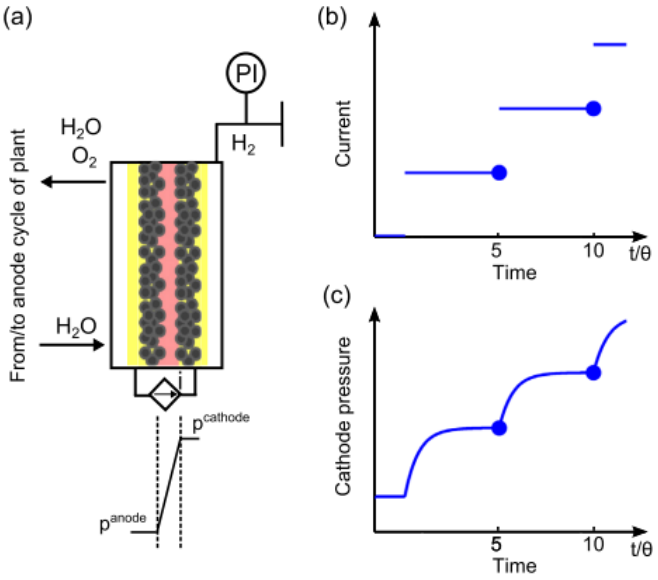

Figure 3.6: Test schematics, applied currents and cathode's pressure [59].

Although measuring the hydrogen crossover presents the risk of contamination and creation of an explosive environment in the the oxygen stream, it is not the main cause of hydrogen leak in regular operation. The problem comes from the parasitic or shunt currents, which go through the side channels causing an unintended discharge and consequent reduction of the effective current going through the cell and producing hydrogen. An analogy has been done with an AWE with bipolar arrangement as presented in Figure 3.7a, which is more common than the monopolar configuration. The resistances shown in the inlet channels (bottom side of Figure 3.7a,3.7b) and the outlet channels (top side) represent the ionic resistance of the KOH solution, not the channels themselves, which are made of electrically insulating materials.

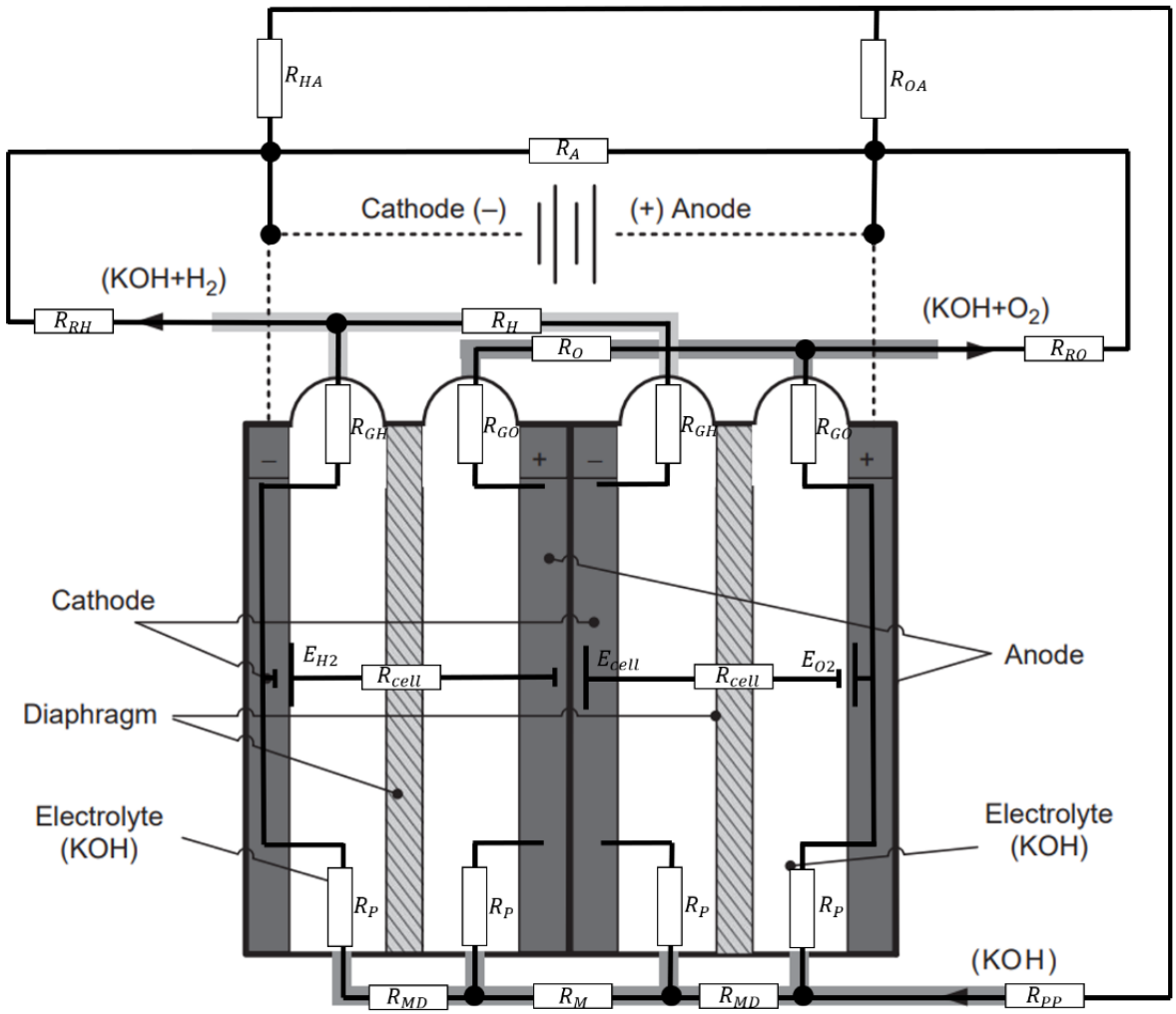

(a) Equivalent Circuit [51].

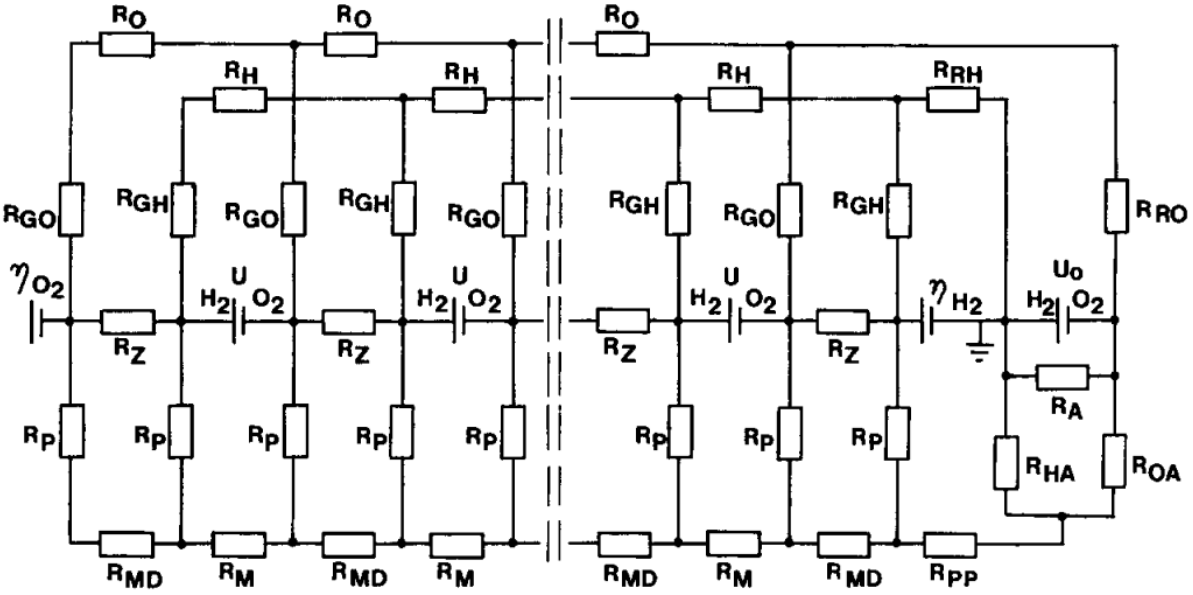

(b) Electrical Analogue [60].

Figure 3.7: Lumped Parameter Circuit.

The electrical analogue of Figure 3.7b comes from an article published by Divisek *et al.* [60], who created a lumped parameter model of an alkaline bipolar 30-cell stack based on its geometrical dimensions as shown in Figure 3.7a. Solving this model with Kirchhoff's laws, it is obtained the electrolyzer's shunt current distribution shown in Figure 3.8.

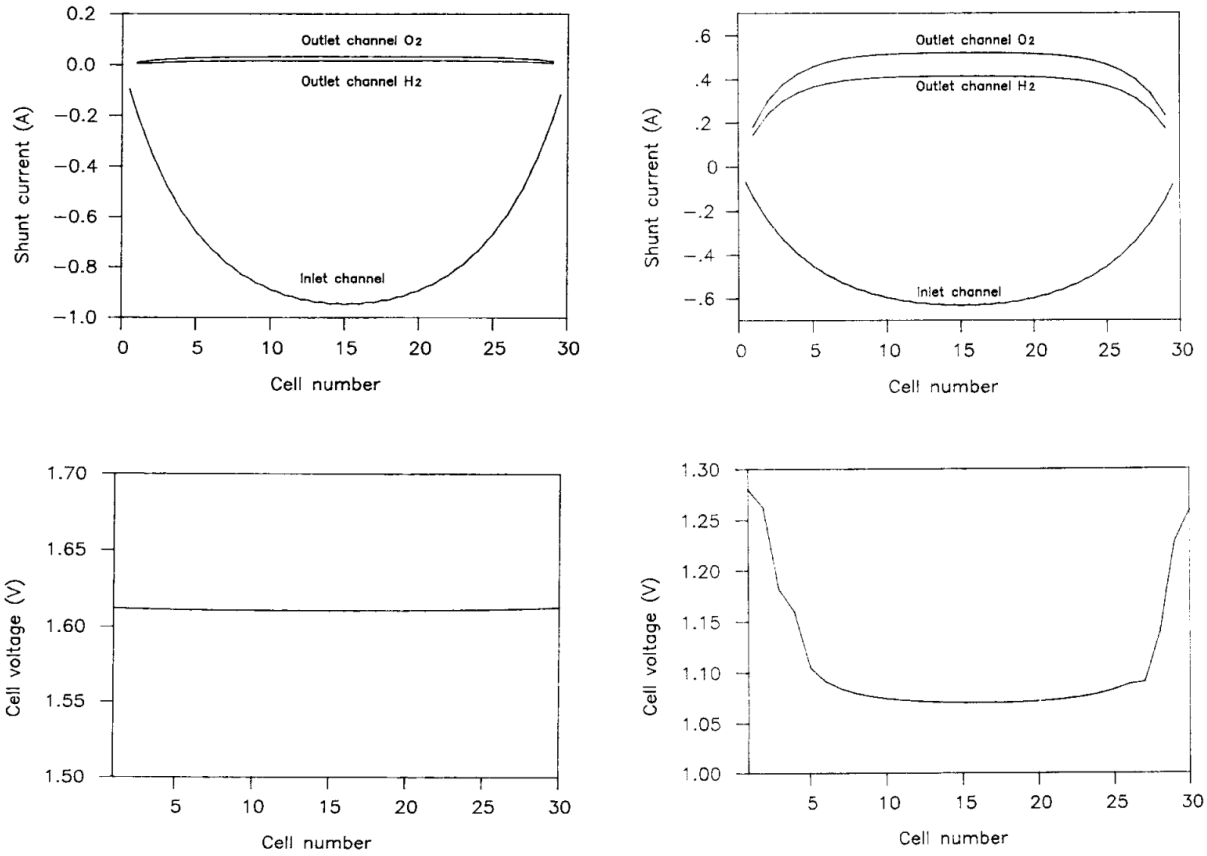

(a) Current density of 4000 A m^{-2}.

(b) Current density of 50 A m^{-2}.

Figure 3.8: Parasitic current distribution and individual cell voltage in a thirty-cell stack [60].

From these profiles it can be observed that the shunt currents in the outlet or gas channels present a susceptible behavior to current density variations, unlike in the electrolyte feed channels. A second observation is that the parasitic currents in the gas channels only become important for very low current densities. A possible theory behind this behavior is the emergence of hydrogen and oxygen bubbles in the gas channels when there is high current density, which increases significantly the ohmic resistivity of this path.

In a similar article [61] to the paper published by Divisek, Mergel and Schmitzto [60], Hug *et al.* developed a lumped model of their electrolyzer, confirmed said model with measurements and created a chart for the current efficiency contrasting both model and empirical results. The results validate the conclusions reached in the previous paragraph since the efficiency drops heavily for low density values. An additional insight is the drop of efficiency at higher temperatures due to lower resistivity of the KOH solution.

4

Alkaline Water Electrolyzer Modeling in PowerFactory

Two articles were used as core references to develop the AWE model. The first paper [43], published by Øystein Ulleberg in 2003, divides the model implementation in three sections: I-U curves, thermal model and hydrogen production. Subsequently, an IEEE team of Aalborg University published an article [62] in 2013 using Ulleberg's outline to develop their own model in PowerFactory. This last article served as benchmark to design and validate the electrolyzer in DIgSILENT PowerFactory, for which they deserve acknowledgement.

Given the lack of technical specifications for a commercial MW-scale electrolyzer beyond their catalog performance characteristics like hydrogen production, operating temperature, pressure and footprint, the implemented procedure was to base the model on the electrolyzer installed in the PHOEBUS demonstration plant, situated in Jülich, Germany.

The PHOEBUS electrolyzer under consideration boasts a robust operational history spanning almost a decade, from 1994 to 2003, and its performance monitored by Ghosh *et al.* [63]. Moreover, it has recurrently served as a benchmark in scientific literature, facilitating comparisons between theoretical models and empirical findings, as evidenced by references such as [43] and [53]. Lastly, its operation ratings and design specifications are shown in Table 4.1.

Table 4.1: PHOEBUS AWE operation ratings and design specifications [53].

Parameter	Value	Parameter	Value
Electrolyzer rated power	26 kW	Electrode area	0.25 m^2
Number of cells in stack	21	Electrolyte	KOH (30-40 wt.%)
Max. block voltage	35-37 V	Anode (O_2 side)	Ni/Co_3O_4/Fe on Ni-plate
Max. current density [43]	3500 A m^{-2}	Cathode (H_2 side)	CePt on performed Ni-plate
Max. temperature	80°C	Diaphragm	Ni-mesh supported NiO
Max. operation pressure	7 bar	Design	Zero spacing

4.1 Model definition

As mentioned before, Øystein Ulleberg [43] divided his model implementation in three sections: I-U curves, thermal model and hydrogen production. The thermal model is out of the thesis scope but it would have been beneficial for the general project scope, since

it enables to simulate thermal transients like cold-start procedure, as well as considering additional electrical consumption such as a water pump, which extracts heat but reduces the system's efficiency. Nonetheless, an experimental method would be required to update the thermal model parameters like the electrolyzer's thermal resistance and capacitance when scaling-up the size and electrical consumption of the device from kWs to MWs.

Table 4.1 presents the operating limits and design parameters of the electrolyzer. However, this data does not provide information regarding cell polarizations or Faraday efficiency, both necessary to analyze the AWE performance at a specific point of operation. The calculation of both properties is possible using equations (4.1), (4.2) and the parameters listed in Table 4.2 introduced by Øystein Ulleberg and the Aalborg University team.

$$E_{cell} = E_r(T,P) + (r_1 + r_2 T) J_{cell} + s \log((t_1 + \frac{t_2}{T} + \frac{t_3}{T^2}) J_{cell} + 1) \tag{4.1}$$

$$\eta_F = a_1 \exp\left(\frac{a_2 + a_3 T}{J_{cell}} + \frac{a_4 + a_5 T}{{J_{cell}}^2}\right) \tag{4.2}$$

Table 4.2: PHOEBUS AWE I-U curves and Faraday Efficiency parameters [43],[62].

Parameter	Parameter description	Value	Unit
r_1	Ohmic parameter 1	8.05 x 10^{-5}	Ω m^2
r_2	Ohmic parameter 2	-2.5 x 10^{-7}	Ω $m^2/^oC$
s	Coefficient of electrode overvoltage	0.185	V
t_1	Overvoltage coefficient 1	-0.1	m^2/A
t_2	Overvoltage coefficient 2	8.424	m^2 $^oC/A$
t_3	Overvoltage coefficient 3	247.3	m^2 $^oC^2/A$
a_1	Faraday efficiency coefficient 1	99.5	%
a_2	Faraday efficiency coefficient 2	-9.578	A/m^2
a_3	Faraday efficiency coefficient 3	-0.055	A $(m^2$ $^oC)^{-1}$
a_4	Faraday efficiency coefficient 4	1502.708	A^2/m^4
a_5	Faraday efficiency coefficient 5	-70.8	$A^2(m^4$ $^oC)^{-1}$

The first step to calculate the cell potential E_{cell} in equation (4.1) is introducing the reversible voltage E_r at operation conditions, which is calculated as described in section 3.2. The second term of the equation reflects the ohmic polarization, which shows a linear behavior with temperature, while the third term accounts for the activation overvoltage which presents a logarithmic behavior. It is noticeable that the operating pressure affects the reversible potential, but not the polarization terms.

In both figures 4.1 and 4.2, it is performed a temperature sweep from 20 to 80°C and the voltage and current efficiencies are calculated. This temperature range depicts the nominal behavior of the electrolyzer from ambient till operating temperature at atmospheric pressure. There is no value in obtaining curves above this point since this is the highest operating temperature for industrial AWEs. Besides, working close to 100°C carries the risk of reaching the boiling point of water.

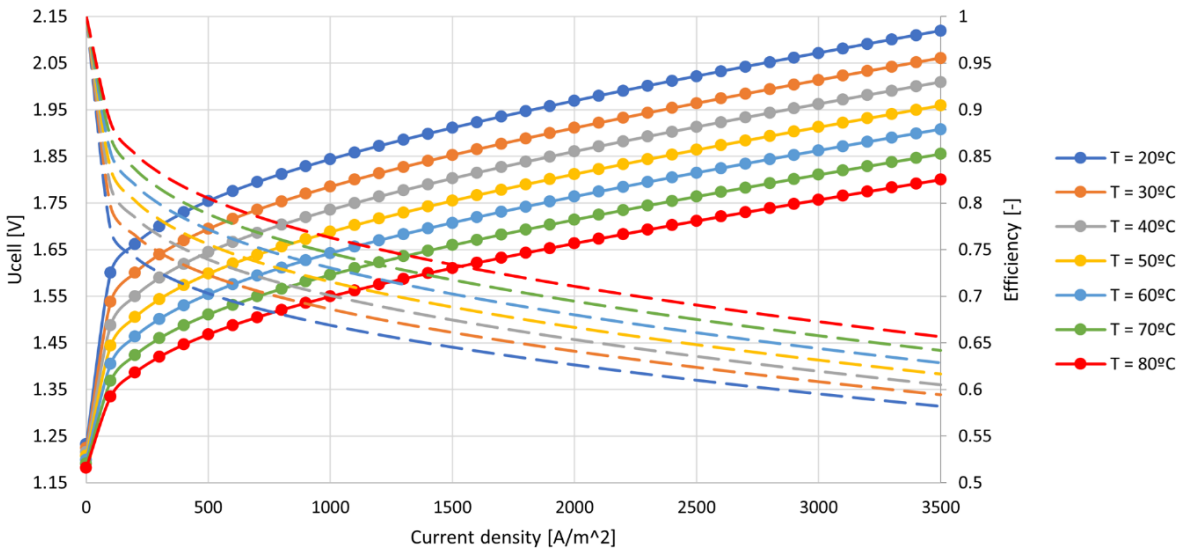

Figure 4.1: Characteristic IU curves and Voltage Efficiency.

In [62], it is proposed the empirical equation (4.2) to model Faraday efficiency, which is shown in Figure 4.2. This expression reflects the concepts explained in section 3.4, accounting for the parasitic currents and gass crossover.

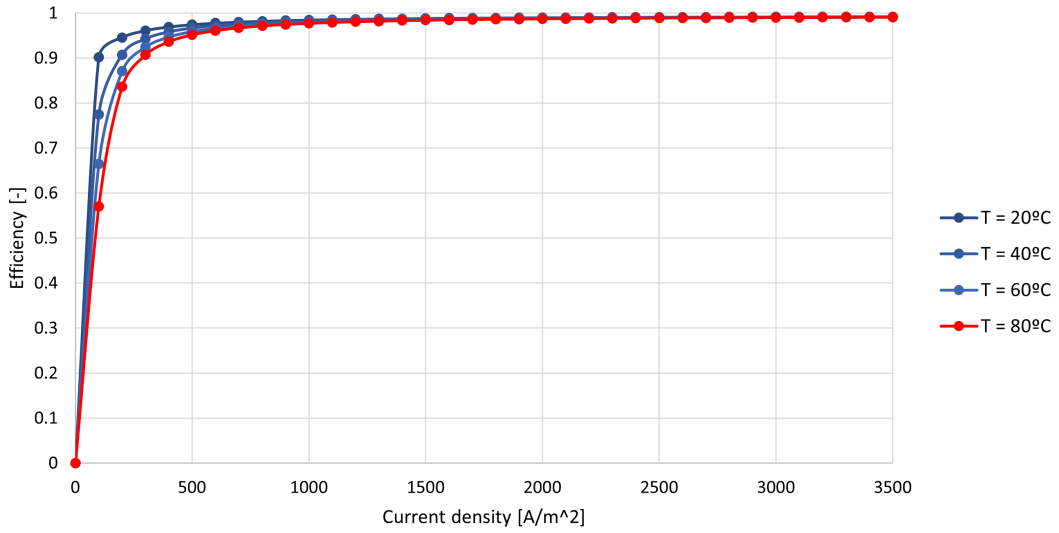

Figure 4.2: Faraday Efficiency.

4.2 Power increase from kW electrolyzer to MW-level

To scale up the electrolyzer, it was necessary to find a suitable candidate among different manufacturer catalogues. The chosen manufacturer was Nel Hydrogen given its dominant position in the market together with Cummins and Siemens Energy [64], as well as their products similar operation characteristics with the 26 kW PHOEBUS electrolyzer as shown in Table 4.3. Another criteria was that this company offers modular products like module A3880 which consists of 8 stacks-A485.

Table 4.3: Series A Nel Hydrogen Atmospheric Alkaline Water Electrolyser [44].

Specifications	A485	A1000	A3880	Units
Net Production Rate $\dot{n}_{H_2}$	300-485	600-970	2400-3880	Nm^3/h
$\dot{m}_{H_2}$	647-1046	1295-2094	5180-8374	kg/24 h
Production Capacity Range	15-100	15-100	15-100	%
Efficiency at Stack η	3.8-4.4	3.8-4.4	3.8-4.4	kWh/Nm^3
	42.22-48.88	42.22-48.88	42.22-48.88	kWh/kg
H_2 Purity	99.99	99.99	99.9	%
Delivery Pressure	1–200	1–200	1–200	barg
Dimensions	225	350	770	m^2
Ambient Temperature	2-35	2-35	2-35	°C
Electrolyte	25	25	25	% KOH
Operating Temperature	80	80	80	°C
H_2 outlet pressure	200–400	200–400	200–400	mm WG
after electrolyzer	0.02-0.04	0.02-0.04	0.02-0.04	barg

Since it was not possible to get more accurate data like the number of cells n_{series} or their voltage-current curves, some assumptions and deductions have been made to build the model. The logical derivation starts with the definition of power consumption P_{dc}, which can be expressed as

$$P_{dc} = V_{dc} I_{dc} = n_{series} E_{cell} A_{cell} J_{cell} \tag{4.3}$$

where V_{dc} and I_{dc} are the stack voltage and current respectively, each decomposed into their elemental components. In Table 4.3, it is given the hydrogen flow capacity $\dot{m}_{H_2}$ which determines the product of number of cells times maximum current ($n_{series} * I_{max}$) using Faraday's Law (3.24). Lastly, it is plausible to consider that all Series A modules are agglomerations of A485, which can be induced by comparing their production rates as indicated in Table 4.4.

Table 4.4: Deductions of Series A.

Module	N° stacks	$\dot{m}_{H_2}$ [kg/s]	$n_{series} * I_{max}$ [kA]
A485	1	0.012	1168.541
A1000	2	0.024	2339.761
A3880	8	0.097	9351.004

Same as in Figure 4.1, it is selected an individual cell voltage E_{cell} of 1.8 V at operating temperature and maximum current density J_{max} of 3500 A m^{-2}. Lastly, it is assumed 500 cells for n_{series} and an electrode cell area A_{cell} of 0.6 m^2. For stack A485, this results in the ratings described in Table 4.5.

Table 4.5: A485 assumptions and operation ratings.

Assumptions		Results	
Temperature, T	80°C	Nominal voltage, $U_{dc,nom}$ (80°C)	900 V
Max. current density, J_{max}	3500 A m^{-2}	Max. voltage, $U_{dc,max}$ (25°C)	1050 V
Cells in series, n_{series}	500	Max. current $I_{stack,max}$	2100 A
Area, A_{cell}	0.6 m^2	Nominal power, $P_{dc,nom}$ (80°C)	1.9 MW
Cell voltage, E_{cell} (80°C)	1.8 V	Max. power,$P_{dc,max}$ (25°C)	2.2 MW

In Figure 4.3, a visual comparison is made between the 26 kW electrolyzer used in the PHOEBUS demonstration plant and the 1.9 MW Nel Hydrogen A485 electrolyzer.

(a) 26 kW electrolyzer used in the PHOEBUS demonstration plant [65].

(b) Nel Hydrogen Alkaline Electrolyzer A485 [44].

Figure 4.3: Scale-up from kW to MW level electrolyzer.

4.3 Dynamic Model Implementation in PowerFactory

Once the specifications for the model were defined, it could be developed in PowerFactory. The aforementioned article, published by an IEEE team of Aalborg University in 2013 [62], served as guideline for the implementation of AWE in DIgSILENT PowerFactory. The book "Modelling and Simulation of Power Electronic Converter Dominated Power Systems in PowerFactory" [66] written by Francisco M. Gonzalez-Longatt and José Luis Rueda Torres was also used as literature reference for developing models in DIgSILENT.

The model definition prompted the need for substantial troubleshooting efforts, given the operational challenges of the software. Also many approaches were taken, but finally only two designs were considered for its implementation:

- General load (Model 1): simulating the whole system as a general AC load where it is possible to tune the active P and reactive power Q independently to control the power flow. This solution was based on article [62].

- Converter + voltage source (Model 2): locating a current i_{pu} controller in the converter and implementing the IU curves in the voltage source block.

Model 1 allows voltage dependence of the load when performing load flow calculations since the whole system (rectifier and electrolyzer) is a "black-box" or PQ load. This setup allows dynamic simulation known in PowerFactory as RMS simulation, but not instantaneous analysis of waveforms inside the rectifier or EMT simulation. In their article [62], Iker Diaz de Cerio Mendaza, Birgitte Bak-Jensen and Zhe Chen implemented the model assuming that the sole demand of reactive power is the one consumed by the compressor. This is not general, since it depends heavily on the converter topology and varies depending on the loading as described in Chapter 5. The power quality definition of the load can be introduced to change the converter type. Overall, this model enables good and fast analysis of the load.

On the other hand, Model 2 enables a more thorough and comprehensive understanding of the system by segregating both the power electronics and the load. It is very suited for dynamic simulation (RMS) and enables the possibility of analyzing the instantaneous spectrum of the rectifier (EMT) and to change the harmonics contents produced by different types of rectifier topologies (6-pulse thyristor, 12-pulse thyristor, PWM with IGBT). However, it supposes an independent handling of the load flow analysis and the dynamic behavior in RMS/EMT simulation.

Both models are recommended for implementation in future projects, but this thesis will be based on the second option. System modelling for stability and electromagnetic transient analysis (RMS/EMT) is a critical issue in the power system analysis. Given this level of complexity in time-domain simulations, PowerFactory modelling philosophy presents a strictly hierarchical system modelling approach, which combines both graphical and script-based modelling methods. The basis for this modelling approach is presented in the following points, from the highest level to the lowest one:

- In the highest level it is found the "composite models". These objects are defined by a "composite frame", which combine and interconnect "built-in models" and "common models". In simpler words, the composite frames are a type-file which enables to reuse a basic structure for a composite model.

- "Built-in models" are the transient PowerFactory models for standard equipment, i.e generators, motors, loads. The "common models" are based on "DSL block definitions" and are the front-end of the user-defined transient models.

- The "DSL block definitions", based on the "DIgSILENT Simulation Language" (DSL), form the basic building blocks to represent transfer functions and differential equations for the control systems.

For terminology purposes, **AWE or electrolyzer system** will be referring to the whole module: converter and electrolyzer. In Figure 4.4, it is shown the AWE system composite frame, which includes all necessary blocks for building the model:

- Measurement devices like phase-locked loop or PLL (.ElmPhi), current measurement (.StaImea) and, since this project does not count with a thermal model, a reference block for pressure and temperature (.ElmDsl).
- Model Definitions like the current controller (.ElmDsl), the AWE IU curves (.ElmDsl) and the hydrogen production block (.ElmDsl).
- Two built-in models to represent the voltage source (.ElmDcu) and the rectifier (.ElmRecmono).

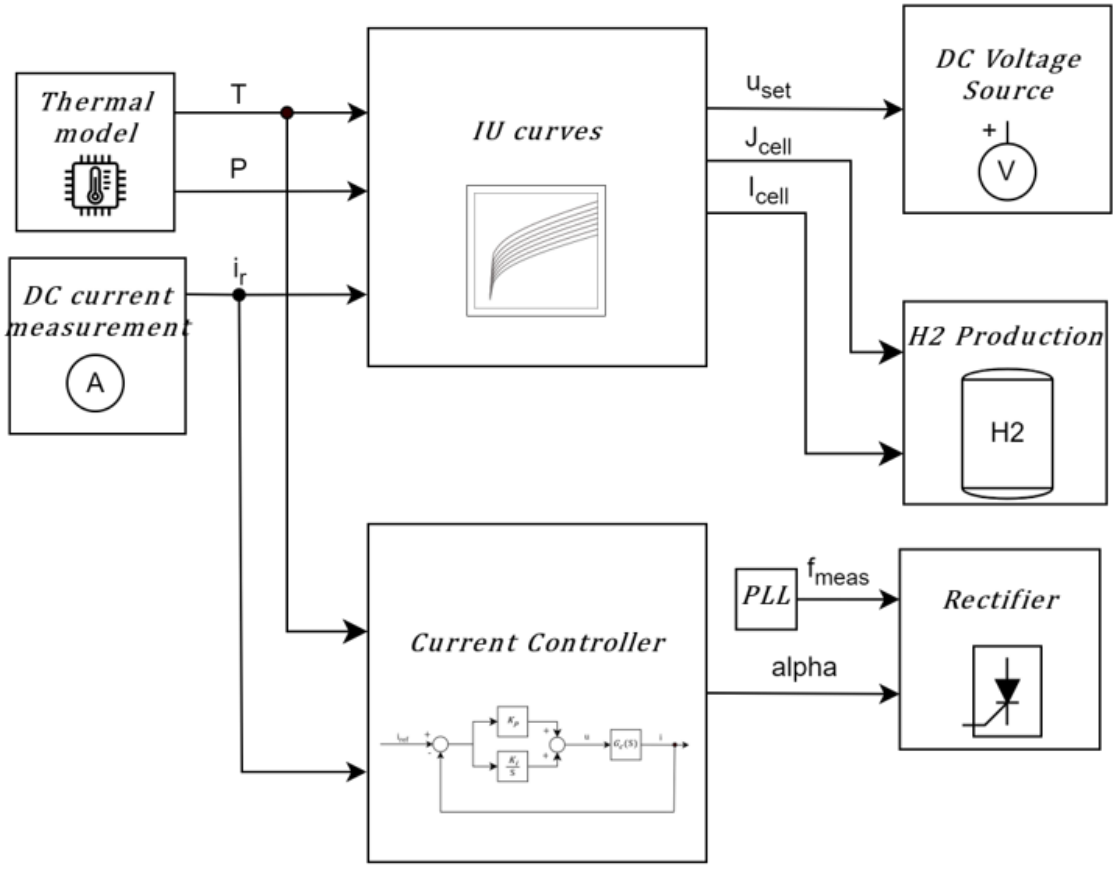

Figure 4.4: AWE system composite frame (BlkDef. Test Voltage Source).

Diving into the AWE IU curves block definition: this module gets the operating temperature T and pressure P as inputs which allows to determine the operating IU curve, the reversible E_r and thermoneutral potential E_{th}. With the last two properties it is possible to calculate the instantaneous efficiency of the electrolyzer η_{LHV} and η_{HHV}. However, the IU curves are not implemented using the equations of subsection 4.1 since the objective of this script is to be repeatable for other electrolyzers with different curves. Instead a look-up table is used with temperature T and current density J_{cell} as inputs. All these schematics are illustrated in Figure 4.5.

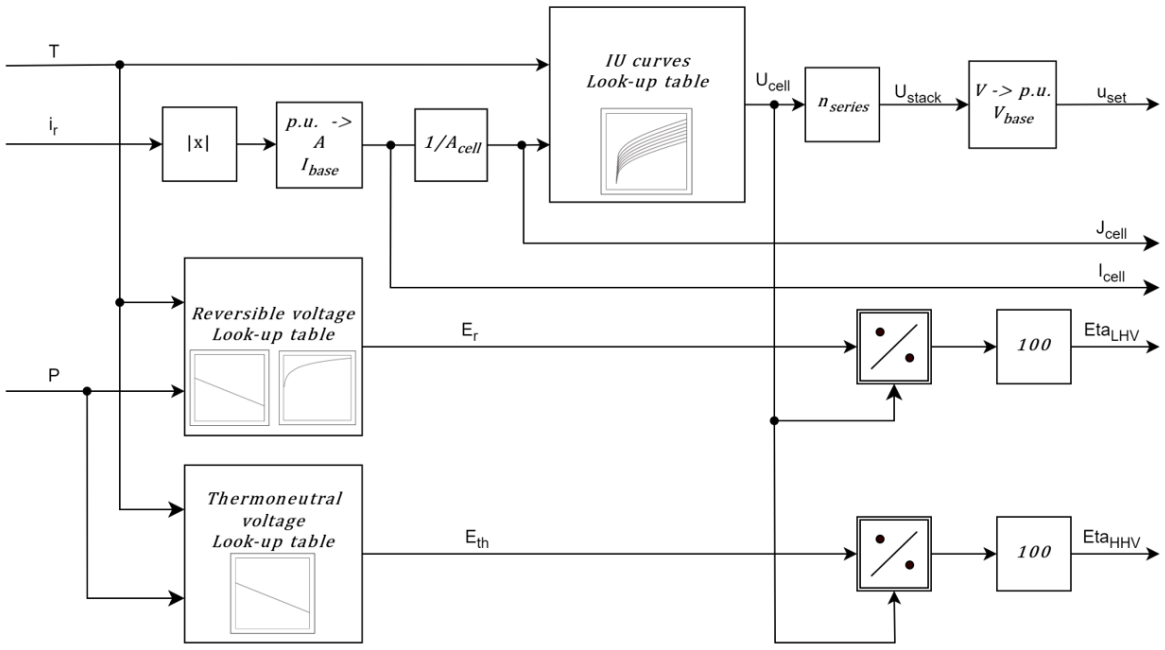

Figure 4.5: AWE IU curves block (BlkDef. IU curves).

An important point to highlight is that the current measurement i_{pu} is defined per unit, but the look up table for single cell IU curves is not, so per unit conversion is required. Afterwards, i_{pu} is converted to its absolute value due to the DC voltage source (.ElmDcu) sign criteria. Conversion back to per unit is done with the voltage U_{stack} at the output. At the composite frame Figure 4.4, this value u_{set} is introduced into the "Voltage Load Slot", where this value updates the voltage source element.

Finally, the current density J_{cell} and cell current I_{cell} measured in standard units are taken as input for the hydrogen production block (BlkDef. Faraday Law). As observed in Figure 4.6, the left block applies Faraday's law with only current as input and gives the mass flow $\dot{m}_{H_2}$ in kg/s. The look-up table below gives the Faraday efficiency using the curves of Figure 4.2. Finally, the mass $\dot{m}_{H_2}$ and volume $\dot{n}_{H_2}$ flow, expressed in kg/h and Nm^3/h respectively, are obtained applying hydrogen density at atmospheric pressure.

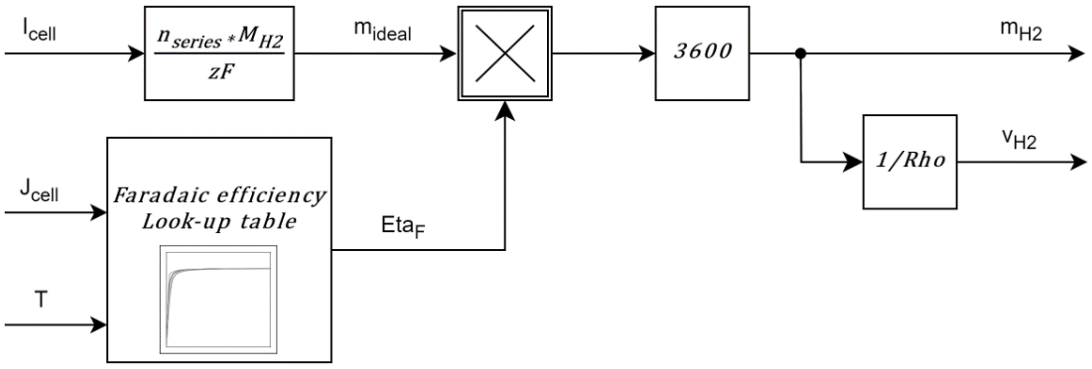

Figure 4.6: Hydrogen production block (BlkDef. Faraday Law).

Lastly, the block definition of the current controller is presented in the following sections.

5

Converter-load interaction and control

The AWE IU curves and H_2 production model definitions developed in section 4.3 are valid independently of the converter topology. This fact, besides the dependence of the converter technology on the semiconductor topology, makes it necessary to dedicate this part a separated section. Before delving into the controller design, a concise preliminary study has been conducted. Electrolyzers require high current rectifier topologies to operate: at least 2.1 kA DC for the model at hand, so only some technologies are evaluated.

5.1 Prestudy

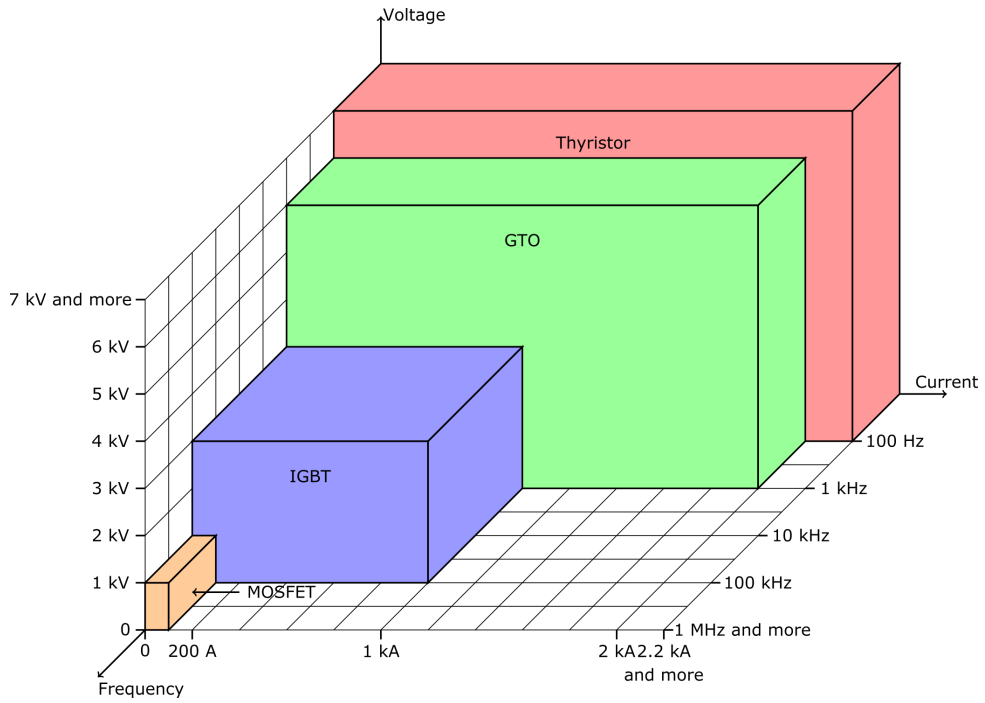

Figure 5.1: Active Components Ratings in Power Electronics [67].

It is possible to classify rectifier topologies into three categories depending on its semiconductor technology: diode, thyristor and IGBT based.

Diode-based rectifiers are typically overlooked since they are non-controllable devices. Nontheless, there is a viable approach involving diode rectifiers in conjunction with a

DC/DC converter to achieve voltage regulation [68]. Such systems, referred to as rectifier-DC choppers, find extensive use in applications with power ratings in the kilowatt range but prove inadequate for megawatt-level tasks. This leaves only rectifiers based on thyristors and IGBTs for further examination. Figure 5.1 depicts the limits of voltage, current and frequency across various semiconductor technologies employed in power electronics.

The thyristor stands out as the dominant component in managing high electrical loads. It excels in handling voltages exceeding 8 kV and currents surpassing 2.2 kA. Nevertheless, they are slow devices with switching frequencies no exceeding 100 Hz. Semi-controllable in nature, the thyristor can be activated at will but does not have turn-off capabilities.

In contrast, the IGBT emerges as an active component without the drawbacks of thyristors. However, its proficiency in handling voltage and current is comparatively restricted. For applications demanding high voltage, the solution often entails stacking several IGBTs in series within modular converters.

Currently, thyristor-based rectifiers dominate the market including industrial and Power-to-Gas applications. They are mature technologies that offer high efficiency, reliability and good control of the current, but unfortunately, they suffer from degrading the power quality of the AC grid by injecting low-frequency harmonics, consuming undesired reactive power and having high DC current ripple. Its standard converter is the 6 pulse thyristor-based rectifier (6-PTR).

There are multiple configurations to decrease the thyristor line RMS current as well as the low-frequency harmonics and output current ripple: 12-pulse, 24-pulse, 48-pulse, double-star rectifier [68].

Noteworthy progress has been achieved in the realm of IGBTs for medium-voltage and power applications, leading to their integration into PWM current source rectifiers (PWM-CSR). However, this configuration proves unsuitable for high-power applications, mainly due to the substantial voltage and current demands that elevate conduction losses, ultimately undermining energy efficiency.

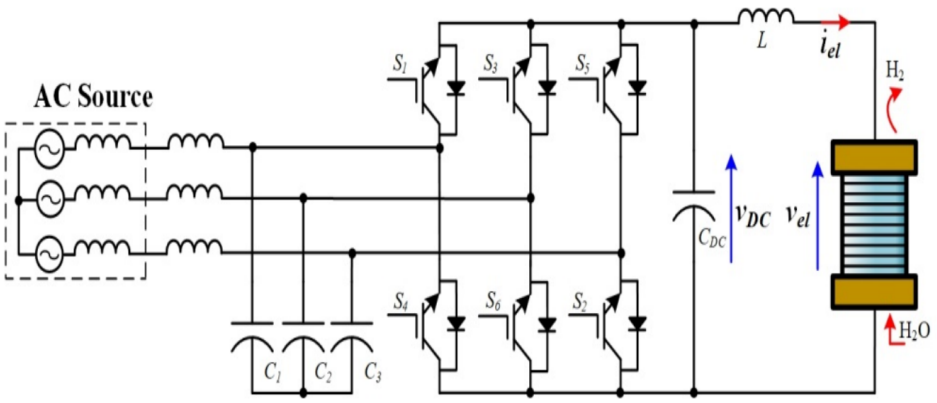

Figure 5.2: PWM-CSRs [68].

To compensate these disadvantages usually multilevel converters are implemented. An example is the three-level Neutral Point Clamping (NPC) converter shown in Figure

5.3. These converters utilize multiple voltage levels to achieve efficient power conversion. However, they suffer from increased high voltage and current stress, which leads to higher conduction losses and reduced energy efficiency compared to thyristor-based rectifiers. Other options include the Modular Multilevel Converter (MMC) with half-bridge or H-bridge modules [67].

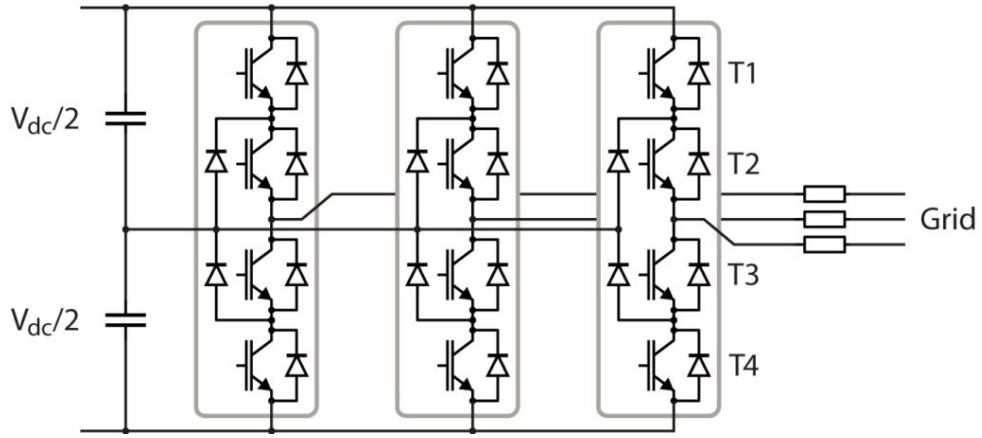

Figure 5.3: Three-level Neutral Point Clamping converter.

In essence, there are two primary configurations available for rectifiers: those based on thyristors and those utilizing IGBT power electronics. In modern applications, where power quality and harmonic mitigation are critical, more advanced converter topologies such as active front-end converters or multilevel converters are preferred.

It is anticipated that IGBT converters will exhibit competitive costs compared to thyristor-based solutions in the future since they are exempt of needing harmonic-tuned filters to comply with emissions regulation and reactive power compensation devices. Nevertheless, thyristor-based rectifiers remain the preferred option for MW-level electrolyzer applications due to their superior efficiency and reliability resulting from the utilization of fewer components and its higher ratings [69],[70].

5.2 Power converters in PowerFactory

As it was commented in section 4.3, there are two main possibilities to model the whole electrolyzer system: decoupling the power electronics and DC behavior or modeling the whole as a general load with a predetermined level of harmonics. Since it was decided to follow the first alternative, next step in the modeling process is to implement the converter and the controller behind it.

There are various alternatives available to implement converters in PowerFactory, as depicted in Figure 5.4. The highlighted elements displayed in the image below enable the modeling of different types of converter topologies, unlike the unmarked ones, which represent specific topologies of their own, such as HVDC, Softstarters, TCSC and SSSC.

- Rectifier/Inverter (.ElmRec, .ElmRecmono)
- PWM Converter (.ElmVsc, .ElmVscmono)
- DC-DC Converter (.ElmDcdc, .ElmDcdcbi)

- DC Valve (.ElmValve)

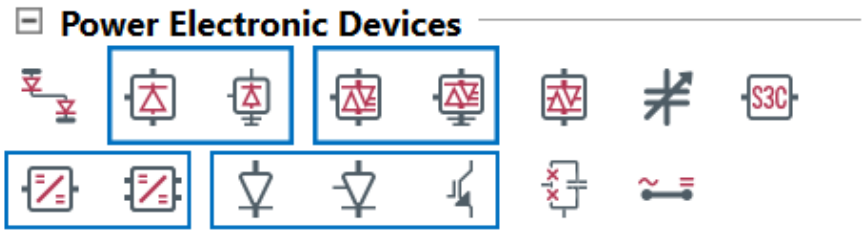

Figure 5.4: Power Electronic Devices available in PowerFactory.

The converter implemented in this thesis is AC-DC type, thus excluding the study of the DC-DC Converters. As the intention is to utilize a prebuilt version of the converter, the examination of individual DC valve elements such as diodes, thyristors and IGBTs is omitted. Therefore, only two options follow:

- The Rectifier/Inverter can be modeled either as a full-bridge diode rectifier or a 6-pulse thyristor converter (selection as rectifier or inverter orientation).
- The PWM Converter model which can be configured to represent both a self-commutated, voltage source AC/DC two-level converter or modular multilevel converter.

Model Definition type .ElmRec allows three kinds of model for rectifier implementation:

- Three-phase diode rectifier: this option is disregarded since it is an uncontrolled rectifier topology, which gives no regulation over the hydrogen production.
- Three-phase line-commutated (LCC) rectifier/inverter: this model is the preferred choice since it is the standard topology for 6-PTR and the most robustly designed and controlled.
- Three-phase capacitor-commutated (CCC) rectifier/inverter: this configuration is the same as the LCC but with series capacitors between thyristors and the commutation reactances. This topology allows to advance the commutating voltage over the thyristors, resulting in a lower firing angle and therefore drawing less reactive power of the grid. However, it has a difficult design and resonance phenomena to consider, not the best model for a prototype.

5.3 6 and 12 pulse three phase thyristor-based rectifiers

The "6-pulse" designation refers to the arrangement of six thyristors in the rectifier circuit. These thyristors are semi-controlled switches that allow current to flow in only one direction, effectively rectifying the AC input into a smoother DC output. The arrangement consists of three pairs of thyristors, forming a three-phase full-wave bridge rectifier configuration. This converter corresponds to the LCC rectifier described before and shown in Figure 5.5.

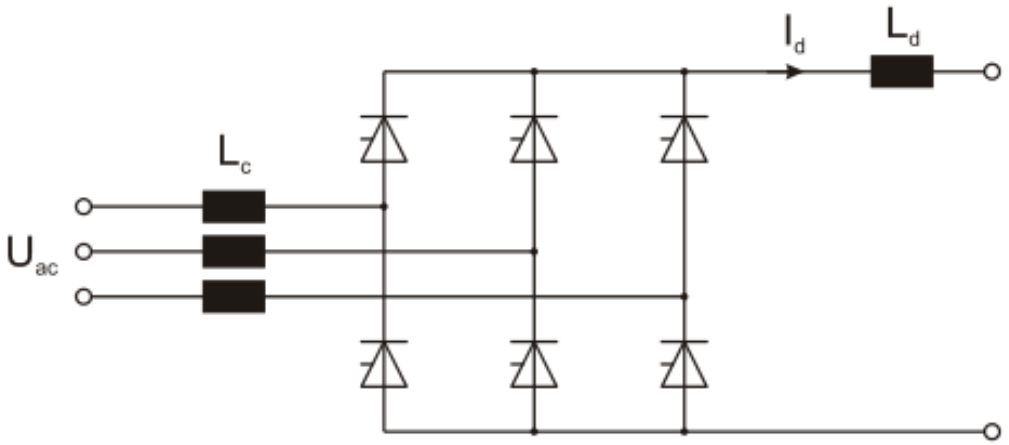

Figure 5.5: PowerFactory three-phase LCC rectifier model.

This converter is often connected to grid through a step-down transformer and its leakage inductance usually represents most of the commutation inductance L_c. The rectifier is connected to a DC load through the inductance L_d intended to reduce the current ripple.

Assuming the case for an uncontrolled 6-PTR which would correspond to a three phase full-wave bridge diode rectifier, it is possible to define the "ideal no-load DC voltage" V_{d0} in equation (5.1) being V_{LL} the rms line to line voltage.

$$V_{d0} = \frac{3\sqrt{2}}{\pi} V_{LL} \approx 1.35 V_{LL} \tag{5.1}$$

The thyristors are turned on and off at specific times to control the flow of current through the circuit. However, current must reach zero by itself for turning-off the switch which disables the use of pulse width modulation (PWM). Instead, the current flowing through each thyristor can be delayed using the ignition angle α which determines the DC voltage.

$$V_{d\alpha} = V_{d0} \cos \alpha \tag{5.2}$$

Nonetheless, to reflect more realistic converters the voltage drop ΔV_d caused by current commutation from one valve to the next one must be contemplated.

$$V_d = \frac{3\sqrt{2}}{\pi} V_{LL} \cos \alpha - \Delta V_d = \frac{3\sqrt{2}}{\pi} V_{LL} \cos \alpha - \frac{3\omega L_c}{\pi} I_d \tag{5.3}$$

Notice that if the ignition angle becomes bigger than 90º, the DC voltage turns negative where it enters into the inverter mode. Since for our application it is only desired the rectifier mode, α will always operate in the range [0, 90º] providing maximum active power at low firing angles and minimum active power at high firing angles.

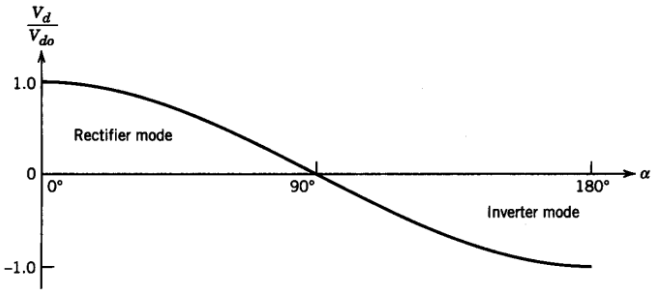

Figure 5.6: Normalized DC voltage V_d/V_{d0} as function of the firing angle α assuming no commutation inductance L_c [71].

In Figure 5.7, the instantaneous AC voltage, AC current, DC voltage, firing angle α and commutation angle μ corresponding to the operation of the converter are presented. It can be appreciated the transition of the currents with the commutation angle and its effect on the DC waveform and its average V_d.

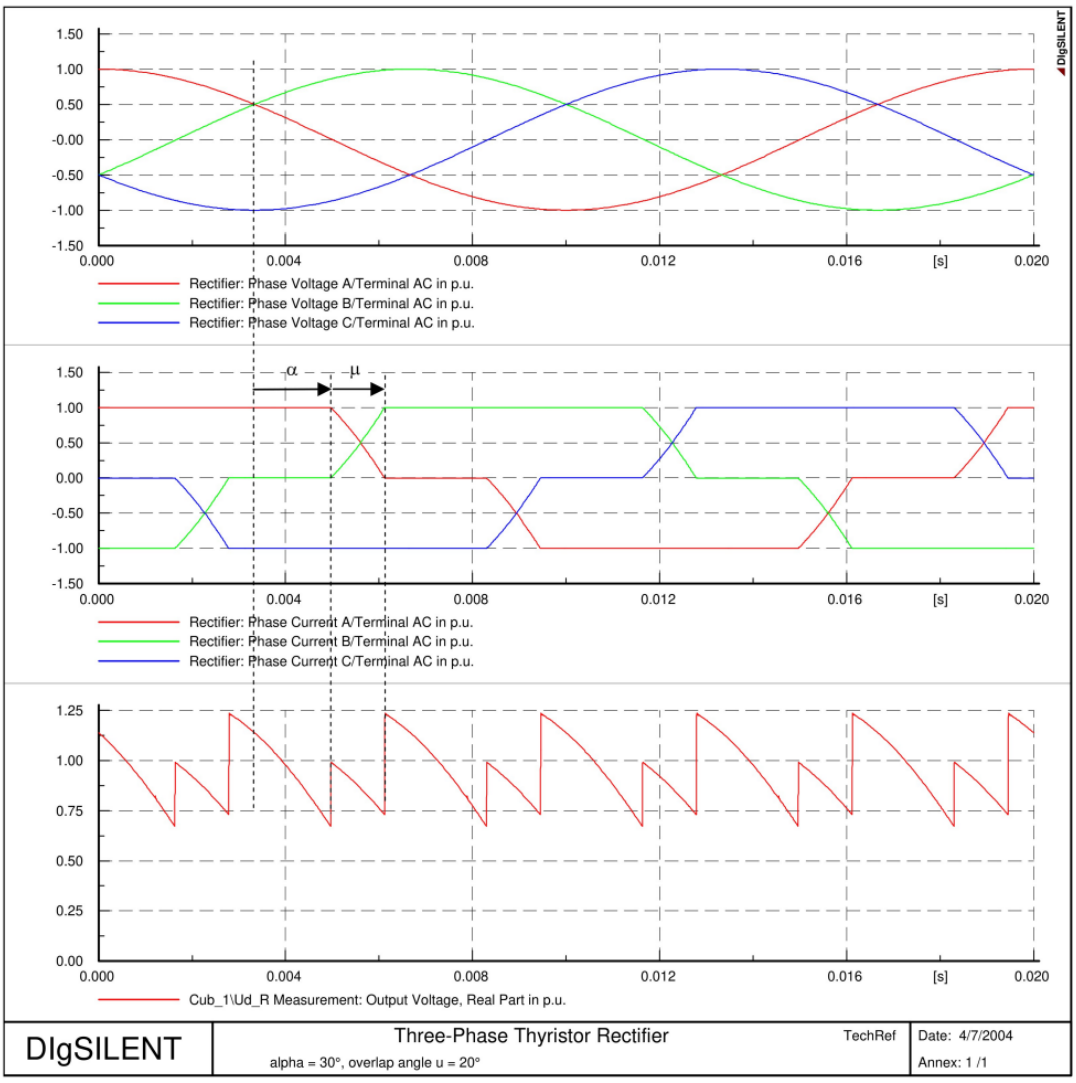

Figure 5.7: Phase voltages, currents and DC voltage of a 6-PTR working with a firing angle α=30º and a commutation angle μ=20º.

The current waveforms exhibit an ideal rectangular shape when disregarding the commutation angle μ. Assuming his idealization, a Fourier decomposition of the currents into their harmonic components will be done. In the context of a single-phase rectifier, the rectangular waveform is broken down into its odd harmonics. However, in the case of a three-phase system, all third-multiple (3h with h $\in \mathbb{N}$) or zero sequence current harmonics vanish. Consequently, what remains are the non-triple odd harmonics (6h$\pm$1 with h $\in \mathbb{N}$). Each of these possesses a value inversely proportional to its harmonic order and is characterized by its fundamental value as described in equation (5.4) for phase A.

$$\hat{I}_{A(1)} = \frac{\sqrt{6}}{\pi} I_d \qquad \hat{I}_{A(h)} = \frac{\hat{I}_{A(1)}}{h} \tag{5.4}$$

Implementing a 6-PTR for a high current load, like an AWE system, becomes impractical given the magnitude of its harmonics [71]. Fortunately, there is a simple cancellation technique for some of these low frequency harmonics which consists into parallel two 6-PTR with a 30º phase shifted three-winding transformer. The transformer must have a Yy0 and Y$\triangle$11 winding configuration with a turn ratio 1:$\sqrt{3}$:1 as shown in Figure 5.8.

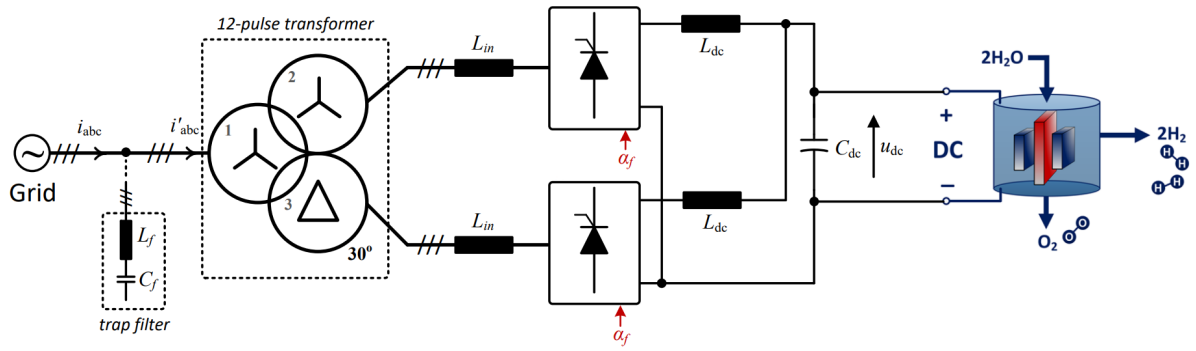

Figure 5.8: 12-pulse thyristor rectifier [70].

The implementation of a 12-PTR allows to cancel those harmonic orders 6h$\pm$1 with h = 1, 3, 5 ... This is shown in Figure 5.9 and it is also compared the ideal harmonic distortion distribution in 6 and 12-PTR. The non-cancelled harmonic orders are 12h$\pm$1 with h $\in \mathbb{N}$, which are typically managed with specific harmonic-tuned filters.

In Figure 5.9, the applied harmonic distortion distribution presents a lower value than the ideal scenario for the non-cancelled harmonic orders (11^{th}, 13^{th}, 23^{rd}, 25^{th}...), but not a complete cancellation for the rest. The main explanation is that the current does not present a perfect square-step waveform caused by the commutation angle μ and the parasitic components of the thyristors. Another factor to consider in the 12 PTR topology is that both bridges may not switch exactly as intended in the controller, which introduces a relative small time error that also affects the current waveform. Overall, the applied Total Harmonic Disorder (THD) results in a lower level than the ideal, as indicated in Table 5.2. The THDs presented in this table are calculated until the 50^{th} harmonic order.

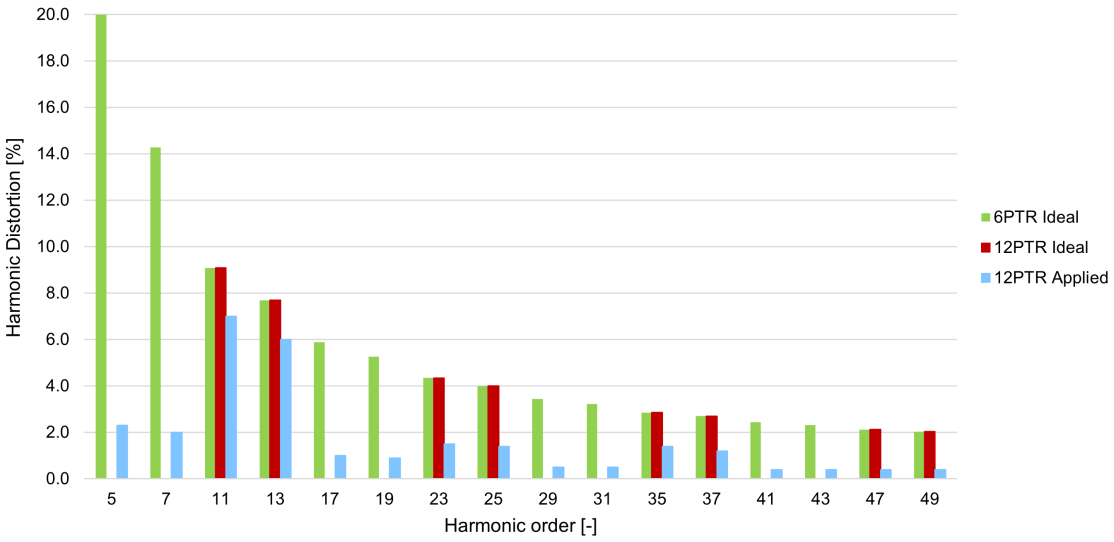

Figure 5.9: Harmonic distortion distribution for 6 and 12-PTR topologies.

Since the categorical difference between a 6 and 12-PTR is the harmonic distortion distribution of the current, the 12-PTR can be simulated in PowerFactory as an equivalent 6-PTR but manipulating the harmonic contents. The table implemented in the model is described in Table 5.1.

Table 5.1: Implemented Harmonic Distortion in 12-PTR [72].

Harmonic	HD [%]	Angle [º]	Harmonic	HD [%]	Angle [º]
5	2.3	0	29	0.5	0
7	2	0	31	0.5	0
11	7	-4.4	35	1.4	215.6
13	6	-8.3	37	1.2	201.7
17	1	0	41	0.4	0
19	0.9	0	43	0.4	0
23	1.5	285.8	47	0.4	488.5
25	1.4	269.3	49	0.4	477.5

Table 5.2: Total Harmonic Disorder (THD) for 6 and 12 PTR topologies.

Rectifier	THD
6-PTR Ideal	30.02%
12-PTR Ideal	14.17%
12-PTR Applied	10.24%

The topology and the rectifier operating principles have now been explained, so in the rest of the sections, the system is studied with rms values to develop the current controller. The electromagnetic transient (EMT) operation of the converter is left out of the scope from a control point of view.

5.4 Controller Implementation

Since the primary objective of the plant is to control the hydrogen production $\dot{m}_{H_2}$, this is the reference input of the controller. Besides, given its direct proportionality with the DC current I_{dc}, both variables have the same values in per unit. In fact, the desire of having the same controller independently of how many stacks are put in parallel or series makes a per unit controller the ideal solution. In the next subsections, a proportional-integral (PI) controller for the hydrogen flow is designed using the Internal Model Control (IMC) tuning method [73]. This process has 3 design steps:

1. Process model
   - Describe the process with equations
   - Estimate the process with measurements
   - Verify the process model
2. Controller design
   - RL circuit control
   - Feed-forward and anti-windup introduction
3. System analysis
   - Is the system behaving as expected? Testing and validation

5.4.1 Process model

This part entails to describe the behavior of the process model, in this case, the electrolyzer. This device is far from a simple electric circuit model as described in a previous section, but to design the hydrogen controller some simplifications are made. The electrolyzer process model is considered as a simple resistance in series with a voltage source, although this assumption ignores the activation losses. Two linear process models are proposed as candidates to design the controller with different slopes and y-intercepts.

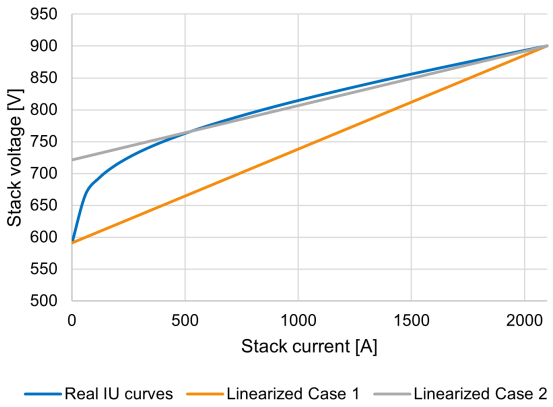

(a) Comparison.

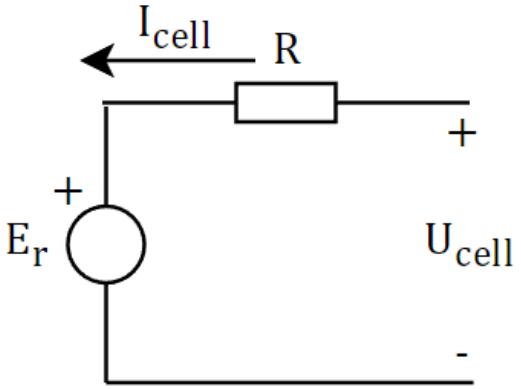

(b) Equivalent circuit.

Figure 5.10: Analogy of electrolyzer with resistance and voltage source.

5.4.2 Controller design

As mentioned before, the reference input for the controller is the objective DC current in per unit $i_{ref,pu}$. This value corresponds also to the hydrogen production $v_{H_2,ref,pu}$ established by Faraday's Law as well as the electrolyzer's loading.

This controller works based on average and DC values, ignoring the electrical transient nature of a rectifier with instantaneous variations like current ripples. In Figure 5.11, it is shown the PI controller for a RL circuit represented by the transfer function $G_c(S)$.

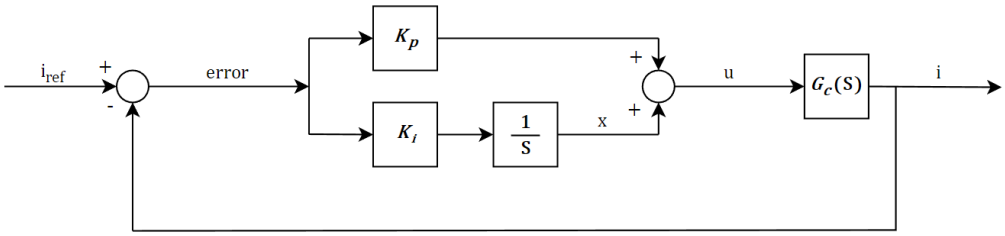

Figure 5.11: Current controller for RL circuit.

Nevertheless, the electrolyzer $G_c(S)$ is not comparable to a RL circuit, it also has a reversible voltage E_r that acts like a disturbance D. In order to control the current as it would be for the RL circuit, a feed-forward $\hat{D}$ is introduced in the controller to remove the disturbance D. No active damping is implemented. This way, the closed-loop system $G_{cl}(S)$ is designed to behave like a first order system.

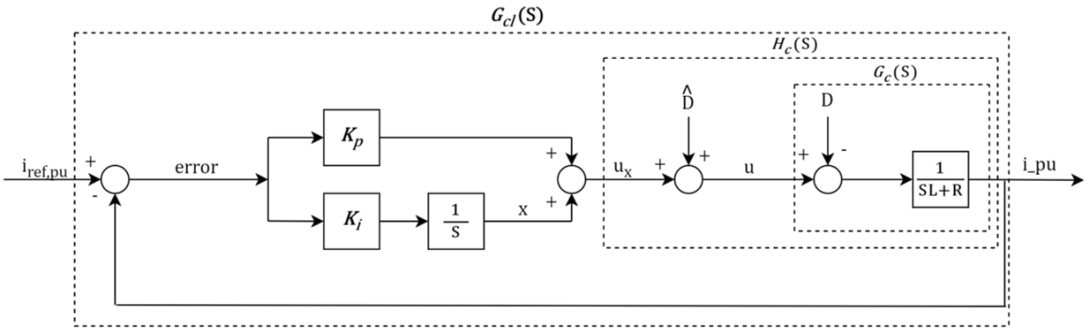

Figure 5.12: Introduction of feed-forward $\hat{D}$ in the current controller.

Another necessary implementation in the controller is the anti-windup. The converter is not an ideal source of DC voltage. It has a limit in the maximum deliverable output voltage V_{dc} which depends on the AC voltage of the grid. The conditional integration anti-windup method switches off the integral part of the controller to avoid windup effects when $y \geq y_{max}$ and $y \leq y_{min}$. As reference, it is implemented the PI block with an anti-windup limiter in accordance with the IEEE Standard 421.5-2016 [74] as described below

$$\begin{aligned}
&\text{If } y \geq y_{max} : y_o = y_{max} \text{ and } \dot{x} = 0 \\
&\text{If } y \leq y_{min} : y_o = y_{min} \text{ and } \dot{x} = 0 \\
&\text{Otherwise } : y_o = y = K_p y_i + x \text{ and } \dot{x} = K_i y_i
\end{aligned}$$

5.4.3 System analysis

Upon completion of the controller design, the subsequent step involves studying and validating the response of the closed-loop system $G_{cl}(S)$, but this time integrating the actual AWE system. Both the simplified schematic and real controller implemented in PowerFactory are illustrated in Figure 5.13 and 5.14, respectively.

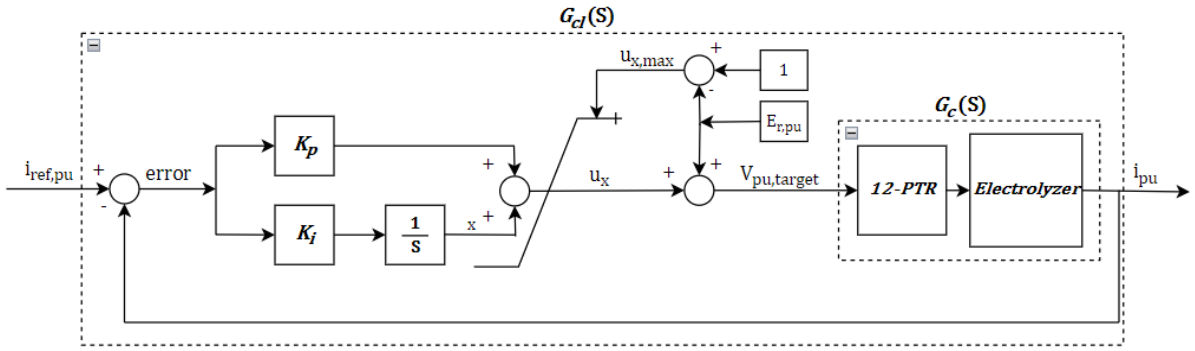

Figure 5.13: Proportional-integral current controller with feed-forward and anti-windup limiter.

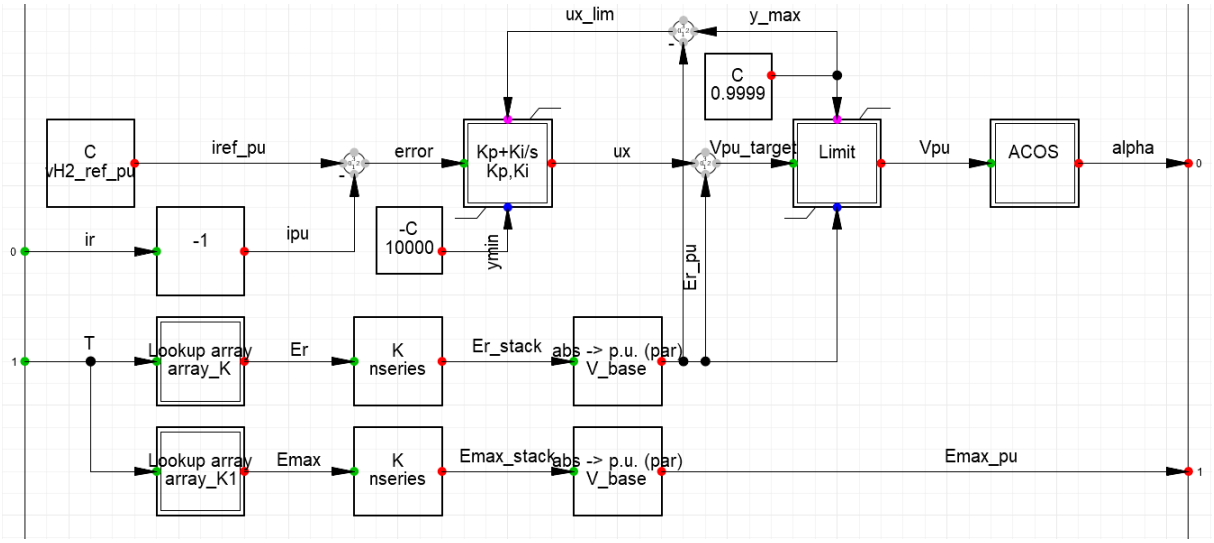

Figure 5.14: Current controller block definition (BlkDef. Current Control).

In Figure 5.14, it is shown that the current controller receives two inputs: the DC current measurement i_r and the operating temperature T. The controller provides two outputs: the rectifier's firing angle α and the maximum voltage in per unit $E_{max,pu}$.

Temperature T is used for calculating the reversible E_r and maximum E_{max} potentials at that given temperature. These potentials are then multiplied by the number of cells in series n_{series} and divided by the base voltage V_{base} to obtain per unit values.

The current reference $i_{ref,pu}$ gets subtracted by the DC current measurement i_r giving the total error. This value gets inside the PI controller with anti-windup, where boundaries are defined so $V_{pu,target}$, after feed-forward, gives a maximum voltage of 1 p.u. Afterwards, this voltage is transformed into the necessary firing angle α to obtain $V_{pu,target}$.

The IMC method is a robust approach for tuning controller parameters [73]. In this case, the proportional K_P and integral K_I constants can be tuned by considering the desired rise time t_{rise} for the closed-loop system $G_{cl}(S)$ and the circuit's resistance and inductance. Here, t_{rise} represents the time required to reach from 10 to 90% of $i_{ref,pu}$ and can be calculated using equation (5.5), where α_c denotes the system's bandwidth.

$$t_{rise} = \frac{ln(9)}{\alpha_c} \tag{5.5}$$

Two sets of control parameters may be implemented considering the two linear process models defined in Section 5.4.1. Both K_P and K_I can be calculated through equations 5.6 and 5.7 with l_{load} and r_{load} representing the inductance and resistance of the DC load in per unit. Since these variables are calculated in per unit, they must be divided by R_{base} which is 0.5 Ω, calculated with the electrolyzer maximum ratings.

$$K_P = l_{load} * \alpha_c \tag{5.6}$$

$$K_I = r_{load} * \alpha_c \tag{5.7}$$

For this electrolyzer model, the considered DC inductance L_{load} is null, which makes the proportional constant K_P zero for Case 1 and 2. This inductance must not be confused by L_d, DC inductance connected at each output of the thyristor rectifiers. The purpose of L_d is to reduce the voltage ripple output in an EMT environment, while L_{load} is the inherent inductance of the DC load, in this case the electrolyzer.

Additionally, a third case is suggested imposing a proportional constant K_P to compare the performance of the system despite the absence of inherent DC inductance. The control parameter sets are tabulated in Table 5.3.

Table 5.3: Candidates for final controller.

Parameter	Case 1	Case 2	Case 3
R_{load}	0.147 Ω	0.085 Ω	0.085 Ω
r_{load}	0.294 p.u.	0.171 p.u.	0.171 p.u.
t_{rise}	2 s	2 s	<2 s
K_P	0	0	0.1
K_I	0.32365	0.18756	0.18756
α_c	1.1 rad/s	1.1 rad/s	<1.1 rad/s

Applying these PI configurations and performing a ramp-up analysis, it is obtained three ramp-up scenarios, which represent the voltage and current at the DC side of the electrolyzer. All cases are performed with an operating temperature of 80°C.

In Figure 5.15 it is appreciated that all controllers, independently of their configuration, have a big time-delay in the first 0.2 p.u. step, and none of them fulfill the theoretical rise time t_{rise} of 2 seconds. This is due to the simplification of the load which ignores the logarithmic component of the voltage equation that represents the activation losses. Besides that, all controllers work adequately.

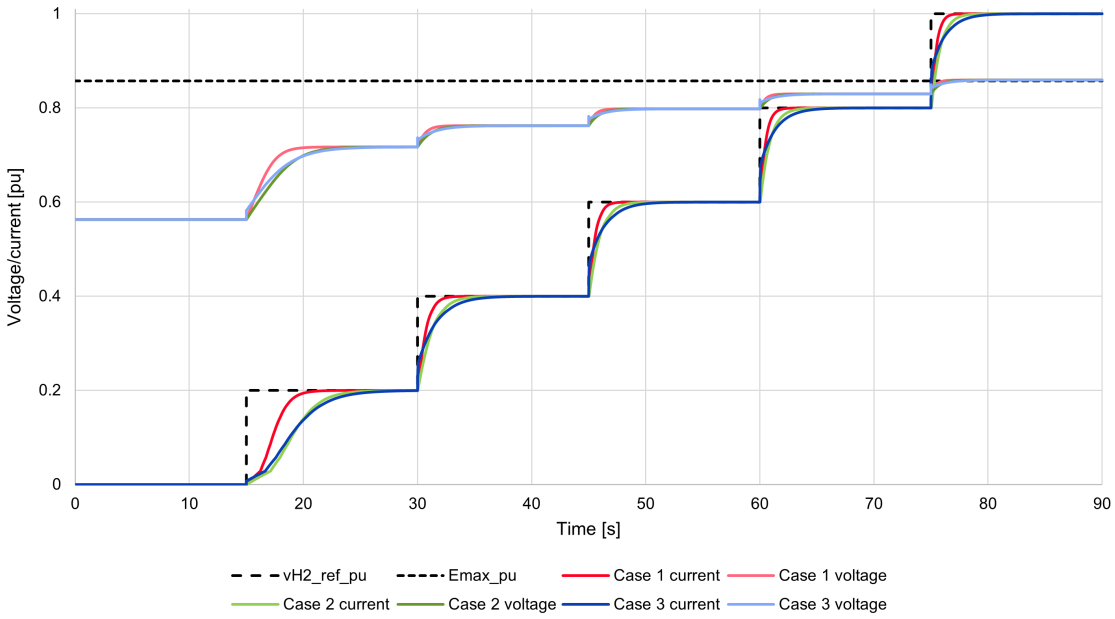

Figure 5.15: Time-domain response of the system with different PI parameters.

Case 2 uses the most simple first order response while adjusting to the real electrolyzer behavior, given the similarity of Process Model 2 to the electrolyzer, shown in the IU curves. These arguments lead to the design of an integral controller based on Case 2 parameters.

Another factor to consider in the system analysis is the temperature influence on the load. Two ramp-up simulations at ambient and nominal temperature are compared in Figure 5.16. As expected, operating at ambient temperature implies working at higher voltages to obtain the same desired hydrogen flow. The most noticeable contrast is the first 0.2 p.u. step, where the difference between activation potentials is the highest.

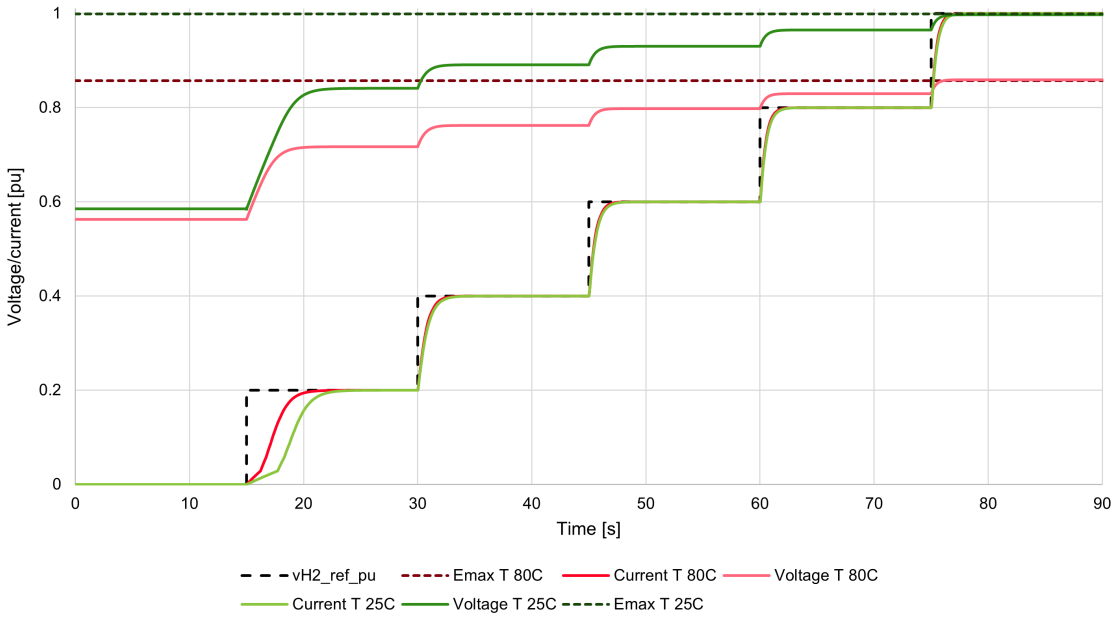

Figure 5.16: Time-domain response of the system with different operating temperatures.

The empirical rise time for each step using this controller is illustrated in Table 5.4. Due to the higher voltage requirements at 25°C, the integration of the current error takes longer to reach steady state compared to operating it at 80°C. This leads to a higher delay in the rise time at 25°C.

Table 5.4: Rise time at ambient and operating temperature.

i_{ref}	t_{rise} (25°C)	t_{rise} (80°C)
0-20%	4 s	3.13 s
20-40%	1.57 s	1.4 s
40-60%	1.23 s	1.13 s
60-80%	1.09 s	0.98 s
80-100%	1 s	0.92 s

The result of applying operating temperatures of 25°C and 80°C in the electrolyzer gives different firing angles α, as depicted in Figure 5.17. Operating at higher voltages implies lower firing angles due to the cosine function, introduced in equation (5.2).

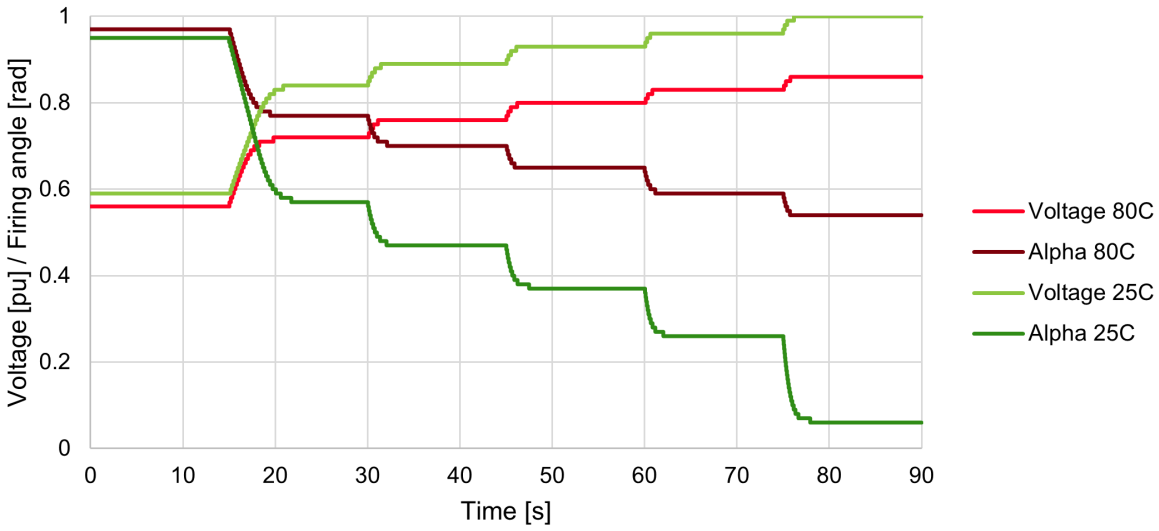

Figure 5.17: Stack voltage V_{pu} and firing angle α at different temperatures.

5.4.4 Power consumption analysis

Once the DC current and voltage are calculated and a ramp-up analysis has been made, the next step was to analyze the AC behavior of the AWE system. Three scenarios are simulated using the single line diagram (SLD) shown in Figure 5.18, where the active P_{AC} and reactive Q_{AC} power consumption of the rectifier is mapped by increasing the hydrogen production rate or loading.

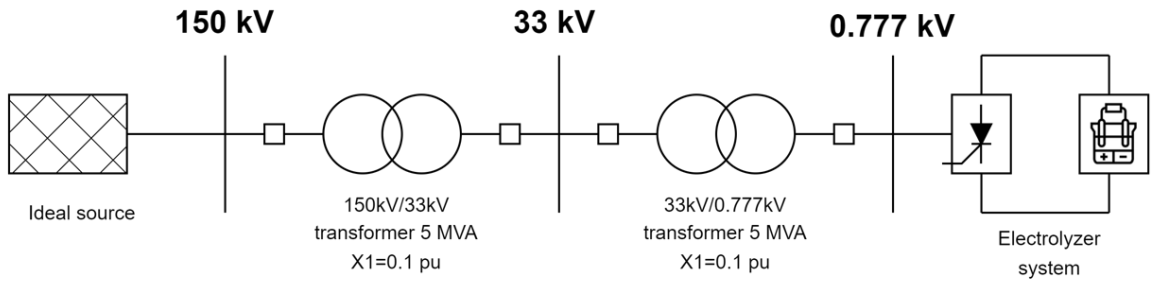

Figure 5.18: Grid single bus.

First and second scenario assume an ideal external grid with negligible leakage reactance in the step-down transformers and, therefore, no voltage drop across them. First scenario (dashed lines) assumes an operating temperature of 25°C while second scenario (bold line - blue) assumes 80°C. Finally, the third scenario (bold line - green) assumes a leakage reactance of 0.1 p.u. on each transformer and 80°C operating temperature. Second and third scenario share the same active power curve (bold line - red).

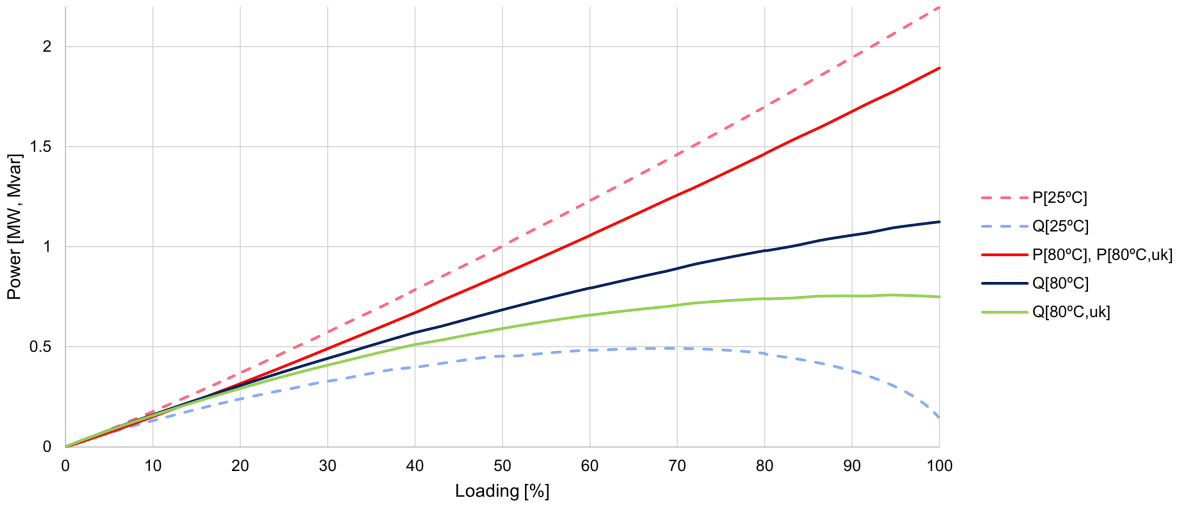

Figure 5.19: Active P_{AC} and reactive Q_{AC} power consumption as function of loading level.

Since switching and conduction losses are ignored for the converter, the consumption of active power in AC and DC sides is the same. It may be observed in Figure 5.19 that active power consumption P_{AC} reaches 2.2 MW and 1.9 MW for 25°C and 80°C, respectively. This is logical since the voltage at maximum loading in the IU curve for a single cell is 2.1 V at 25°C and 1.8 V at 80°C.

In terms of reactive power, the root cause of consumption in the rectifier is the firing angle α. As it can be observed in Figure 5.20, the regulation of the firing angle intrinsically delays the AC current which decreases the power factor PF. Additionally, in Figure 5.17 it can be observed that the higher the loading, the lower is the required firing angle. The reactive power consumption is the result of the multiplication of both factors, the AC current and sine function of the firing angle in the loading range.

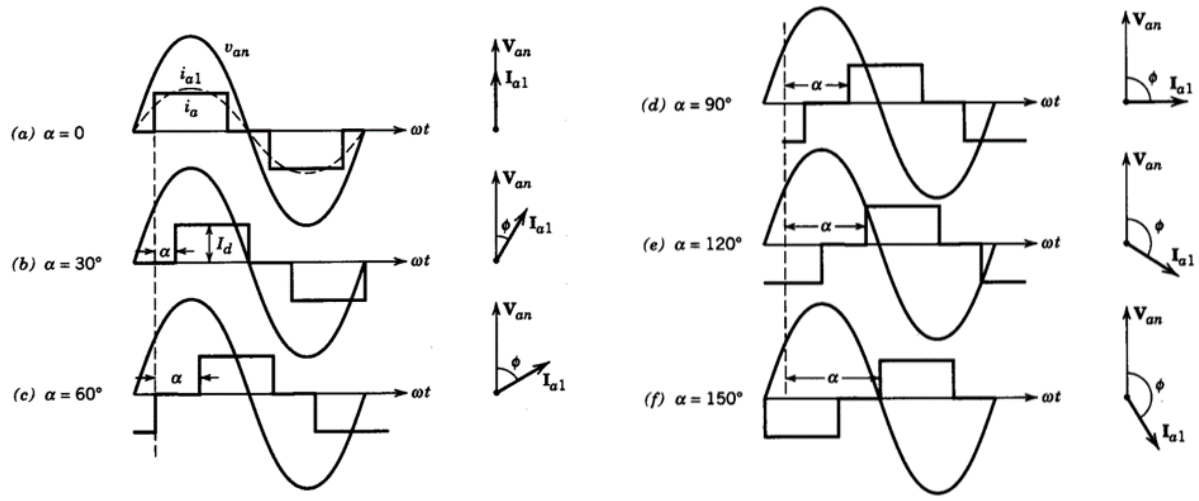

Figure 5.20: Line current wave-forms in a 6-PTR as function of firing angle α assuming no commutation reactance [71].

As already mentioned, the main difference between scenario 2 and 3 is the introduction of a reactance before the converter. It may be observed that Q_{AC} for scenario 3 is lower than for scenario 2. This is due to the voltage drop across the transformers reactances, which decrease the AC voltage at the rectifier bus. Maintaining the same current range, it decreases the reactive power consumption, but not the active power demand.

Lastly, a visualization of the stack efficiency in terms of η_{HHV} and η_{LHV} is shown below. Here it is visible the limitation of 15% as minimum operating limit for the electrolyzer due to the fact that, below this current density, the electrolyzer works at a lower voltage than the thermoneutral potential E_{th} which makes the electrolyzer an endothermic device. At this point, the electrolyzer is 100% efficient from a thermal analysis.

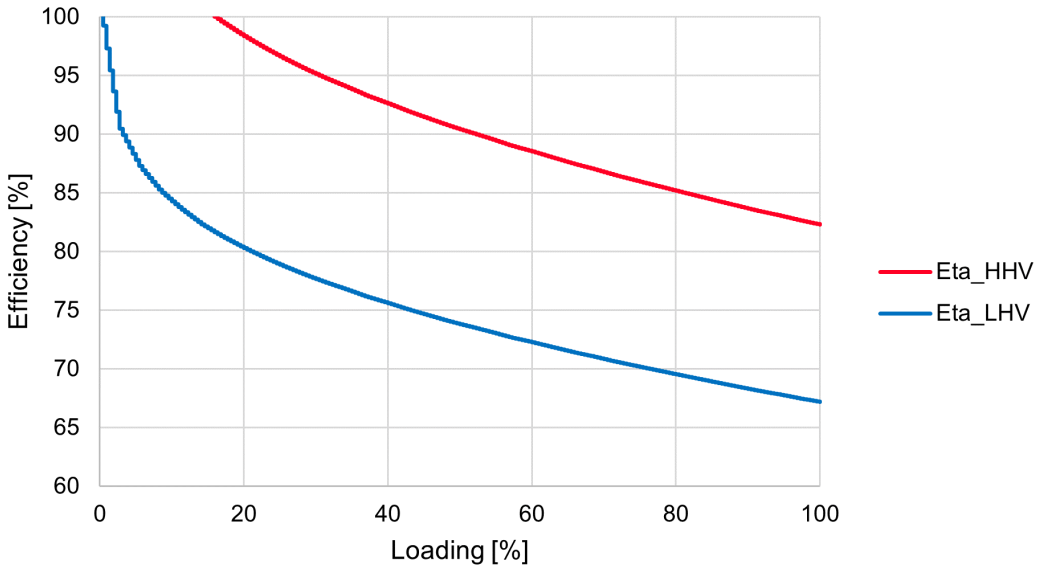

Figure 5.21: Efficiency Chart.

6

Structure Design for Electrolyzer stations at GW-scale

The technical design of the plant is based on two reference projects: *Electric infrastructure for electrolyser systems* thesis [56] and *Hydrohub GigaWatt-Scale Electrolyzer project* [69].

The first one presents the electric infrastructure of a station with state of the art technology using 3 voltages levels 400/150/(66 & 33) kV between the Point of Common Coupling (PCC) and a transformer-thyristor based rectifier module. On the other hand, the Hydrohub project includes a design with only 2 voltage levels 380kV/66kV between PCC and a transformer-IGBT based rectifier module.

Hydrohub project presents a global vision for building a GigaWatt green hydrogen plant considering not only the electrical installation, but process units, civil, structural works, piping, process automation and utilities. It also includes an economic evaluation of the project implementing both electrolyzer technologies, AWE and PEM, and providing anticipated investment cost estimations.

Nevertheless, the Hydrohub project is based on the assumption of having an "Advanced Design for 2030", which presumes technological advancements like IGBT enhanced characteristics, higher current densities and efficiencies for the electrolyzers enabling a reduction in the stack size and, therefore, in the station footprint. This thesis presents a compendium between both projects, as well as a more detailed plant design.

6.1 Station Design Criteria

The conventional power station is typically linked to a HVAC grid, specifically designed to accommodate extremely high loads like this case study. As a general rule, higher demand requires higher voltage to efficiently manage the current, thereby reducing losses.

Since electrolyzers are relatively-low voltage devices compared to the PCC voltage magnitude, it is necessary to provide a step-down infrastructure to connect the loads to the grid. For terminology purposes, this infrastructure is called distribution grid. They can be classified in three categories depending on the nature of the HV line and the connection of DC loads. These distributions grids are described in Figure 6.1.

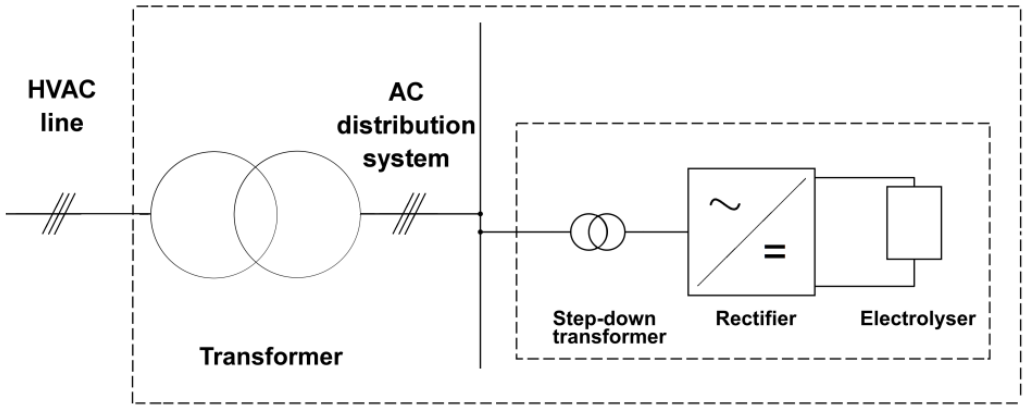

(a) AC distribution grid connected to HVAC grid through step-down transformers.

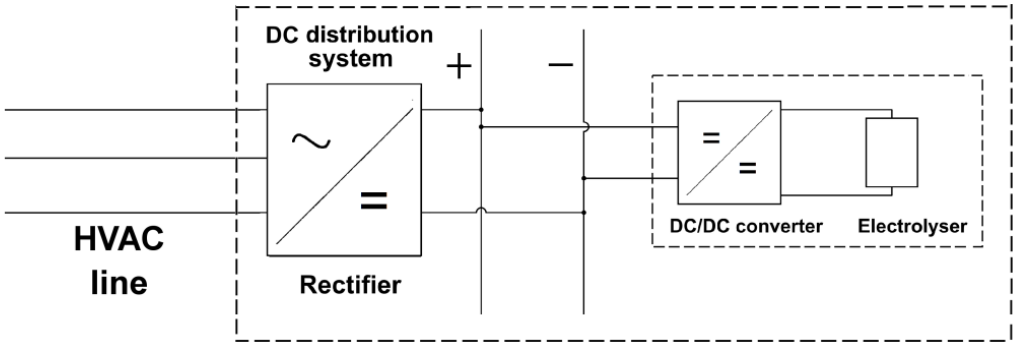

(b) DC distribution grid connected to HVAC grid through a large rectifier.

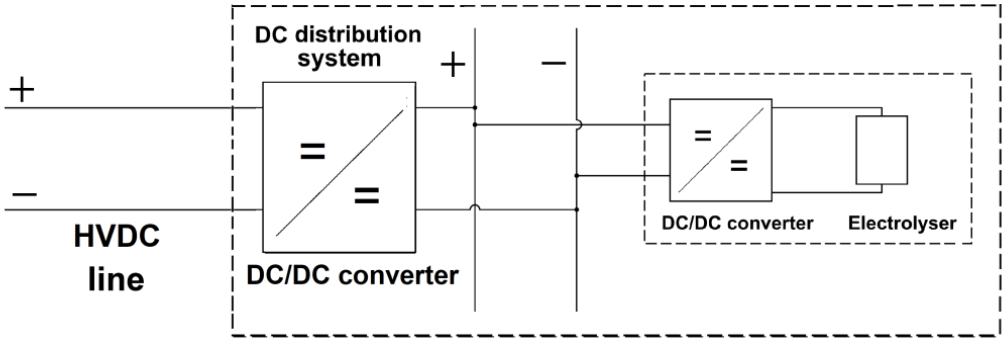

(c) DC distribution grid connected to HVDC grid through a large DC/DC converter.

Figure 6.1: Distribution grids for an electrolyzer station comprised of system modules [56].

The scope of the thesis was to analyze the technical feasibility of a GW-scale station connected to the traditional grid, therefore, the third distribution system has been disregarded. However, it may prove convenient to analyze in a future project since it unlocks the possibility to connect directly a renewable power plant to the substation skipping the intermediate AC/DC conversion infrastructure. The selection of 12-PTR as converter module for the electrolyzers leaves the AC distribution grid as the only option.

In Figure 6.2, it is presented an example of a SLD for a GW-scale electrolyzer station developed in *Electric infrastructure for electrolyser systems* thesis. This station is implemented in four different scenarios. All cases have a common structure of 3 voltage levels $400/150/V_{bus}$ kV with a Static Synchronous Compensator (STATCOM) connected to the PCC busbar, three 400/150 kV transformers and the electrolyzer systems connected to V_{bus} busbar.

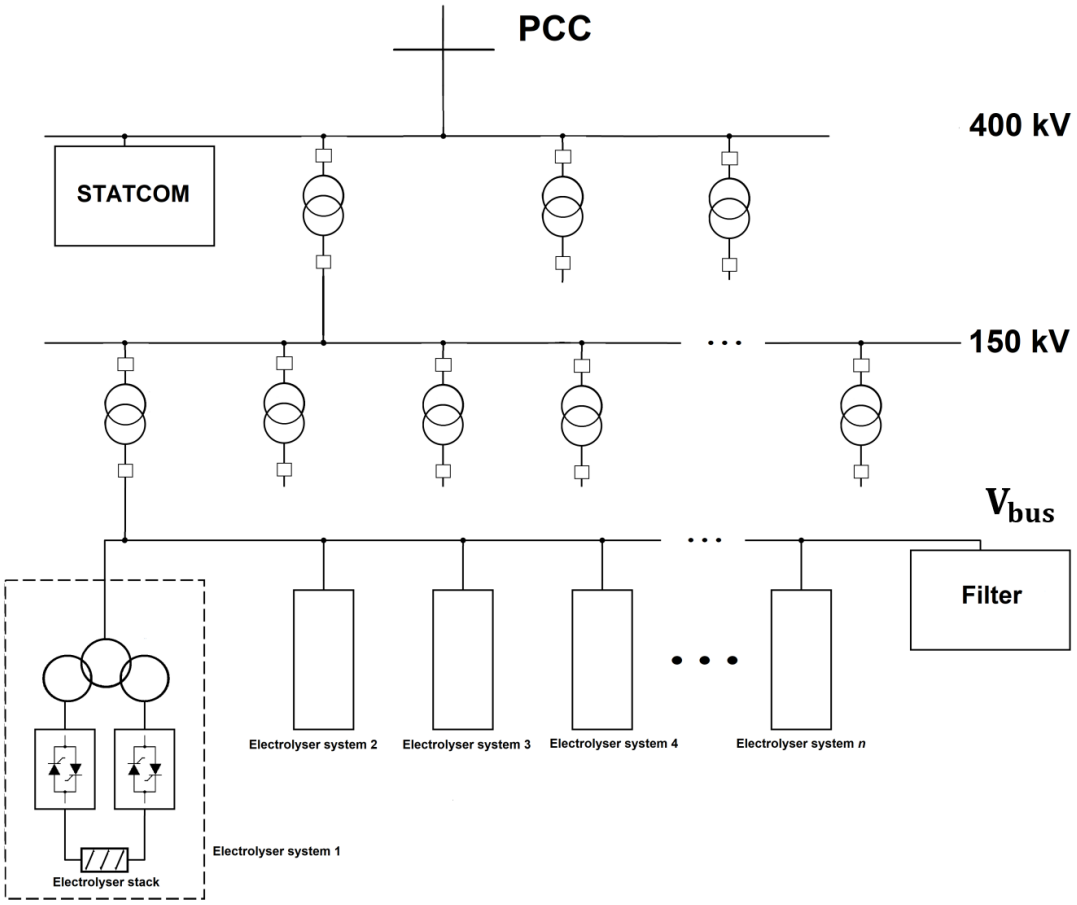

Figure 6.2: Electrolyzer station base line diagram [56].

The implementation of 66 kV or 33 kV at the electrolyzer system terminal, and the parallel connection or not of the 400kV/150KV transformers impacts the specifications of the station and the load shedding consequences in case of fault. The specification differences are summarized in Table 6.1.

Table 6.1: Structure comparison for cases 1-4 [56].

Parameter	Case 1	Case 2	Case 3	Case 4
V_{bus}	33 kV	66kV	33 kV	66kV
$I_{n,bus}$	3.0 kA	2.66 kA	3.0 kA	2.66 kA
I_{SCC}	27 kA	22 kA	21 kA	15 kA
$S_{n,T}$ (400/150 kV)	570 MVA	570 MVA	400 MVA	400 MVA
$S_{n,T}$ (150/V_{bus} kV)	172 MVA	300 MVA	172 MVA	300 MVA
N^o transformers	7	4	7	4

While case 1 and 2 have the 400/150 kV transformers connected in parallel, case 3 and 4 have them separated. The first approach is better in terms of redundancy and efficiency, since it avoids load shedding in case of failure of one transformer and sharing out the load between the transformers reduces the overall copper losses. However, this approach is not convenient in terms of protection. For example, a fault in the 150 kV busbar would interrupt the operation of the whole plant whereas in case 3 and 4 only a third

of the station would be offline. Separating the 400/150 kV transformers also reduces the short-circuit current at V_{bus} busbar in case 3 and 4 compared to their counterparts, since the impedance of one 400/150 kV transformer is higher than the equivalent for 3 parallel-connected transformers.

A relevant conclusion is to highlight the difference between using 33 or 66 kV as V_{bus}. Observing Table 6.1, the specifications of case 4 seem the most beneficial since it allows the lowest nominal bus current, short-circuit current and number of transformers. However, the application in industry of Medium Voltage (MV) Transformer Rectifiers led to the selection of 33kV as voltage level [72].

Case 3 could have been the selected design for the further analysis of the plant, but the Hydrohub project brought in the possibility of omitting the intermediate 150 kV busbar, linking directly the 400 kV and 33 kV busbars through 4 state-of-the-art three-winding transformers [69]. This approach is possible because there are no loads connected directly to the 150 kV busbar in the station SLD and it is technologically viable to manufacture these 400 kV/33kV transformers [72]. Besides, this scheme reduces the total number of transformers, busbars and switchgear systems necessary inside the station. The final structure design is illustrated in Figure 6.3.

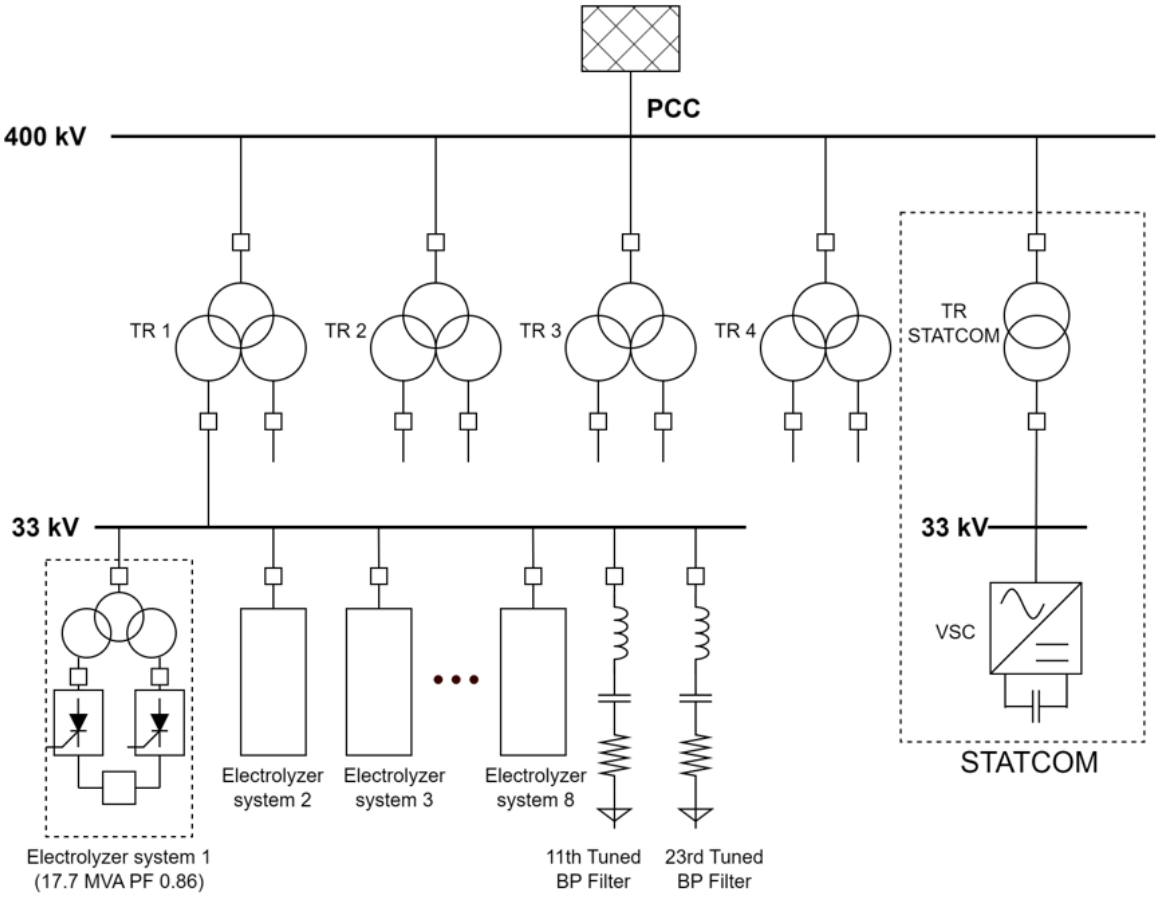

Figure 6.3: Selected SLD for station design.

6.2 Model implementation of different structure designs

The first step to implement the GW-scale structure design is to step-up the 1.9 MW electrolyzer system (A485-stack) to higher power ratings. As explained in section 4.2, Nel Hydrogen's catalogue [44] includes the modules A1000 and A3880, each using 2 and 8 A485-stacks respectively. Since A3880 enables a larger hydrogen production and power rating, this was the preferred choice.

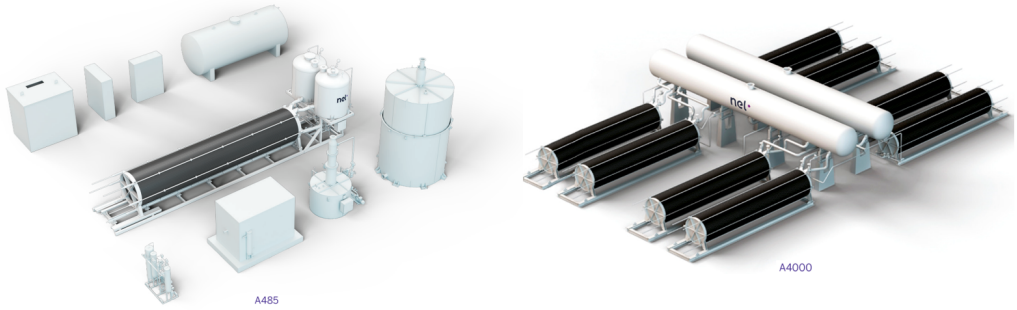

Figure 6.4: A485 and A3880 modules [44].

Since the connection settings are not defined in the specifications [44], it is possible to connect the stacks in 4 different schemes: all parallel (1s8p), 2-series in 4-parallel (2s4p), 4-series in 2-parallel (4s2p) and all series (8s1p). Some of these proposals would be impractical in real application, for example, problems like the self-discharge of parallel-connected batteries. Assuming all connection schemes are technically possible, the preferred choice for a 12-PTR would be the 4s2p module as shown in Figure 6.5.

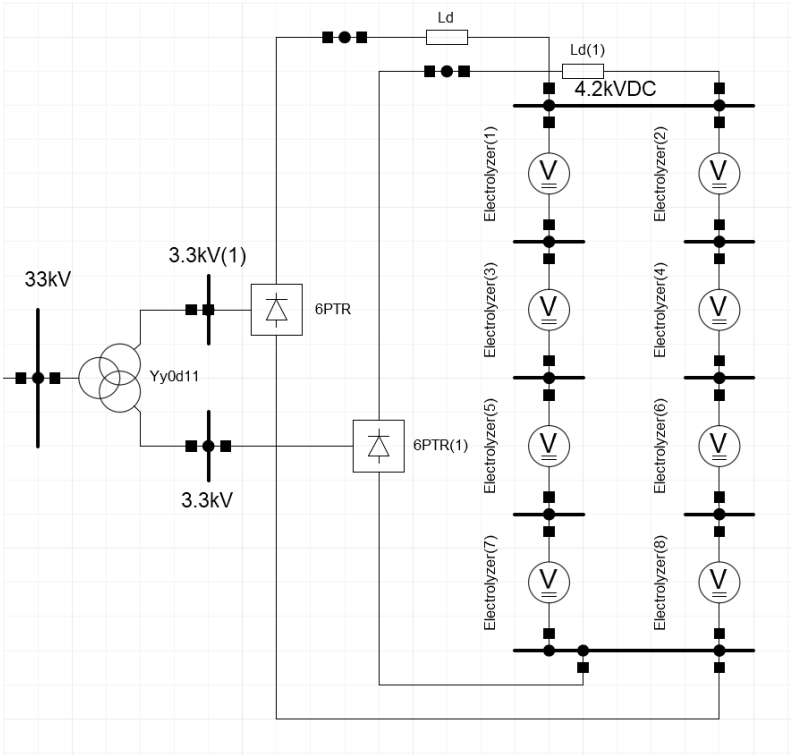

Figure 6.5: A3880 4s2p electrolyzer system.

This configuration provides a good performance since arranging 4 stacks in series in each leg allows to quadruple the DC voltage to 4.2 kV and 2 parallel legs to maintain the DC current to 2.1 kA per 6-pulse bridge. In other words, the current per thyristor reaches the maximum allowable of 2.1 kA and the blocking voltage per thyristor increases to 4.2kV, both values under the thyristor maximum ratings shown in Figure 5.1.

It is relevant to determine how many electrolyzer systems must be placed under each 33 kV busbar. The total number of electrolyzer systems in the one-GigaWatt plant is calculated dividing the total station active power capacity $P_{n,station}$ by the individual demand of each electrolyzer system $P_{n,sys}$. Assuming an A3880 module as individual load (15.2 MW at 80°C), equation (6.1) would dictate 66 electrolyzer systems. Since 64 systems are better distributed in multiples of 2, this was the implemented number in the substation.

$$N_{sys,total} = \frac{P_{n,station}}{P_{n,sys}} \tag{6.1}$$

The typical nominal current for a 33kV busbar is around 3 kA, which gives a maximum capacity per busbar of 172 MVA. Assuming a power factor of 0.86, each A3880 module consumes an apparent power $S_{n,sys}$ of 17.66 MVA at full load. Introducing this value in equation (6.2) gives a upper limit of 9 systems per branch and a subsequent minimum of 7 busbars for 33kV.

$$N_{sys,branch} = \frac{S_{n,branch}}{S_{n,sys}} \tag{6.2}$$

The proposed number of transformers between 400kV and 33kV (Figure 6.3) is 4 with a three-winding configuration, which gives a total of eight 33kV busbars. Following the same logic as distributing the systems in multiples of 2, the total number of systems per busbar is 8, which fulfills the minimum number of busbars.

Lastly, in order to reduce the simulated number of elements, the 8 electrolyzer systems connected to each busbar have been grouped into 2 equivalent modules of 70.6 MVA each with a power factor of 0.86 as shown in Figure 6.6.

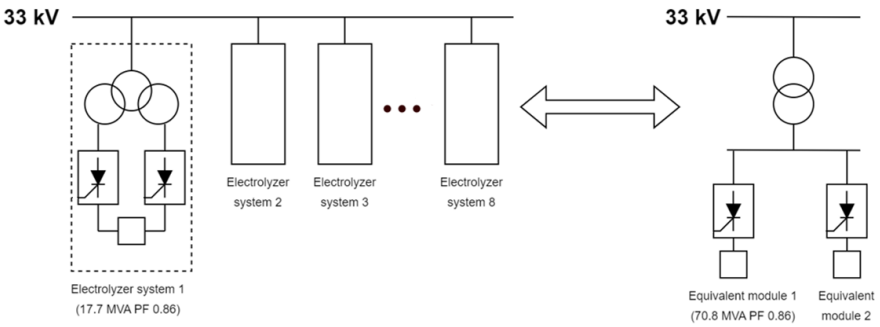

Figure 6.6: Grouping electrolyzer systems into electrolyzer modules.

6.3 Demand Connection Code

Grid code compliance is a critical aspect of connecting an industrial plant to the power grid at a high voltage level. Electrical codes and standards ensures the safety, reliability and interoperability of the connection.

In general, grid code requirements are not defined by a single entity, but by multiple applicable regulations and standards in each country. These may include national codes dictated by the transmission grid operator (Svenska kraftnät in Sweden), international standards (e.g. IEC), and local regulations for electrical installations and operations.

Three main documents are considered for grid code compliance in the plant's design and operation: the Demand Connection Code (DCC) [75], the IEEE Recommended Practice and Requirements for Harmonic Control in Electric Power Systems and the IEC assessment for waveform distortion limits.

Voltage regulation and power quality standards are the main aspects to consider when connecting an industrial facility to the power grid at HV level. These standards ensure a stable operation, prevent disruptions and mitigate adverse effects on the grid and connected equipment. These are summarized in 3 main categories: harmonics and distortion, power factor correction and voltage regulation.

6.3.1 Harmonics and Distortion

Compliance with harmonic standards is specifically relevant for the present study since the base load of the whole plant is a non-linear load that generates significant current distortions. This may cause electrical and mechanical stress in connected equipment, overheating and most importantly a distortion in the PCC voltage waveform, which can potentially affect other customers located nearby in the grid.

Since in DCC article 20 [75] it is not specified any harmonic limits, it is used the IEEE Standard 519-2014 [76] and IEC TR 61000-3-6:2008 Standard [77] as reference.

Table 6.2: Current distortion limits for systems rated above 161 kV IEEE Std 519-2014 [76].

	Individual harmonic order (odd harmonics) [%]					
I_{SC}/I_{max}	3≤h<11	11≤h<17	17≤h<23	23≤h<35	35≤h<50	TDD
<25	1.0	0.5	0.38	0.15	0.1	1.5
25<50	2.0	1.0	0.75	0.3	0.15	2.5
≥ 50	3.0	1.5	1.15	0.45	0.22	3.75

Table 6.3: Individual harmonic order (odd harmonics) IEC TR 61000-3-6 [77].

Harmonic order	Harmonic Voltage [%]	
h	MV	HV-EHV
5	5	2
7	4	2
11	3	1.5
13	2.5	1.5
$17 \leq h \leq 49$	$1.9\frac{17}{h} - 0.2$	$1.2\frac{17}{h}$

The Total Harmonic Distortion (THD) is a measurement that provides insight of a signal distortion. A low THD indicates a signal close to a pure sinusoidal wave. It is defined as the ratio of the RMS amplitude of the higher harmonic frequencies to the RMS amplitude of the fundamental frequency, as shown in equation (6.3).

$$THD_v[\%] = \frac{\sqrt{\sum_{n=2}^{\infty} V_n^2}}{V_1} * 100 \tag{6.3}$$

In Table 6.2, the Institute of Electrical and Electronics Engineers (IEEE) defines the current harmonic limits for users connected to transmission systems with a rated voltage at PCC greater than 161 kV. However, all tabulated values are expressed as a percentage of the maximum demand current, I_{max}, which transforms THD into Total Demand Distortion (TDD), calculated relative to the full load demand. This distinction is important because, at low currents, the harmonic components can be of similar magnitude to the fundamental. Both variables are correlated through equation (6.4), equal only at full load.

$$TDD_i[\%] = THD_i[\%] * \frac{I_1}{I_{max}} \tag{6.4}$$

In Table 6.3, the International Electrotechnical Commission (IEC) specifies voltage distortion limits based on voltage levels: medium voltage (MV) under 132 kV, and high voltage to extra high voltage (HV-EHV) above 132 kV. It is notable that the IEC imposes stricter limits for industries connected to HV-EHV busbars than for MV, due to the greater risk of jeopardizing the supply to a larger number of loads.

6.3.2 Power Factor Correction

Compliance with power factor standards is necessary to ensure an efficient use of electrical energy and avoid penalties imposed by utilities for poor power factor. Article 15 reactive power requirements of the DCC [75] limits the actual reactive power range at 0.9 power factor either for import or export of active power, except in situations where either technical or financial system benefits are demonstrated by the demand facility owner.

Nonetheless, this general guideline is a soft limit so in this thesis power factor is kept in unity at PCC. This statement implies that all reactive power produced or consumed inside of the plant should be compensated. This may be accomplished with passive components like capacitor banks or with active reactive-power compensators, such as Synchronous Condenser, Static Var Compensator (SVC) or Static Synchronous Compensator (STATCOM).

6.3.3 Voltage Regulation

High voltage industrial connections should include voltage regulation equipment to manage fluctuations and maintain a stable voltage supply within specified limits under extraordinary scenarios such as load rejection. The use of Dynamic Voltage Restorers (DVR), STATCOMs or similar devices are necessary to avoid or dampen voltage dips and temporary overvoltages.

6.4 Power Plant Electrical Components Design

6.4.1 Grid Characterization

For load flow calculations, the external grid is operated like a Slack Bus (SL) where the main setpoint is keeping the bus voltage at 1 p.u. Equation (6.5) and (6.6) define the grid's short-circuit capacity S_k'' as well as the short-circuit current I_k'', according to the settings defined in PowerFactory.

$$S_k'' = \sqrt{3} U_{nom} I_k'' \tag{6.5}$$

$$\bar{I}_k'' = \frac{c_{factor} U_{nom}}{\bar{Z}_1} \tag{6.6}$$

Rewriting both equations and assuming a R/X short-circuit ratio, the grid's positive sequence impedance $\bar{Z}_1$ can be derived. This impedance represents the Thevenin equivalent impedance of the external grid and is calculated dividing the nominal voltage U_{nom} of the grid by its short-circuit capacity S_k''. The c-factor coefficient is a safety factor at the user's disposal that is multiplied by U_{nom} to account for voltage variations at PCC. Splitting the impedance into their resistive and reactive components gives equation (6.7) and (6.8).

$$X_1 = \frac{c_{factor}}{\sqrt{1 + (\frac{R}{X})^2}} \frac{U_{nom}^2}{S_k''} \tag{6.7}$$

$$R_1 = \frac{R}{X} X_1 \tag{6.8}$$

As this section does not involve unbalanced load flow calculations or unbalanced faults, negative and zero sequence impedance calculations are beyond the scope of this study. Consequently, short-circuit current calculations for unbalanced faults are also excluded.

Table 6.4: Grid Characterization.

Parameter description	Parameter	Value	Units
Short-circuit power	S_k''	10000	MVA
Nominal voltage	U_{nom}	400	kV
c-factor coefficient	c_{factor}	1.1	-
Positive sequence R to X short-circuit ratio	R/X	0.1	-
Short-circuit current	I_k''	14.43	kA
Positive sequence resistance	R_1	1.75	Ω
Positive sequence reactance	X_1	17.51	Ω

6.4.2 Transformers Rating Estimation

As it is shown in Figure 6.3, there are 2 main voltage levels in the station (400 and 33 kV). Additionally, it is necessary to consider the 3.11 kV terminal inside the electrolyzer module to rate the equivalent 2-winding transformer. In a real-case substation, each A3880 module would have its own 3-winding transformer with 18 MVA of capacity given the nature of the 12-PTR topology, but a 2-winding is used to simplify calculations.

The maximum active power $P_{n,sys}$ demanded by a A3880 system is 15.2 MW with a power factor of 0.86, assuming operating temperature at 80°C. Since 4 AWE systems constitute an equivalent module, the $S_{n,module}$ becomes 70.8 MVA. There are 2 modules per busbar, therefore the power rating of the transformer between 3.11 kV and 33 kV terminals becomes 141.6 MVA according to (6.9).

$$S_{n,2TR} = N_{sys,branch} * S_{n,sys} \tag{6.9}$$

The total apparent power of the 400/33kV three-winding transformers $S_{n,3TR}$ doubles the 33/3.11kV transformer rating $S_{n,2TR}$, which gives an estimated capacity of 283.2 MVA. This may be assumed since both medium (MV) and low (LV) voltage windings are symmetric.

This is a simplistic method to estimate the transformer power rating disregards two important factors. The first one is the reactive power consumed by the leakage impedance, which increases the power rating of the transformer. Secondly, the electrolyzer module reactive power consumption is a quadratically proportional to the AC bus voltage as it was shown in Figure 5.19.

These two effects are accounted for in the load flow and ramp-up simulations in a latter section. These preliminary calculations serve only in the first instance, since additional components are connected in latter stages. These modify the load flow through the transformers, which makes these calculations only provisional. Both ratings and parameters are printed in Table 6.5.

Table 6.5: Transformers Rating Sheet.

Parameter	TR2	TR3	Units
Power Demand	141.6	283.2	MVA
Rated Power	150	300	MVA
HV side	33	400	kV
MV/LV side	3.11	33/33	kV
Positive sequence leakage impedance	3	14/14	%
Zero sequence leakage impedance	3	11/11	%
Vector Group	YNyn0	YNyn0yn0	-

6.4.3 Harmonic Analysis

The 12-PTR line current waveform exhibits a stepped square shape, which makes the whole electrolyzer system a non-linear load. It is important to eliminate these distortions before they get transmitted to the grid to avoid any effect on facilities nearby the station and unnecessary losses. In the absence of any filtering components, the current harmonic distortion at PCC and 33 kV busbar at maximum loading is depicted in Figure 6.7. The THD_i is 10.24%, way above the limit of 1.5% set by IEEE Std 519-2014.

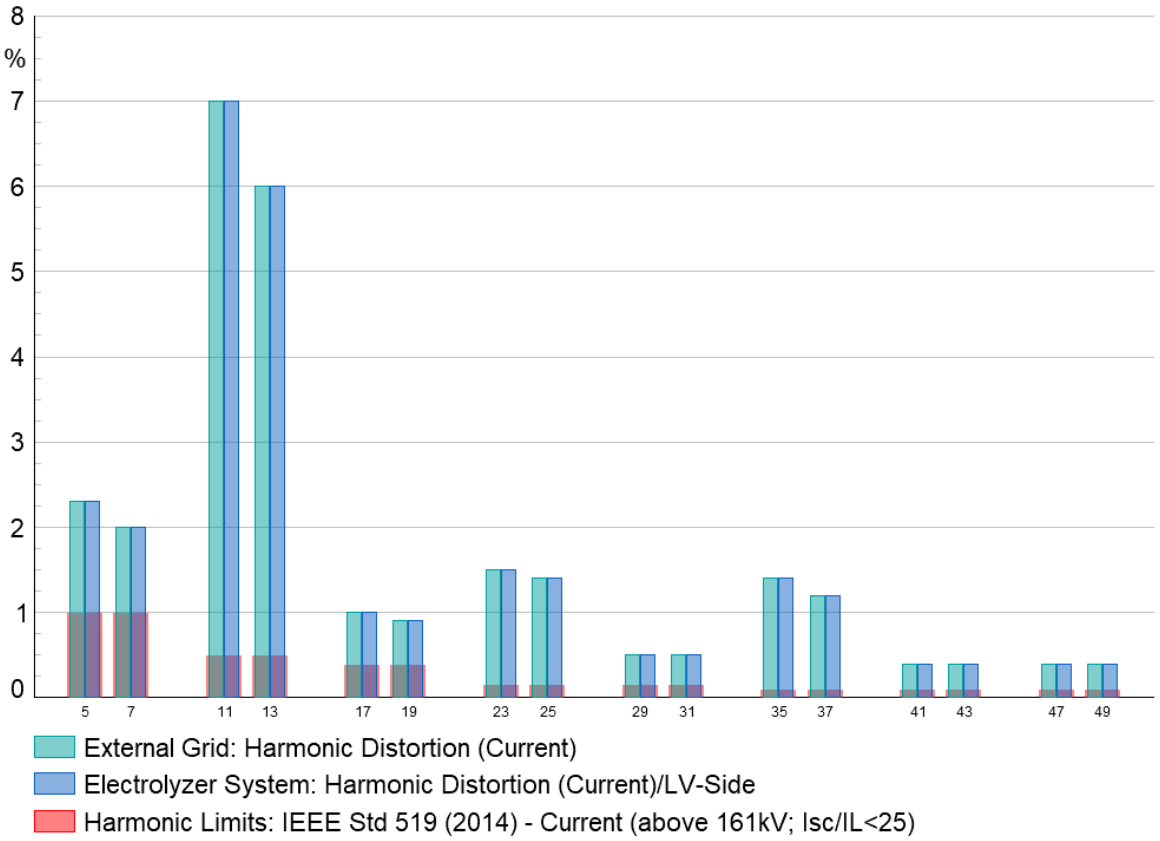

Figure 6.7: Current harmonic distortion distribution at 33kV and 400kV busbar without filtering.

Since the rectifier topology is thyristor-based, the resulting harmonic distortion is predominantly of low frequency. Various methods can be employed to mitigate harmonic distortions in electrical power systems, including the previously mentioned use of Phase-Shifting Transformers in Multi-Pulse Converters. However, two primary methods stand out as particularly effective, as illustrated in Figure 6.8.

- Active filtering. Through dynamic power converters such as DVRs and STATCOMs [78], the control scheme is designed to produce the measured harmonics in same magnitude but opposite phase. This way the harmonics get cancelled out seen from the power system side. This system is very effective, but requires high investment costs.

- Passive filtering. Using band-pass tuned filters for specific harmonic orders is a more economic and widespread solution. Designed to provide low impedance paths for harmonic currents, shunt filters divert harmonic currents away from the power

system. They are robust, but have the risk of overloading if an external distortion is injected from the grid, surpassing their rating.

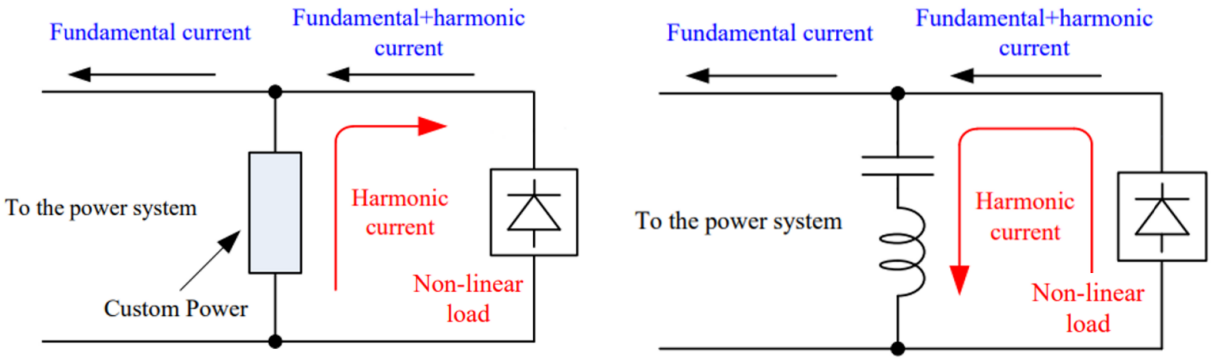

(a) Active Filtering.

(b) Passive Filtering.

Figure 6.8: Harmonic Filtering [79].

Given the advantages and disadvantages outline above, it was decided to proceed with passive filters. However, it would be beneficial to analyze the potential implementation of active filtering in a future project.

The working principle of a passive filter is illustrated in Figure 6.9. If the non-linear load is modeled as a current source I_h, the filter is designed to have zero impedance at the frequency of the target harmonic order. Therefore, the filter offers the path of least energy for the harmonic component of the current I_{fh}, as depicted in Figure 6.9b.

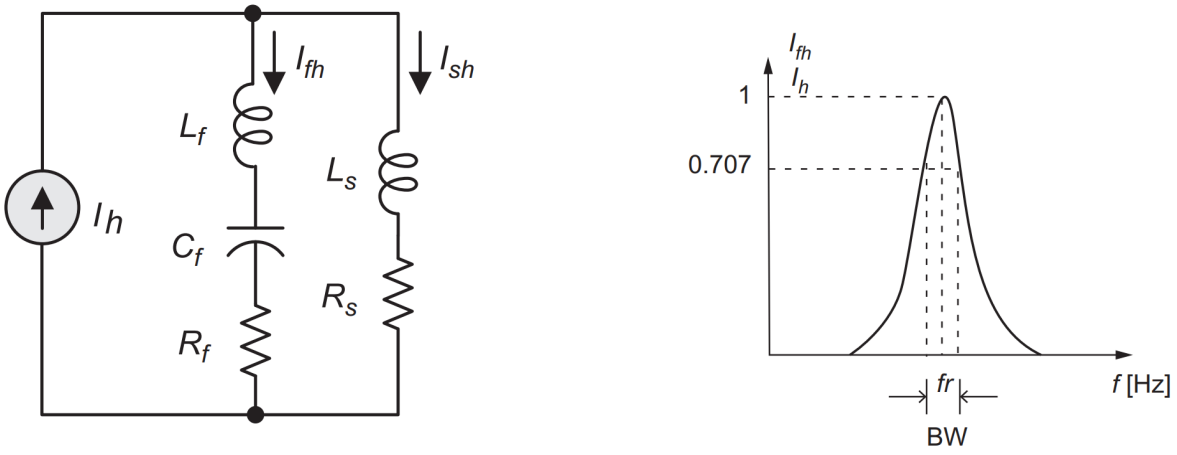

(a) Norton equivalent circuit of grid and filter.

(b) Frequency sweep of filter current.

Figure 6.9: Single-tuned filter [80].

To design a band-pass passive filter, it is required the definition of 4 main parameters: rated reactive power (Q_f), rated voltage (V_f), resonant frequency (f_r) and quality factor (q). With these four design parameters, the corresponding L_f, C_f, R_f values can be calculated using equations (6.10), (6.11) and (6.12).

$$X_f = X_L - X_C = \frac{{V_f}^2}{Q_f} \tag{6.10}$$

$$L_f C_f = \frac{1}{\omega_r^2} = \frac{1}{(2\pi f_r)^2} \tag{6.11}$$

$$q = \frac{\omega_r L_f}{R} = \frac{1}{\omega_r R_f C_f} \tag{6.12}$$

The selection of the inductance L_f and capacitance C_f is straightforward when implementing the corresponding resonance frequency f_r for the selected harmonic order and the desired reactive power Q_f. However, there is no specific rule to decide which quality factor q to implement, which in turn determines the filter resistance R_f. The quality factor significantly affects the steady-state losses and smooths the transition from capacitive to inductive impedance at the resonance frequency.

When studying the harmonic distribution of Figure 6.7, it can be observed that the most conflicting harmonics are the 11^{th}, 13^{th}, 23^{rd} and 25^{th}. In a first instance, it was considered to implement a band-pass filter tuned for each harmonic. Opportunely, it resulted to be enough with 2 band-pass filters, each tuned for the 11^{th} and 23^{rd} respectively.

There are two alternatives to connect the passive filters and mitigate the harmonics. The first option is to connect them to the 400kV busbar. It represents a cost-effective solution and requires a low footprint since it agglomerates all filtering equipment in a single bank. However, this option was quickly discarded since it allows the voltage distortion of each 33kV busbar, polluting the power supply of all converters connected to the terminal. Besides, the harmonics going through the transformers would cause unnecessary losses, but also strain on equipment and shortening of its life span [81].

The second option consisted on connecting filters to each 33 kV busbar, which avoids the intrinsic problem of the previous configuration, but increases the station footprint and cost. With this station design, the reactive power flow through the transformer is reduced considerably, which alleviates the voltage drop on its windings. The specifications for both filters is described in Table 6.6. If a frequency sweep is executed, it is obtained the filter impedance response shown in Figure 6.10.

Table 6.6: Specifications for 11^{th} and 23^{rd} tuned band-pass filters at 33kV busbar.

Design Parameter	Value	Parameter	Value
Rated Reactive Power	25 MVAr	R_f	0.2 Ω
Rated Voltage	33 kV	L_f	1.155 mH
Resonant Frequency	550 Hz	C_f	72.47 uF
Quality Factor	20		
Rated Reactive Power	25 MVAr	R_f	0.1 Ω
Rated Voltage	33 kV	L_f	0.26 mH
Resonant Frequency	1150 Hz	C_f	72.94 uF
Quality Factor	20		

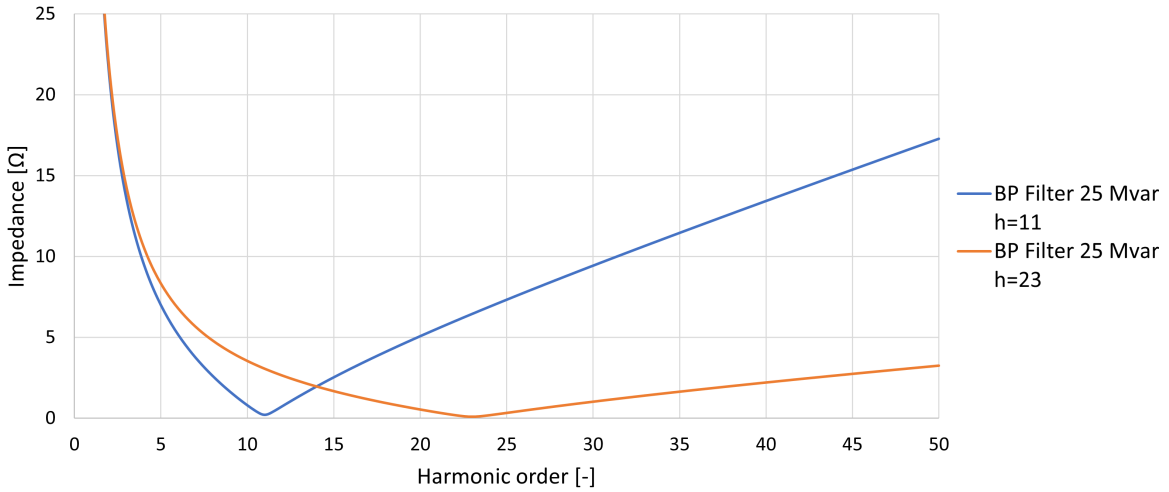

Figure 6.10: Frequency sweep of filter impedance.

As it can be observed Figure 6.11, the current distortion is handled so all components are maintained under limits and the TDD_c is 1.133% below the limit of 1.5 % stated by IEEE Std 519 (2014). Similarly, the harmonic distortion distribution of the voltage at PCC with the selected filtering is shown in Figure 6.12. Once more, it is checked that the magnitude for each harmonic order is below limits and the THD_v is 0.923% below the demanded 3% by IEC TR 61000-3-6 (2008).

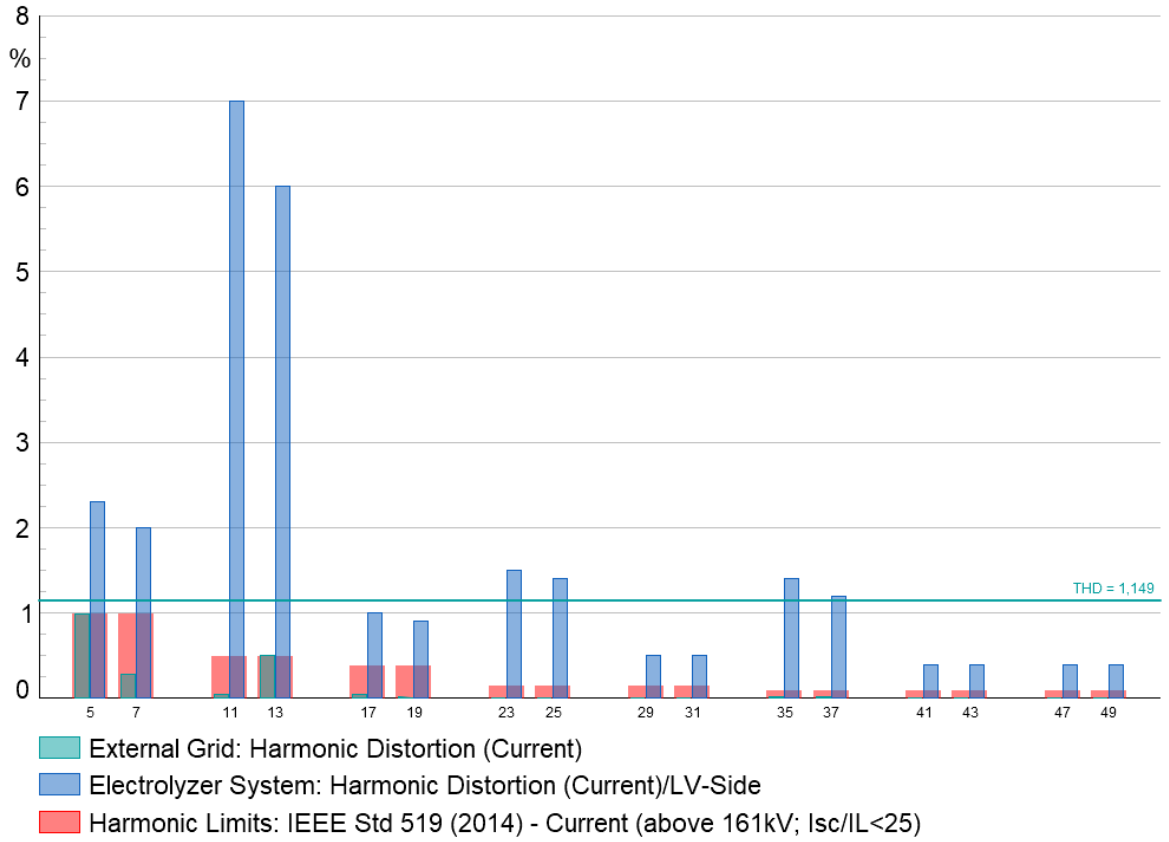

Figure 6.11: Current harmonic distortion distribution at 33kV and 400kV busbar with filtering.

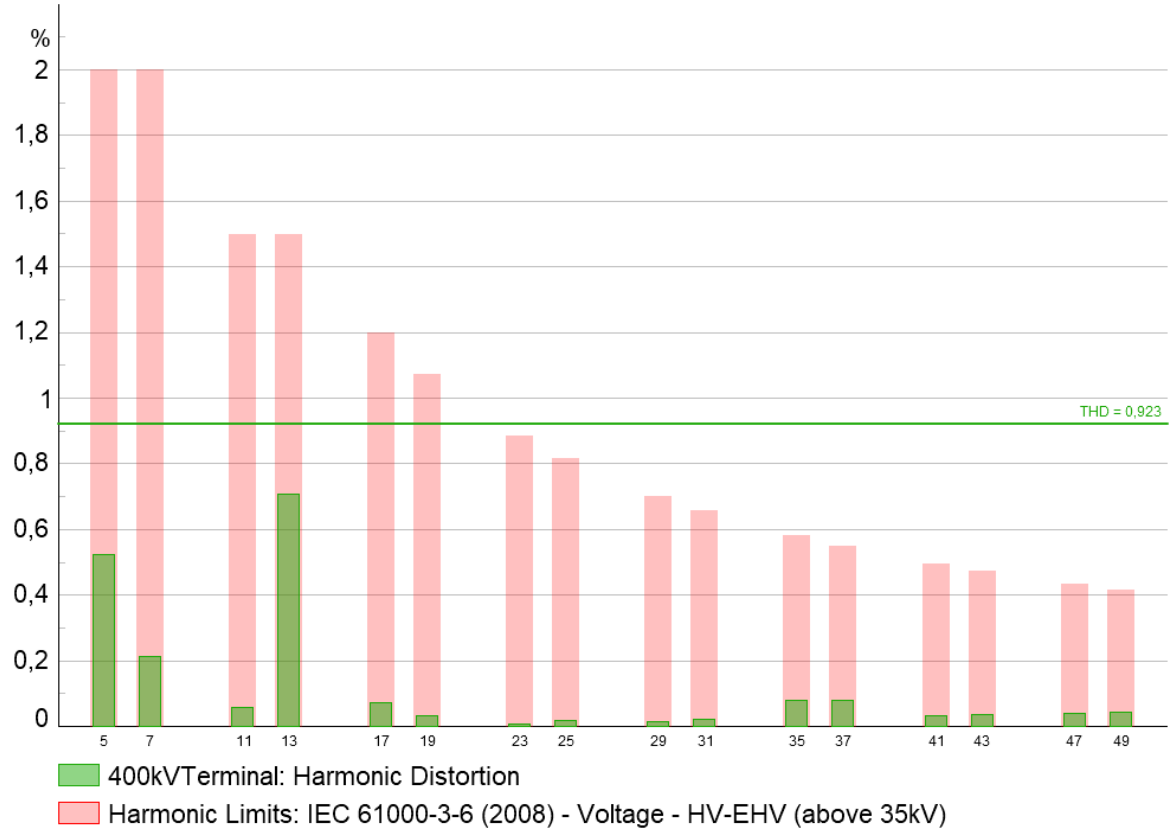

Figure 6.12: Voltage harmonic distortion distribution at PCC with filtering.

6.4.4 Reactive Power Compensation

As mentioned before, the passive filters at 33 kV busbar have an intrinsic positive effect: they produce reactive power, which partially compensates the electrolyzer systems reactive power demand. Therefore, it also decreases the voltage drop on the transformer and avoids the need of tap changers at the LV side by keeping the voltage within 0.95 and 1.05 p.u.

Nevertheless, an instantaneous reactive power compensation method would not be possible using only passive filters. Although capacitor banks are scalable and can operate in steps, these are fixed and present a complex operation for real-time power factor adjustments [82].

A possible alternative could be using another reactive power compensator (synchronous condenser, SVC) at the 33 kV busbar in parallel with the filters, which would solve the power factor adjustment. However, since there are already capacitor banks implemented at each 33 kV busbar, it would be more economical to increase their power rating instead of adding new equipment. Besides, filters present advantages against their competitors like low maintenance costs and low power losses [79].

Considering all theses facts, the proposed solution is a hybrid combination of these passive filters at 33kV and a STATCOM connected to the 400kV terminal imitating the solution proposed by J. Solanki, N. Fröhleke and J. Böcker [83] as illustrated in Figure 6.13.

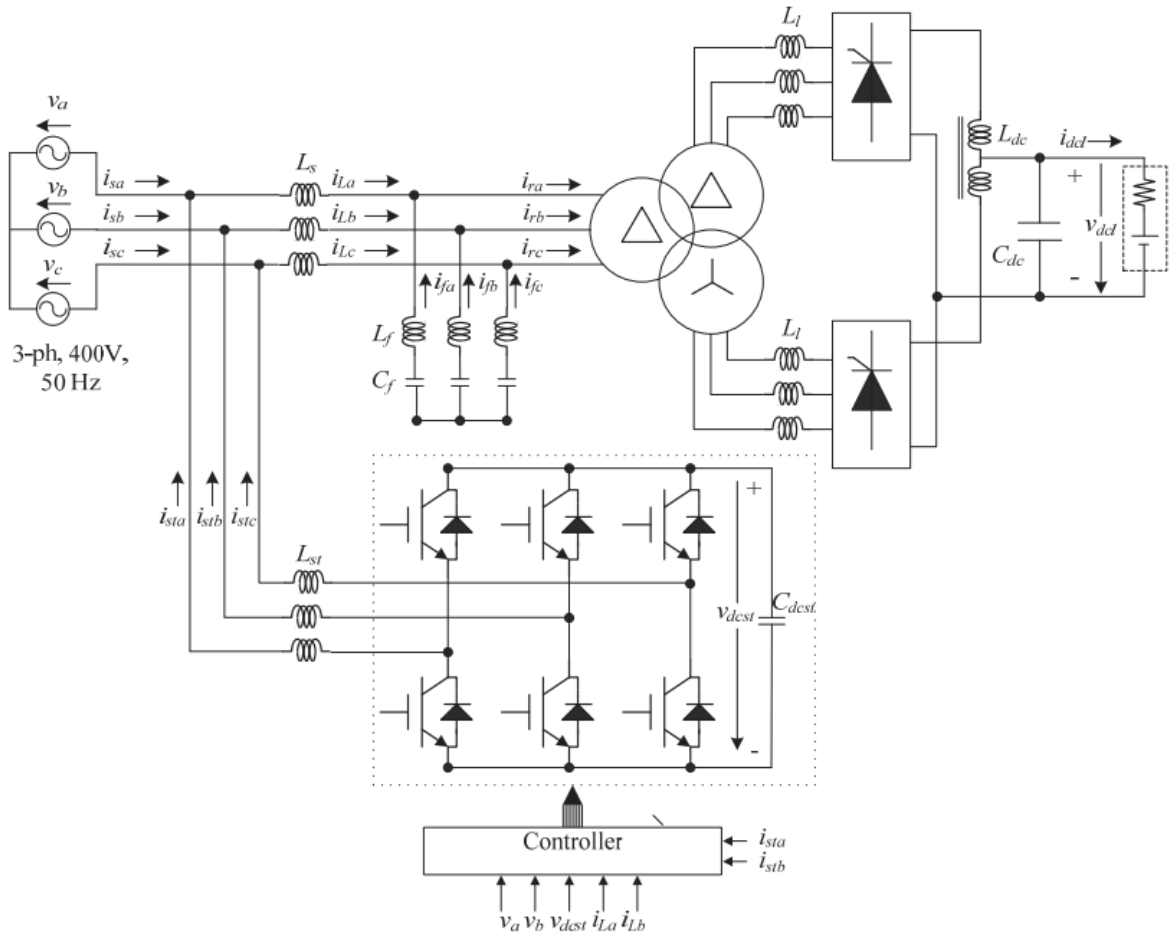

Figure 6.13: Hybrid system composed of STATCOM, passive filter, 12-PTR and electrolyzer [83].

The strategy of this system is to generate the bulk of reactive power demand with the passive filters, and use the STATCOM to provide the variable part. When the station is not demanding power, the injection of reactive power by the filters needs to be compensated by the STATCOM to avoid overvoltage. On the other hand, when the station is at full load, the STATCOM changes to capacitive mode, therefore merging the contribution of both devices.

The dilema is how to distribute the capacity between the two devices. According to J. Solanki *et al.* [83], the capital cost of a STATCOM is much higher than its equivalent capacitor bank of the same rating. This leads to an optimization problem of the rating of the STATCOM to minimize costs and increase the system performance. The proposed distribution of capacity between the STATCOM (Q_{st}) and filters (Q_{f}) suggested in [83] is as follows:

$$Q_f = \frac{Q_{max} + Q_{min}}{2} = N_{3TR}\frac{Q_{3TR,max} + Q_{3TR,min}}{2} \tag{6.13}$$

$$Q_{st} = \frac{Q_{max} - Q_{min}}{2} = N_{3TR}\frac{Q_{3TR,max} - Q_{3TR,min}}{2} \tag{6.14}$$

where Q_{max} and Q_{min} symbolize the maximum and minimum reactive power demanded

by the station. In this case, the maximum and minimum scenarios will correspond to the station working at 100% and 20% loading respectively. Assuming no filters or STATCOM present in the SLD, the station load flow is presented in Figure 6.14 according to the calculations made in section 6.4.2.

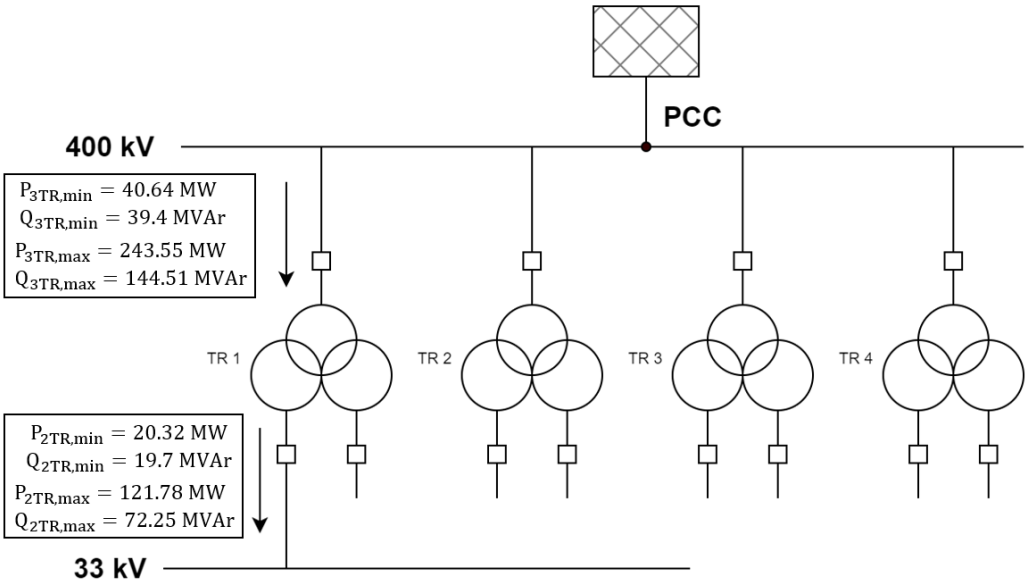

Figure 6.14: Preliminary load flow calculation.

Substituting the reactive power flows of Figure 6.14 on equation (6.13) and (6.14) gives 367.83 MVAr and 210.23 MVAr respectively, being Q_{f} the total capacity of all passive filters in the station. To obtain the individual power rating of each filter it is necessary to divide Q_{f} by the number of 33kV busbars, resulting in 46 MVAr, which evenly distributed between the 11^{th} and 23^{rd} tuned filters gives a power rating of 23 MVAr each, below the filter rating calculated in section 6.4.3. In Table 6.7, the STATCOM and filters specifications are presented with Q_{st} recalculated for the new Q_{f}:

Table 6.7: Preliminary specifications for STATCOM and filters.

	STATCOM	11^{th} filter	23^{rd} filter
Rated power	250 MVAr	25 MVAr	25 MVAr
Line-line voltage	33 kV	33 kV	33 kV
Continuous voltage limit	1.1 / 0.9 p.u.	1.1 / 0.9 p.u.	1.1 / 0.9 p.u.

This configuration stands out for its dynamic advantages and being a more cost-effective solution. While the STATCOM's main purpose is to regulate the reactive power compensation, it can be used to fulfill other grid code regulations for the station. In section 6.3, it was stated 3 regulations that the station must comply to be able to connect to the grid. Harmonics and power factor correction have already been addressed, so only voltage regulation equipment remains up for discussion.

6.4.5 STATCOM Design

The simplest way to simultaneously achieve voltage regulation and power factor correction is by implementing a control strategy in the STATCOM, which allows for short-term voltage control at PCC and long-term compensation of reactive power. In some ways, this behavior resembles that of a synchronous machine [84]. This control strategy is implemented in PowerFactory by introducing an External Station Controller set up to have null reactive power flow exchange with the grid in load flow analysis, and a DC & AC voltage control block diagram for dynamic operation during RMS simulation.

The most suitable configuration for the station's STATCOM is a multilevel converter (MMC) with cascaded H-bridge valves [72], based on the current and voltage ratings depicted in Table 6.7. However, since the purpose of this model is only to demonstrate the behavior of the STATCOM, the Voltage Source Converter (VSC) is modeled as a two-level VSC with PWM using Grid Following control.

In Figure 6.15, it is illustrated the STATCOM system SLD and composite frame control schematic diagram. It receives three main inputs, DC-link voltage measurement V_{dc}, PCC AC voltage measurement V_{ac} and the current at VSC terminal i_{ac}. The voltage control block calculates the reference current i_{ref} in dq coordinates required to obtain a reference voltage of 1 p.u. at PCC. For the synchronization of the STATCOM, a Phase-locked Loop (PLL) estimates the PCC phase angle θ. Both variables, i_{ref} and θ, introduced inside the PowerFactory Converter Block (.ElmVsc) gives the VSC switching pattern.

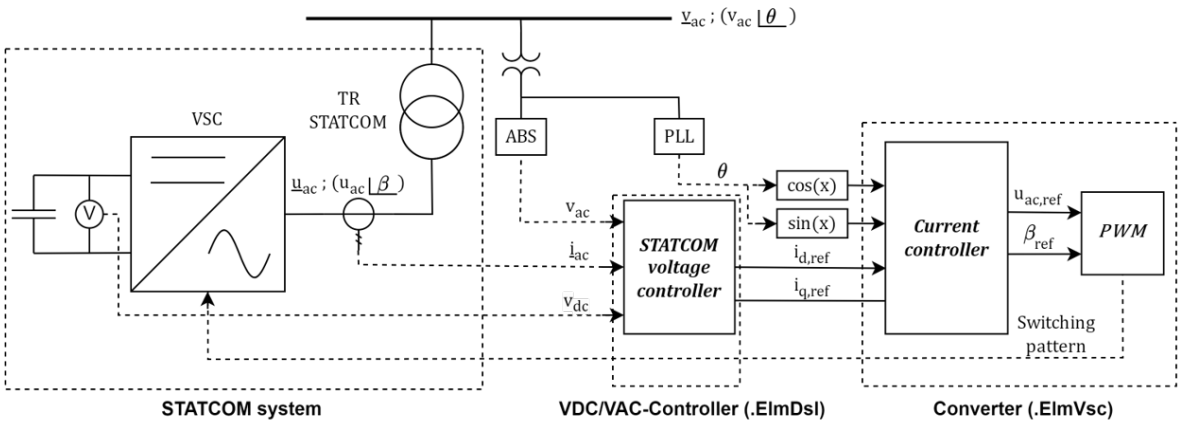

Figure 6.15: STATCOM Single Line Diagram and Composite Frame.

The purpose of implementing Grid Following (GFL) instead of Grid Forming (GFM) is due to its straightforward implementation, simplicity in control design, and suitability for stable grids with well-defined voltage profiles [85]. However, GFL converters may encounter instability issues in weak grids and do not respond effectively to deviations in grid frequency. Due to these problems, it is of interest to implement a GFM control structure in a future project, particularly where the external grid connected to the PCC presents low a short-circuit capacity and low inertia due to a high concentration of renewables.

Figure 6.16 presents the STATCOM voltage control diagram, divided into DC and AC voltage control, each with a PI controller for the respective voltage error. The STATCOM

reference frame is synchronized with the grid via the PLL, allowing direct control of active power exchange with the grid through the d component of the current i_d. Similarly, reactive power is controlled through the q component of the current i_q. Since active power is directly related to the discharge of the DC capacitors, there is a relationship between the DC voltage error ΔV_{dc} and i_d. The same logic applies to the AC voltage and the reactive power, linking the AC voltage error ΔV_{ac} and i_q. All variables shown in the control block diagram are expressed in per unit, and the control parameters are listed in Table 6.8.

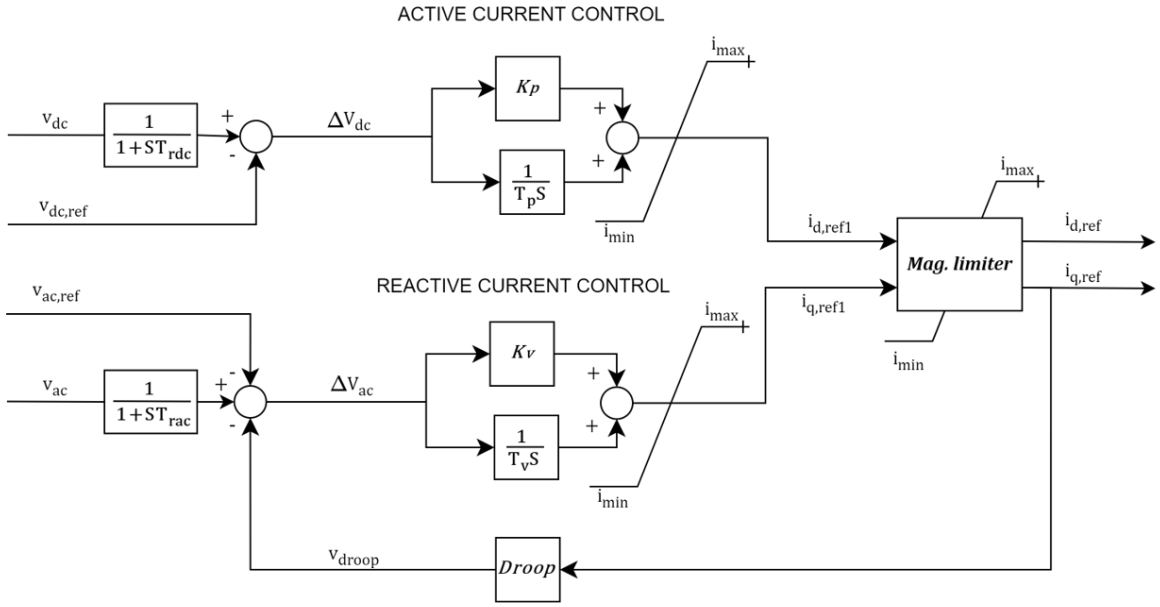

Figure 6.16: STATCOM Voltage Control Block Diagram.

Table 6.8: STATCOM controller parameter definition.

Parameter description	Parameter	Value
Active Power Control Gain	$K_{P,st}$	10
Active Power Control Time Constant	$T_{P,st}$	0.002 s
Voltage Control Gain	$K_{v,st}$	4
Voltage Control Time Constant	$T_{v,st}$	0.002 s
Droop	$Droop$	0
DC Voltage Control Time Delay	$T_{r,dc}$	0.001 s
AC Voltage Control Time Delay	$T_{r,ac}$	0.01 s
Maximum current	i_{max}	1 p.u.
Minimum current	i_{min}	-1 p.u.

Table 6.9: PLL parameter definition.

Parameter description	Value
Proportional Gain	5
Integration Gain	1
Upper frequency limit	1.2 p.u.
Lower frequency limit	0.8 p.u.

7

Simulation cases

In order to verify the station design and the electrical components ratings described in section 6.4, it is necessary to carry out several simulations, including both steady-state and dynamic operation of the plant.

There is a key difference to consider between steady-state and dynamic operation. In load flow analysis the external gird is modeled as a Slack Bus, an ideal voltage source of magnitude 1 p.u., whereas in dynamic simulation, it considers the Thevenin equivalent model of the external grid.

1. Load flow analysis
2. Ramp-up simulation
3. Load Rejection

In load flow calculation, results are presented for two different scenarios: "Service Off" and "Service On". While the first scenario keeps the station working without any reactive power compensation devices, the second scenario includes both STATCOM and filters in operation. This separation allows for a comparative analysis of both performances and ensures that the station systems were correctly rated during the design phase. Ramp-up simulation and load rejection are executed only for "Service On" scenario due to non-grid code compliance in "Service Off" scenario.

7.1 Load flow analysis

In this section, load flow is calculated for the station working at three different loading rates: 20%, 50% and 100%. To apply these ratings, all electrolyzers are uniformly configured with a specific capacity, thus the notation "20% Loading Service Off" implies that each electrolyzer within the facility is functioning at 20% of its hydrogen production capacity, with the STATCOM and filters deactivated. Same logic applies for the rest.

In Table 7.1, external grid load flow results are displayed. The first observation is the correct performance of the STATCOM and filters, which are capable of compensating the reactive power throughout the full loading of the plant in steady state. Meanwhile in "Service Off" scenario, power factor values are identical to those described for A485 stack, which correlates with the fact that the station is a scale-up of that individual stack. Small differences of active power between both scenarios is caused by the filters losses.

Table 7.1: External Grid load flow with 400 kV nominal voltage.

Case	Active Power MW	Reactive Power MVAr	Apparent Power MVA	Power Factor
20% Loading Service Off	162.0	157.3	225.8	0.717
50% Loading Service Off	442.6	350.4	564.5	0.784
100% Loading Service Off	972.1	574.0	1129.0	0.861
20% Loading Service On	163.2	0.0	163.2	1.000
50% Loading Service On	443.7	0.0	443.7	1.000
100% Loading Service On	973.2	0.0	973.2	1.000

In Table 7.2, load flow results for the three-winding transformers are shown. An important observation is that load flow analysis in "Service Off" scenario agrees with the theoretical calculations made in Sections 6.4.2 and 6.4.4.

Another noticeable finding from these results is the reversal of reactive power flow in the transformer for the "20% Loading Service On" case, where the introduction of filters at 33 kV busbars creates an injection of reactive power greater than the one demanded by the electrolyzers. This causes a net increase of apparent power flow from 18.8% to 24.9% at 20% loading, but with the desired benefit of reducing the maximum apparent power flow from 94.1% to 85% at 100% loading.

Table 7.2: Three-winding transformers load flow results at 400 kV terminal.

Case	Max. Loading %	Tot. Active Power HV-Side [MW]	Tot. Reactive Power HV-Side [MVAr]
20% Loading Service Off	18.8	40.5	39.3
50% Loading Service Off	47.0	110.6	87.6
100% Loading Service Off	94.1	243.0	143.5
20% Loading Service On	24.9	40.8	-62.4
50% Loading Service On	37.0	110.9	-3.0
100% Loading Service On	85.0	243.3	76.5

In Table 7.3 one can notice the proportional relation between filters' reactive power and 33kV terminal voltage, due to the shunt impedance connection. The load flow is identical for both 25 MVAr BP filters. The net difference of reactive power between electrolyzer system consumption and filter generation becomes capacitive below 50% loading, boosting the voltage at 33 kV, and inductive above 50%, droping the voltage. These results prove correct the optimization method principle described in section 6.4.4.

Table 7.3: 11^{th} and 23^{rd} harmonic filters.

Case	Reactive Power MVAr	u, Magnitude p.u.
20% Loading Service On	-27.4	1.047
50% Loading Service On	-25.3	1.006
100% Loading Service On	-23.0	0.960

Finally, STATCOM load flow results are displayed in Table 7.4. The most noticeable observation is the overloading of the STATCOM system, which demands a rating increase to at least 350 MVAr. This underestimation is mainly caused by two factors: the increase of electrolyzer reactive power consumption due to voltage boosting of the AC terminal and the dependence of capacitor banks reactive power injection with the 33kV busbar operating voltage, both factors not accounted for in the theoretical calculations. Lastly, it is seen how the STATCOM capacitive and inductive mode of operation determines the STATCOM LV bus voltage, decreasing it at 20% loading when working as a reactor and increasing it at 100% loading as a capacitor.

Table 7.4: STATCOM reactive power flow and 33kV busbar voltage.

Case	Reactive Power LV-Side [MVAr]	Reactive Power HV-Side [MVAr]	u, Magnitude LV-Side [p.u.]
20% Loading Service On	231.9	249.7	0.929
50% Loading Service On	10.7	10.7	0.997
100% Loading Service On	-332.7	-305.9	1.087

7.2 Ramp-up simulation

In this section, the aim is to study the dynamic operation of the plant, in particular the power consumption ramp-up sequence from 20% till full load; how the station systems interact with each other, following the strategy discussed in Section 6.4.4; and how the loading variation in one side of the station affects the rest of components.

Since the thermal model of the electrolyzers is out of the thesis scope, the simulation starts with all devices already operating at 80°C. The real start sequence of the plant would have a preheating stage with the electrolyzers operating at a loading greater than 15% until reaching the desired operating temperature. This criteria is applied by starting the ramp-up with the station operating in steady state, all electrolyzer systems at 80°C and a station total loading of 20%.

An important feature of the start sequence is the operation of the STATCOM and the capacitor banks. It is assumed that the station never operates in a no load scenario: the electrolyzers with no loading and the capacitors banks connected. The capacitor banks circuit breakers close only when all electrolyzer modules under a 33 kV busbar reach 20% loading. Until that moment, the STATCOM takes all responsibility for reactive power compensation. This procedure avoids an unnecessary over-sizing of the STATCOM, since in no load scenario, the non compensation of the capacitor bank reactive power injection by the electrolyzers boosts the 33kV voltage to 1.1 p.u.

The station ramp-up sequence starts at 50 seconds and is done in steps of 50% loading for each electrolyzer system module under each 33kV busbar every 40 seconds, while this is alternated with the adjacent module every 20 seconds. This sequence details are described in Table 7.5.

Table 7.5: Ramp-up sequence.

Station loading	Loading step	Time	Electrolyzer module number
27.5%	50% Loading	at 50s	0, 4, 8, 12
35%	50% Loading	at 60s	2, 6, 10, 14
42.5%	50% Loading	at 70s	1, 5, 9, 13
50%	50% Loading	at 80s	3, 7, 11, 15
62.5%	100% Loading	at 90s	0, 4, 8, 12
75%	100% Loading	at 100s	2, 6, 10, 14
87.5%	100% Loading	at 110s	1, 5, 9, 13
100%	100% Loading	at 120s	3, 7, 11, 15

The major difference with the load flow analysis is the exchange of reactive power with the grid as illustrated in Figure 7.1. While the active power remains identical to the load flow, reaching 163.5 MW at 20%, 442.5 MW at 50% and 973.5 MW at 100% loading, the reactive power presents a progressive ramp-up curve as well. Instead of a complete cancellation, it reaches a maximum of -137.4 MVAr and a steady state of -56.4 MVAr at 100% loading.

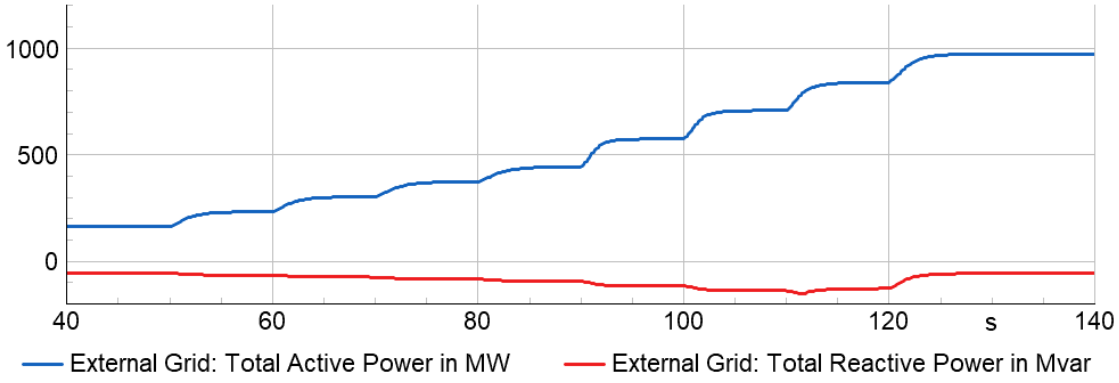

Figure 7.1: Ramp-up power flow in the External Grid.

This behavior is attributed to the STATCOM short-term voltage control, which becomes evident looking at the voltage graph in Figure 7.2.

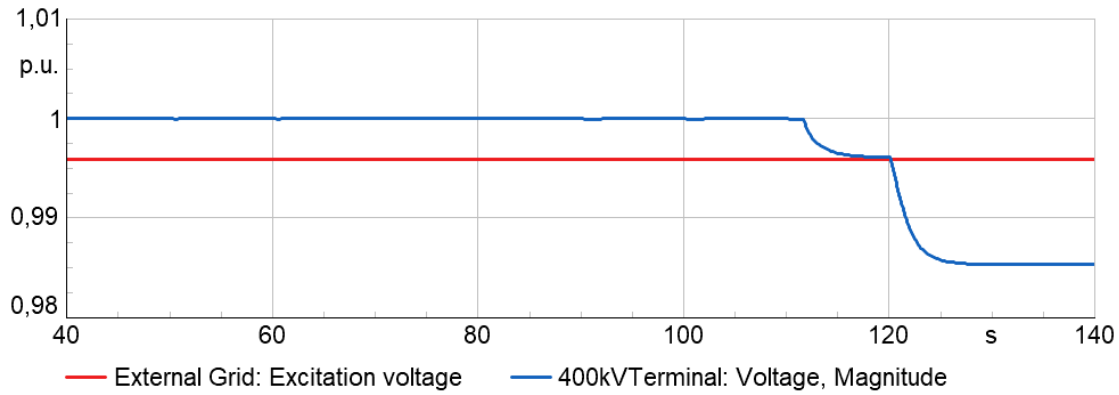

Figure 7.2: Ramp-up External Grid excitation voltage and PCC voltage.

As mentioned before, since this dynamic simulation considers the grid's equivalent Thevenin impedance, the STATCOM's role to maintain the terminal voltage at 1 p.u. prompts it to inject additional reactive power and compensate for the voltage drop.

Nevertheless, as shown in Figure 7.3 the STATCOM reaches the current limit at 110 seconds in the 87.5% loading step. The control action effectively maintains the 400 kV busbar at 1 p.u. until this point, but drops to a voltage level of 0.985 p.u., which is still under valid limits [86]. During the steady state, this gets compensated by the grid increasing its excitation voltage from 0.995 to 1.015 p.u., as observed in the next section.

The STATCOM's SVC has a power rating of 350 MVAr at nominal voltage. However, the maximum deliverable reactive power comes determined by the SVC AC voltage limits, from 0.9 to 1.1 p.u., and the maximum current rating I_{max}, in this case 6.123 kA. According to equation (7.1), this gives an SVC power limit of 315 MVAr in inductive mode and 385 MVAr in capacitive mode, which agrees with the maximum reactive power reached at the end of the ramp-up, 383 MVAr, illustrated in Figure 7.3.

$$Q_{st} = \sqrt{3} V_{LL} c_{factor} I_{max} \tag{7.1}$$

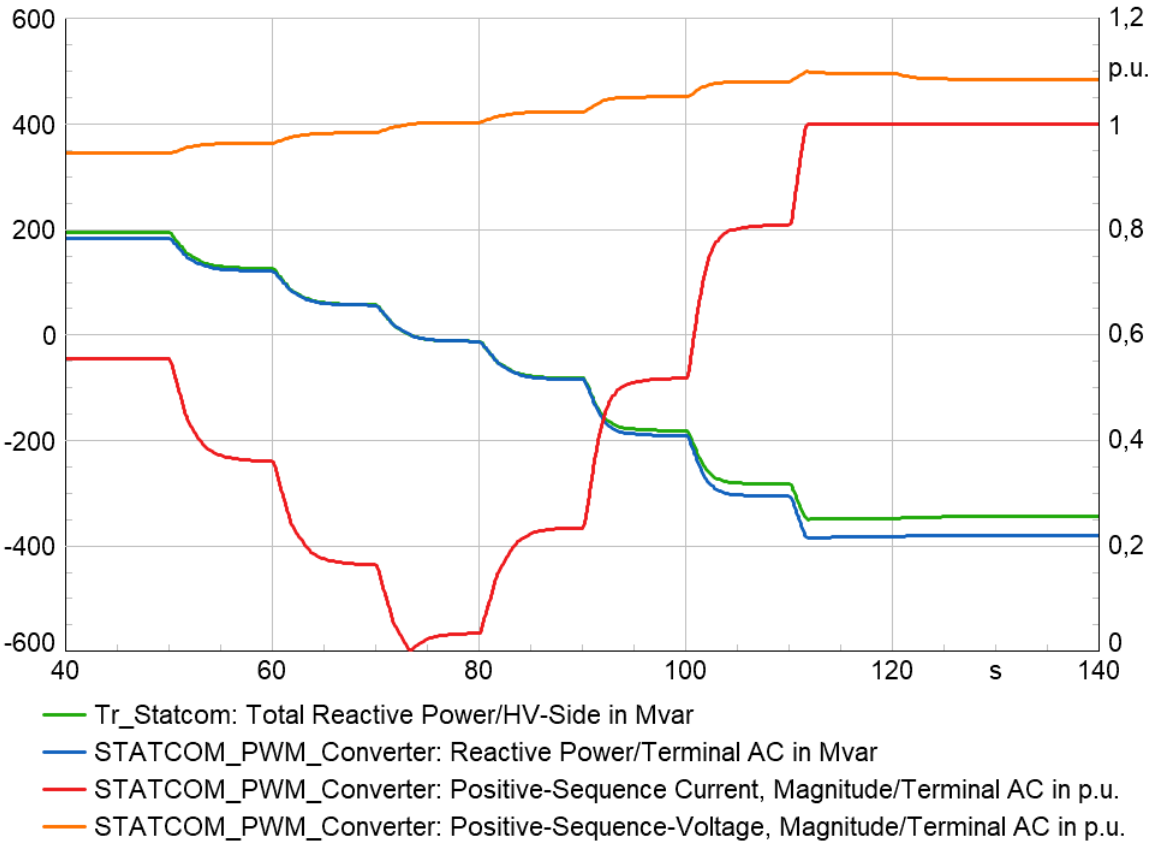

Figure 7.3: Ramp-up STATCOM load flow, current and voltage in p.u.

In Figure 7.4, it is clearly reflected the incorporation of passive filters at the 33 kV busbars. Same as in load flow analysis, the 400/33kV three-winding transformers present a negative reactive power flow until the 50% loading step at 80 seconds, where it exhibits a null net

exchange, and a positive reactive power flow until 100% loading. Comprehensively, the active power flow remains consistent with the load flow "Service Off" scenario.

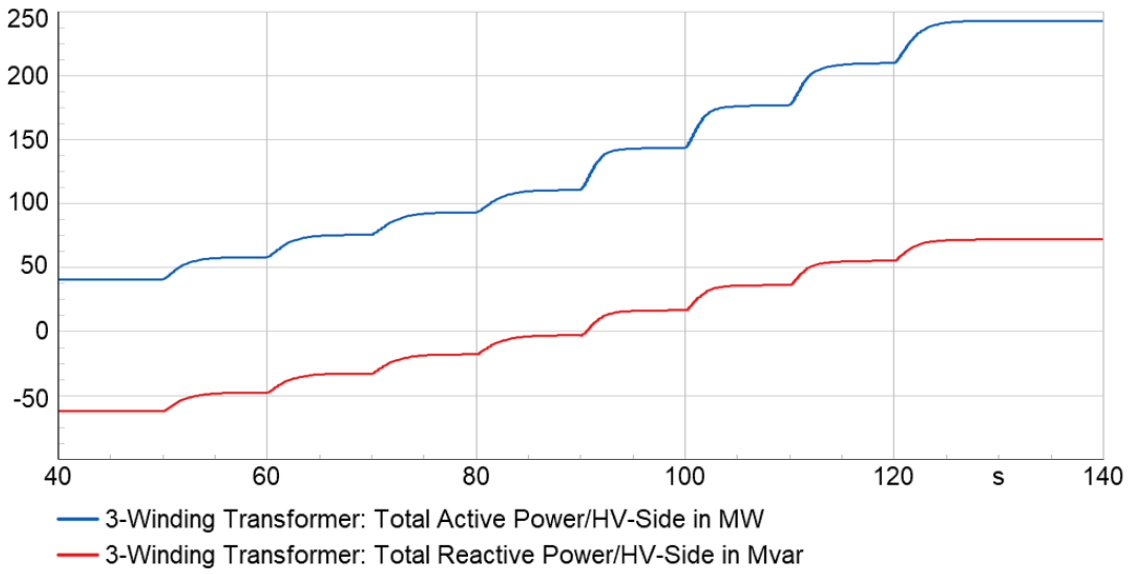

Figure 7.4: Ramp-up power flow in a three-winding 400/33kV transformer.

While Figure 7.4 presents the total power flow at the HV side of the three-winding transformers, Figure 7.5 shows the load flow for the equivalent load under each 33 kV busbar. The first observation is that the voltage at one 33kV busbar has 8 drops although the load only increases 4 times through it. This behavior is caused by the three-winding nature of the transformer, which makes the voltage of both MV windings mutually dependent.

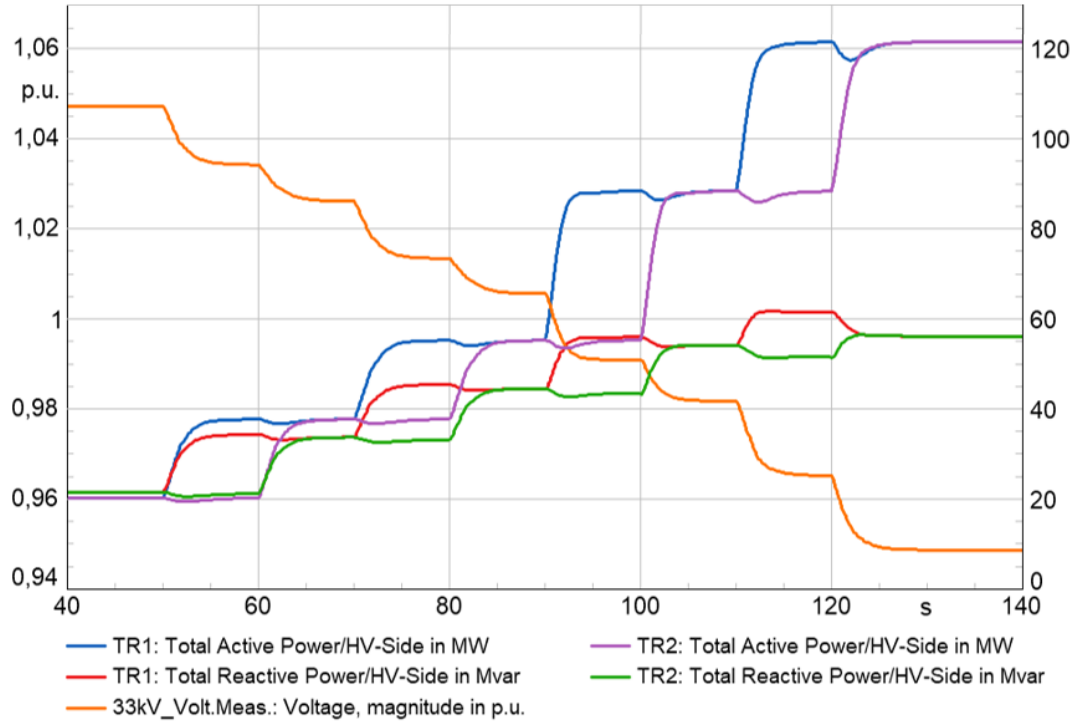

Figure 7.5: Ramp-up power flow in adjacent electrolyzer modules and voltage at 33 kV busbar.

The main consequence of this phenomenon is that after completing one loading step in one of the MV windings, the reactive power follows a small decrease due to the reasons explained in Section 5.4.4. Contrarily, the active power remains constant despite the voltage decrease, except for a transient-bump where the electrolyzer controller adjusts the firing angle accordingly. This behavior is proven in Figure 7.6.

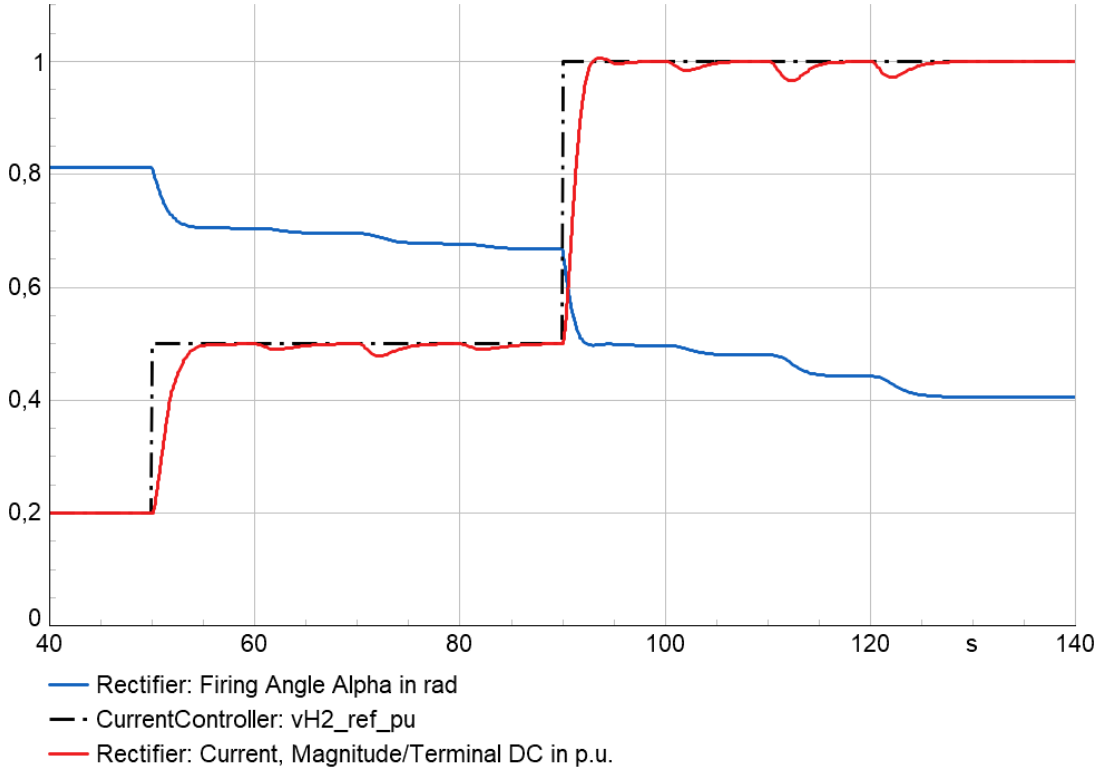

Figure 7.6: Ramp-up electrolyzer dynamic response.

7.3 Load Rejection

Load rejection in electric power systems is a dynamic event where a significant portion of the electrical load is suddenly disconnected from the power grid. This situation can be triggered for several reasons, such as faults in the distribution network, tripping of circuit breakers and, the present case of study, sudden disconnection of large industrial loads.

Load rejection causes notable repercussions for both the grid and the station. From the grid side, there is a great drop of active power consumption, which has important effects in the frequency, whose magnitude is dependent on the plant's portion of disconnection. From the station side, the load-shedding significantly impacts the STATCOM mode of operation, which needs to adapt to the net reactive power flow changes. The aim of performing this simulation is to validate the voltage control of the STATCOM, its performance, and current limits rating.

These simulations are carried out with the plant operating at nominal conditions after a long period. Therefore, steady state conditions are assumed: the grid has increased its excitation voltage, from 0.996 to 1.015 p.u., to supply the station at full load. This leads to a null net exchange of reactive power with the grid, unlike in the ramp-up sequence.

7.3.1 Partial Load Rejection

This study case shows the global behavior of the power plant under the load rejection of one station branch. In other words, when all MV breakers open simultaneously and affect all components downstream in a 33kV busbar, except for the capacitor banks. This load shedding represents a spontaneous loss of 121.5 MW and an injection into the grid of 98.8 MVAr, result of the deprivation of electrolyzer systems power consumption, but still production from the capacitor banks.

In Figure 7.7, one can notice that post-disturbance there is a slight positive generation of reactive power in the external grid. In steady state, the boost of excitation voltage to 1.015 p.u. compensated for the voltage drop in the grid's Thevenin impedance at full load without the need of STATCOM reactive power injection. Post-disturbance, the PCC voltage would be greater than 1 p.u. without reactive power flow, so it requires an additional voltage drop delivered by the external grid reactive power generation.

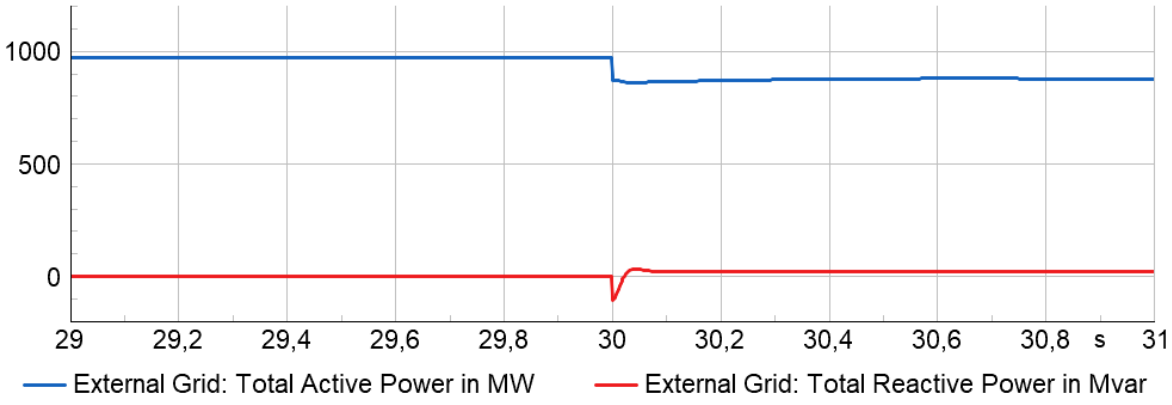

Figure 7.7: Power flow in the External Grid under partial load rejection

The STATCOM voltage control brings along the capacity to compensate disturbances in the PCC terminal, i.e. to mitigate a temporary overvoltage and bring it down to continuous operation limits (0.90-1.05 p.u.) [86] within few milliseconds. In this case, the injection of almost 100 MVAr into the grid causes a temporary overvoltage of 1.015 p.u. as illustrated in Figure 7.8.

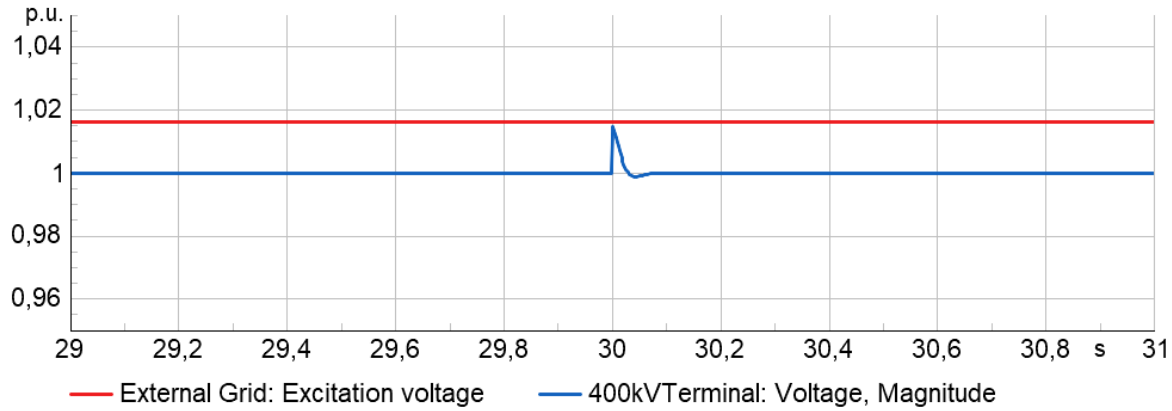

Figure 7.8: External Grid excitation voltage and PCC voltage under partial load rejection.

The STATCOM generation in steady state before the disturbance is 305.9 MVAr, same result as calculated in load flow analysis. To compensate for the generation surplus during the disturbance, the STATCOM system reduces its generation 110.9 MVAr as displayed in Figure 7.9. The STATCOM controller mitigates the disturbance within 50 ms manifesting a second order under-damped behavior.

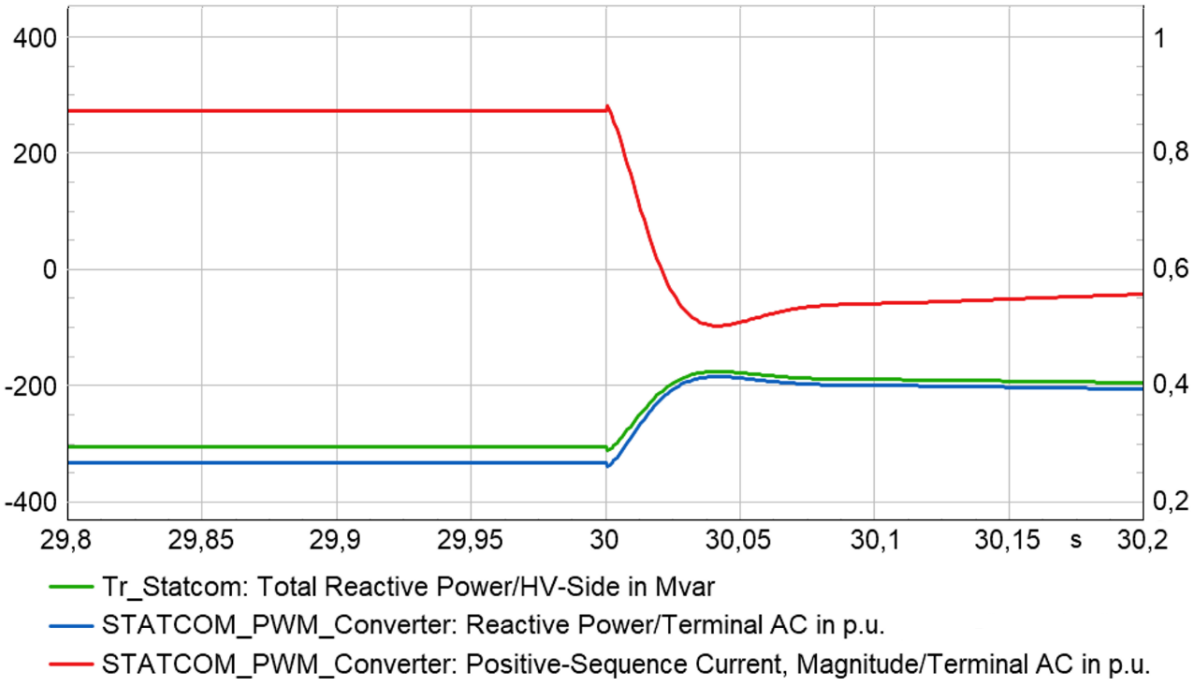

Figure 7.9: STATCOM load flow, current and voltage in p.u. under partial load rejection.

7.3.2 Full Load Rejection

A more severe case is the load rejection of the whole station. Two options were considered to carry away this analysis: opening simultaneously all HV breakers in the LV-side of the three-winding transformers, or opening all MV breakers downstream at 33kV busbars. Since the first case involves shedding all the electrolyzer systems and filters and in the second case only the electrolyzers, it was decided to proceed with option 2. This is the worst-case scenario: in the first one the STATCOM would need to shift from generating 305.9 MVAr down to zero, but in the other, to consume 358.3 MVAr instead.

This scenario produces the same behavior as the partial load rejection but on a larger scale. As presented in Figure 7.10, the peak of reactive power exchanged with the grid reaches above 800 MVAr during 6 ms, which causes a temporary overvoltage of 1.1 p.u. (440 kV). The disturbance is mitigated within 50 ms and the net reactive power flow exchange with the grid is brought down to 97.5 MVAr.

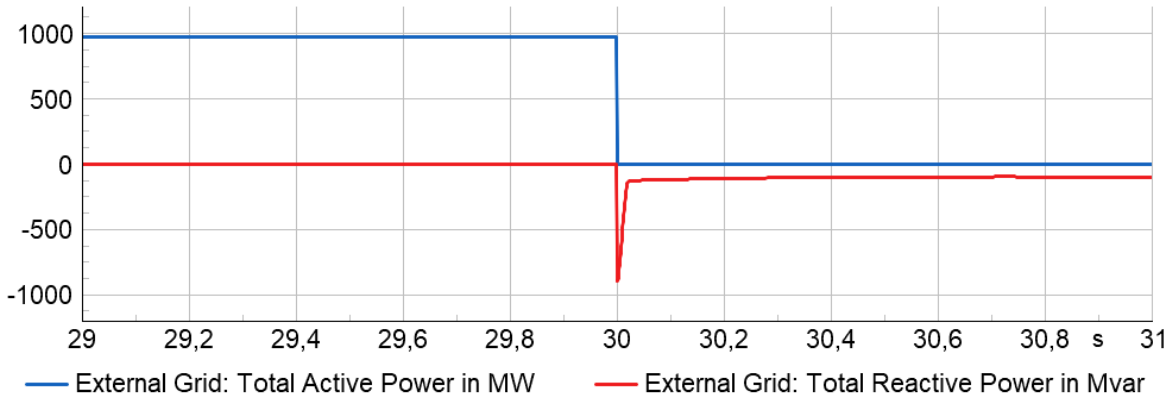

Figure 7.10: Power flow in the External Grid under total load rejection.

Unlike partial rejection, the system is unable to completely compensate for the reactive power produced by the capacitor banks, leaving a post-disturbance voltage of 1.02 p.u. (408 kV) illustrated in Figure 7.11. Therefore, some reactive power is injected into the grid. This situation is only temporary since the capacitor banks are switched off minutes after the event, as it corresponded to the no load scenario explained in the start-up sequence strategy.

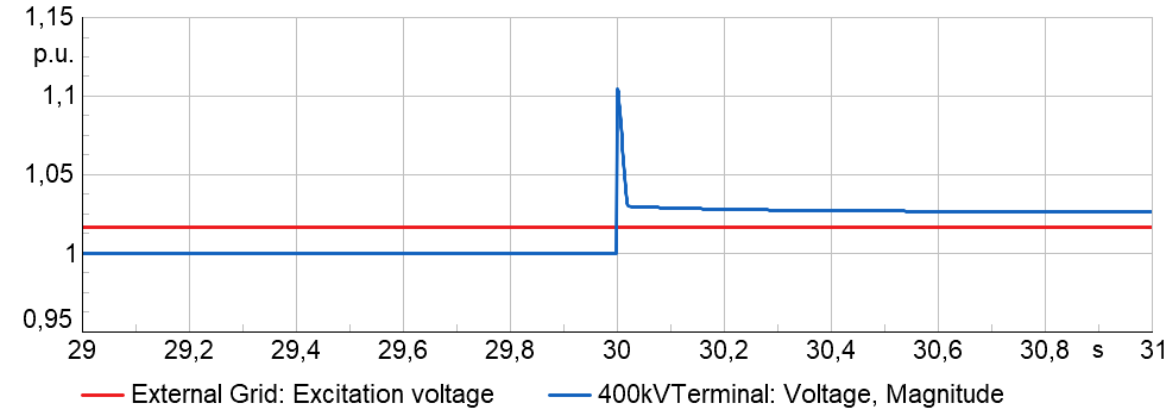

Figure 7.11: External Grid excitation voltage and PCC voltage under total load rejection.

In Figure 7.12, it is observed an immediate transition from capacitive to inductive mode in the STATCOM. During the first 3 ms after the disturbance there is an increase of reactive power production caused by the temporary overvoltage, reaching a maximum STATCOM production of 366.3 MVAr. The SVC reaches the current limit at this point providing 395 MVAr, above the limit of 385 MVAr calculated in Section 7.2, caused by the STATCOM LV-side increase to 1.2 p.u. The STATCOM inductive mode of operation reaches 358.3 MVAr post-disturbance, which translates into a SVC production of 320 MVAr, similar to the simplified limit calculated in Section 7.2.

With this last simulation, the station has been checked for the worst-case scenario, a very unlikely event given the nature of load rejection of only the electrolyzer systems, but not the filters. With this last simulation, it has been ensured the correct sizing of the electrical components inside the station.

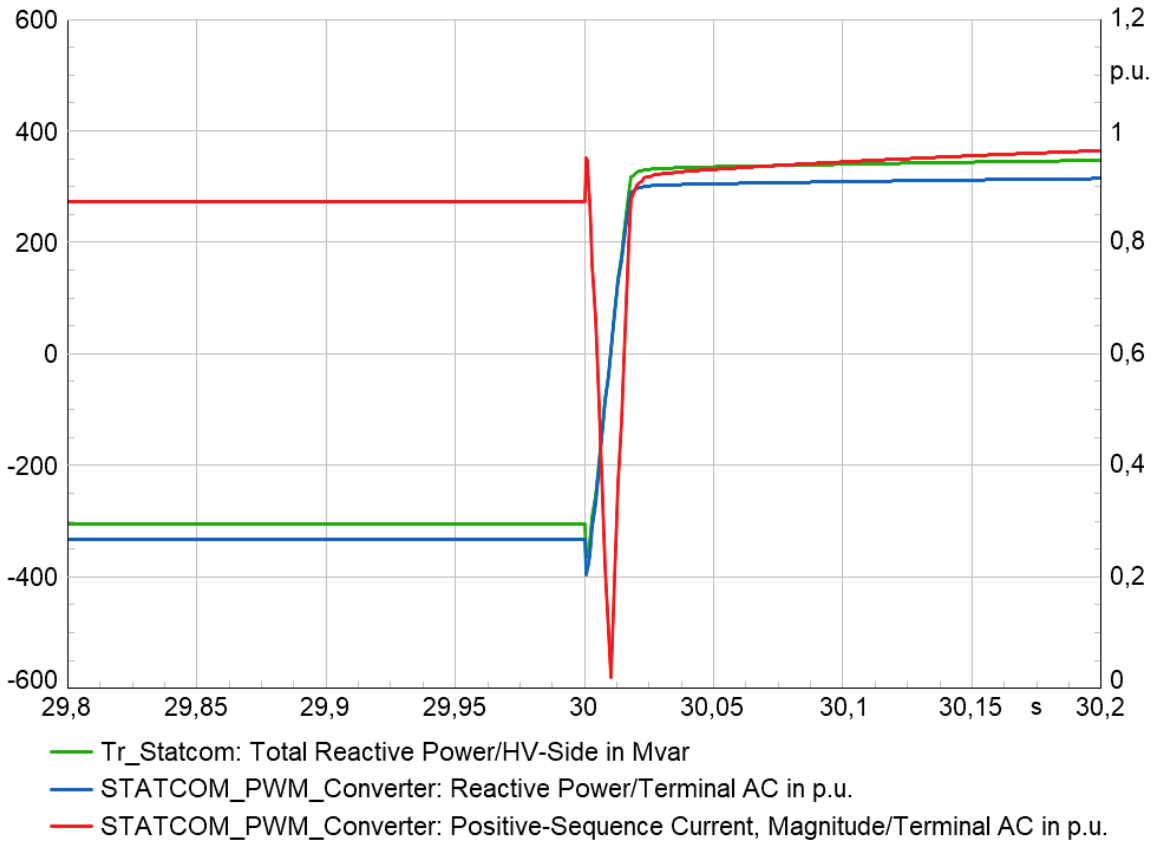

Figure 7.12: STATCOM load flow, current and voltage in p.u. under total load rejection.

8

Conclusions

8.1 Results from present work

The aim of the master thesis was to design and model a GW-scale electrolyzer station which resulted in a 972 MW station capable of producing 190 kt of H2 per annum at full capacity. Benchmarking between AWE and PEM proved PEM superiority in terms of performance and infrastructure. Nevertheless, AWE technology presented itself as a more suitable candidate given its significantly lower CAPEX and longer service lifetime, which led to its selection for model development.

The developed electrolyzer model holds a solid background in the scientific literature, based on the PHOEBUS demonstration plant, and properly scaled-up accordingly to Nel Energy Series A megawatt-level electrolyer stack. The plant design accounts for 64 A3880 modules and a reduction to 16 equivalent loads.

Electrolyzer model and converter controller were successfully designed to be easily replicable in future projects using look-up tables and a per unit controller. The controller design follows IMC methodology accordingly with the electrolyzer process model and validated through ramp-up simulation, giving insight into key differences between expected and simulated performance.

From different station designs, it was proposed a final candidate for further analysis. Electrical equipment and components employed in the plant have been rated to endure the station full loading scenario. This has been confirmed through steady state simulation (load flow analysis), as well as dynamic simulation (ramp-up and load rejection).

Grid code requirements stated for station design criteria was fulfilled through the implementation of filters and STATCOM. The harmonic boundaries were established following international electro-technical standards like IEEE Std 519 (2014) and IEC TR 61000-3-6, and its limits fulfilled with a 1.133% TDD for current, below 1.5%, and a 0.912% THD for voltage, below 3%.

An optimization method was proposed for reactive power distribution between the STATCOM and capacitor banks, reaching an optimum solution in terms of cost and performance. The STATCOM implementation enabled flexible reactive power supply and voltage regulation, with the capacitor banks supplying the bulk of reactive power demand. This strategy allowed the compliance in both power factor correction and voltage regulation grid code requirements. An additional advantage of this design was the downsized rating for the 400/33 kV transformers.

The ramp-up simulation demonstrated the effect of loading increase in neighborly electrolyzer systems due to the terminal voltage drop caused by increased reactive power consumption, as well as, the voltage dependence of both MV windings in the three-winding transformers. Finally, the introduction of the STATCOM enabled the management of voltage fluctuations to ensure a stable voltage supply under partial and total load rejection events and a disturbance handling within a 50 ms time span.

Overall, these steady state and dynamic simulations ensured adequate, safe, reliable and uninterruptible hydrogen supply at the same time grid code compliance was accomplished.

8.2 Future work

This thesis provides a solid base to evaluate large scale hydrogen plants. Nonetheless, further work is required to give a more complete scope, electrolyzer model and, evaluate the economic implications of electrical equipment selection. Further work can be classified in the next items:

Electrolyzer modelling

To commence, first idea in line would be to improve the electrolyzer model by implementing real data provided by the electrolyzer's manufacturer, instead of making assumptions about their catalogue products. Along this line, upgrading the model by integrating the thermal behavior and analyzing the evolution of the operating temperature during cold-start could proof interesting.

PowerFactory modelling

Analyzing the 12 PTR performing electromagnetic transient (EMT) simulation using PowerFactory or PSCAD softwares would prove beneficial for model verification. This study would be essential for the analysis on how the grid's Thevenin reactance and transformers leakage inductance affect the commutation angle in the 12-PTR as well as measuring the DC current ripple.

Station components modelling

Furthermore, a correct estimation of the short-circuit capacity S_k'' of the grid as well as the leakage inductance of the transformers is key to have correct dynamic simulations and short circuit analysis.

A valuable addition for plant design would be the introduction of magnetizing inductance inside transformers since this would have an added-value for an energization study of the station, station load flow calculation at low loading and harmonic analysis of the magnetizing current 3^{rd} harmonic introduction [87]. The implementation of Phase Shifting Transformers [88] between 400kV and 33kV is a useful low-order harmonic cancellation technique left unexplored.

Protection set-up

A noticeable study of the plant design left untouched is the protection coordination and switchgear selection, indispensable aspect for the safety and long-term lifespan of the station. Another interesting add to the station plant would be the incorporation of surge

arresters at 33kV busbars to protect the transformers and capacitor banks against temporary overvoltages.

Economic evaluation

Ancillary services like frequency reserve and interruptible service as demand management tool for the TSO could add system security to the grid and economical benefits for the hydrogen plant [89].

Evidently, an economical evaluation would have to be done of STATCOM along with cost considerations for passive filters per MVAr to determine the optimal distribution of reactive power in economic terms, while fulfilling the technical feasibility and complying with overall requirements.

Medium voltage DC distribution grid

Finally, a plant model connected to a MVDC grid would also add valuable information, as well as implementing PEM electrolyzers to harness wind curtailments and intermittent power flows due to renewable power supply. This would be followed by a cross comparison of HVAC and MVDC plant structure, their advantages respect to number of components and an anticipated total investment cost evaluation for further analysis.

Grid code compliance

Lastly the station should be capable of operating within a PCC voltage range. Swedish Energy Markets Inspectorate's statute book [86] stipulates that consumption units shall be capable of continuous operation within the voltage range 0.90-1.05 p.u. and operation for at least 60 minutes in the voltage range 1.05-1.10 p.u. which could imply the introduction of tap-changers in the 400/33kV transformers.

Bibliography

[1] 'Climate Change 'Biggest Threat Modern Humans Have Ever Faced', World-Renowned Naturalist Tells Security Council, Calls for Greater Global Cooperation,' *United Nations*, Feb. 2021. [Online]. Available: https://press.un.org/en/2021/sc14445.doc.htm (visited on 27/02/2023).

[2] 'United Nations Conference on the human environment, Stockholm 1972,' *United Nations*, [Online]. Available: https://www.un.org/en/conferences/environment/stockholm1972 (visited on 27/02/2023).

[3] Britannica, The Editors of Encyclopaedia, 'Kyoto protocol,' *Encyclopedia Britannica*, Sep. 2022. [Online]. Available: https://www.britannica.com/event/Kyoto-Protocol (visited on 27/02/2023).

[4] G. Rannard, 'ExxonMobil: Oil giant predicted climate change in 1970s - scientists,' *BBC News*, Jan. 2023. [Online]. Available: https://www.bbc.com/news/science-environment-64241994 (visited on 27/02/2023).

[5] G. Supran and N. Oreskes, 'Assessing ExxonMobil's Climate Change Communications (1977–2014),' *Environmental Research Letters*, vol. 12, no. 8, p. 084 019, 2017. DOI: 10.1088/1748-9326/aa815f.

[6] 'The Paris Agreement,' *United Nations*, [Online]. Available: https://www.un.org/en/climatechange/paris-agreement (visited on 27/02/2023).

[7] M. McGrath, 'Climate change: US formally withdraws from Paris Agreement,' *BBC News*, Nov. 2020. [Online]. Available: https://www.bbc.com/news/science-environment-54797743 (visited on 27/02/2023).

[8] 'The United States officially rejoins the Paris Agreement - United States Department of State,' *U.S. Department of State*, Feb. 2021. [Online]. Available: https://www.state.gov/the-united-states-officially-rejoins-the-paris-agreement/ (visited on 27/02/2023).

[9] 'COVID-19 caused only a temporary reduction in carbon emissions – UN report,' *UN Environment*, Sep. 2021. [Online]. Available: https://www.unep.org/news-and-stories/press-release/covid-19-caused-only-temporary-reduction-carbon-emissions-un-report (visited on 27/02/2023).

[10] J. Tollefson, 'What the war in Ukraine means for energy, climate and food,' *Nature*, vol. 604, no. 7905, pp. 232–233, 2022. DOI: 10.1038/d41586-022-00969-9.

[11] K. Ng, 'China's population falls for first time since 1961,' *BBC News*, Jan. 2023. [Online]. Available: https://www.bbc.com/news/world-asia-china-64300190 (visited on 27/02/2023).

[12] L. Silver, C. Huang and L. Clancy, 'Key facts as India surpasses China as the world's most populous country,' *Pew Research Center*, Feb. 2023. [Online]. Available: https://www.pewresearch.org/fact-tank/2023/02/09/key-facts-as-india-surpasses-china-as-the-worlds-most-populous-country/ (visited on 27/02/2023).

[13] IEA, 'World Energy Outlook 2022,' IEA, Paris, Tech. Rep. [Online]. Available: https://www.iea.org/reports/world-energy-outlook-2022.

[14] IEA, 'Global Energy-Related CO2 Emissions by Sector,' IEA, Paris, Tech. Rep. [Online]. Available: https://www.iea.org/data-and-statistics/charts/global-energy-related-co2-emissions-by-sector.

[15] IEA, 'Direct CO2 emissions from industry in the Net Zero Scenario, 2000-2030,' IEA, Paris, Tech. Rep. [Online]. Available: https://www.iea.org/data-and-statistics/charts/direct-co2-emissions-from-industry-in-the-net-zero-scenario-2000-2030.

[16] IEA, 'Global hydrogen demand by sector in the Net Zero Scenario, 2019-2030,' IEA, Paris, Tech. Rep. [Online]. Available: https://www.iea.org/data-and-statistics/charts/global-hydrogen-demand-by-sector-in-the-net-zero-scenario-2019-2030.

[17] IEA, 'Global Hydrogen Review 2022,' IEA, Paris, Tech. Rep. [Online]. Available: https://www.iea.org/reports/global-hydrogen-review-2022.

[18] T. DiChristopher, 'Experts explain why green hydrogen costs have fallen and will keep falling,' *S&P Global Homepage*, Mar. 2021. [Online]. Available: https://www.spglobal.com/marketintelligence/en/news-insights/latest-news-headlines/experts-explain-why-green-hydrogen-costs-have-fallen-and-will-keep-falling-63037203.

[19] E. Commission, 'A hydrogen strategy for a climate-neutral Europe,' European Commission, Brussels, Tech. Rep., Jul. 2020. [Online]. Available: https://eur-lex.europa.eu/legal-content/EN/TXT/?uri=CELEX%5C%3A52020DC0301.

[20] J. Favas, E. Monteiro and A. Rouboa, 'Hydrogen production using plasma gasification with steam injection,' *International Journal of Hydrogen Energy*, vol. 42, no. 16, pp. 10 997–11 005, 2017. DOI: 10.1016/j.ijhydene.2017.03.109.

[21] Nuclear Energy Agency, 'High-temperature Gas-cooled Reactors and Industrial Heat Applications,' OECD Publishing, Paris, Tech. Rep., 2022. [Online]. Available: https://www.oecd-nea.org/jcms/pl_20497/high-temperature-gas-cooled-reactors.

[22] IRENA, 'Global hydrogen trade to meet the 1.5°C climate goal: Part I – Trade outlook for 2050 and way forward,' International Renewable Energy Agency, Abu Dhabi, Tech. Rep., 2022. [Online]. Available: https://prod-cd.irena.org/-/media/Files/IRENA/Agency/Publication/2022/Jul/IRENA_Global_hydrogen_trade_part_1_2022_.pdf?rev=f70cfbdcf3d34b40bc256383f54dbe73.

[23] H. Central, 'Green Hydrogen: Technology Breakthroughs Mean Iridium Shortage and High Prices will Ease in 2023 – Rystad Energy,' Feb. 2023. [Online]. Available: https://hydrogen-central.com/green-hydrogen-technology-breakthroughs-mean-iridium-shortage-and-high-prices-will-ease-in-2023-rystad-energy/.

[24] IEEFA, 'Sinopec building world's largest green hydrogen plant in China,' *Balkan Green Energy News*, Aug. 2022. [Online]. Available: https://ieefa.org/articles/sinopec-building-worlds-largest-green-hydrogen-plant-china.

[25] S. Matalucci, 'The Hydrogen Stream: World's largest electrolyzer to be deployed in Norway,' *Pv Magazine International*, Sep. 2022. [Online]. Available: https://www.pv-magazine.com/2022/09/13/the-hydrogen-stream-worlds-largest-electrolyzer-to-be-deployed-in-norway/.

[26] M. Minutillo, A. Perna, A. Forcina, S. Di Micco and E. Jannelli, 'Analyzing the levelized cost of hydrogen in refueling stations with on-site hydrogen production via water electrolysis in the Italian scenario,' *International Journal of Hydrogen Energy*, vol. 46, no. 26, pp. 13 667–13 677, 2021. DOI: 10.1016/j.ijhydene.2020.11.110.

[27] W. E. Forum, 'How many jobs could the clean energy transition create?' *World Economic Forum*, [Online]. Available: https://www.weforum.org/agenda/2022/03/the-clean-energy-employment-shift-by-2030/.

[28] Stiftelsen for industriell og teknisk forskning (SINTEF), 'Norwegian Energy Road Map 2050,' *SINTEF*, [Online]. Available: https://www.sintef.no/en/projects/2016/energymap/.

[29] K. Espegren, S. Damman, P. Pisciella, I. Graabak and A. Tomasgard, 'The role of hydrogen in the transition from a petroleum economy to a low-carbon society,' *International Journal of Hydrogen Energy*, vol. 46, no. 45, pp. 23 125–23 138, 2021. DOI: 10.1016/j.ijhydene.2021.04.143.

[30] 'Water,' *United Nations*, [Online]. Available: https://www.un.org/en/global-issues/water.

[31] 'Water Resource Considerations for the Hydrogen Economy,' *JD Supra*, Dec. 2020. [Online]. Available: https://www.jdsupra.com/legalnews/water-resource-considerations-for-the-84603/.

[32] Ministry of Energy, Government of Chile, 'National Green Hydrogen Strategy,' Tech. Rep., Nov. 2020. [Online]. Available: https://energia.gob.cl/sites/default/files/national_green_hydrogen_strategy_-_chile.pdf.

[33] E. Phiddian, 'Taking the precious metals out of hydrogen electrolysis,' *Cosmos*, Feb. 2022. [Online]. Available: https://cosmosmagazine.com/science/chemistry/hydrogen-electrolysis-precious-metals-catalyst/.

[34] A. Li *et al.*, 'Enhancing the stability of cobalt spinel oxide towards sustainable oxygen evolution in acid,' *Nature Catalysis*, vol. 5, no. 2, pp. 109–118, Feb. 2022. DOI: 10.1038/s41929-021-00732-9.

[35] U.S. Department of Energy, 'Safe use of hydrogen,' [Online]. Available: https://www.energy.gov/eere/fuelcells/safe-use-hydrogen.

[36] 'Hydrogen incident examples,' *Hydrogen Tools*, Mar. 2020. [Online]. Available: https://h2tools.org/lessons/hydrogen-incident-examples.

[37] S. S. Kumar and H. Lim, 'An overview of water electrolysis technologies for green hydrogen production,' *Energy reports*, vol. 8, pp. 13 793–13 813, 2022. DOI: https://doi.org/10.1016/j.egyr.2022.10.127.

[38] IRENA, 'Green Hydrogen Cost Reduction: Scaling up Electrolysers to Meet the 1.5ºC Climate Goal,' *Abu Dhabi: International Renewable Energy Agency*, 2020.

[39] O. Posdziech, 'Production of renewable hydrogen and syngas via high-temperature electrolysis,' *Sunfire GmbH*, Mar. 2021. [Online]. Available: https://multiplhy-project.eu/Documents/Workshop%20on%20Advanced%20PtG%20and%20PtL%20Technologies%20High-Temperature%20Electrolysis_Posdziech.pdf.

[40] T. Smolinka, H. Bergmann, J. Garche and M. Kusnezoff, 'Chapter 4 - the history of water electrolysis from its beginnings to the present,' in *Electrochemical power sources: fundamentals, systems, and applications*, Elsevier, 2022, pp. 83–164. DOI: https://doi.org/10.1016/B978-0-12-819424-9.00010-0. [Online]. Available: https://www.sciencedirect.com/science/article/pii/B9780128194249000100.

[41] R. Gilliam, J. Graydon, D. Kirk and S. Thorpe, 'A review of specific conductivities of potassium hydroxide solutions for various concentrations and temperatures,' *International Journal of Hydrogen Energy*, vol. 32, no. 3, pp. 359–364, 2007.

[42] M. Schalenbach, G. Tjarks, M. Carmo, W. Lueke, M. Mueller and D. Stolten, 'Acidic or alkaline? towards a new perspective on the efficiency of water electrolysis,' *Journal of The Electrochemical Society*, vol. 163, no. 11, F3197–F3208, 2016. DOI: 10.1149/2.0271611jes.

[43] O. Ulleberg, 'Modeling of advanced alkaline electrolyzers: A system simulation approach,' *International Journal of Hydrogen Energy*, vol. 28, no. 1, pp. 21–33, 2003. DOI: 10.1016/s0360-3199(02)00033-2.

[44] 'Nel hydrogen electrolyzer,' *Nel Hydrogen*, [Online]. Available: https://nelhydrogen.com/water-electrolysers-hydrogen-generators/ (visited on 04/04/2023).

[45] 'Nafion™ Sulfonic Membranes,' [Online]. Available: https://www.nafion.com/en/products/sulfonic-membranes (visited on 15/01/2024).

[46] O. Schmidt, A. Gambhir, I. Staffell, A. Hawkes, J. Nelson and S. Few, 'Future cost and performance of water electrolysis: An expert elicitation study,' *International journal of hydrogen energy*, vol. 42, no. 52, pp. 30 470–30 492, 2017. DOI: https://doi.org/10.1016/j.ijhydene.2017.10.045.

[47] 'Metal Spot Price Charts Iridium Price (USD / Gram) Chart for the Last Year,' *Daily Metal Prices*, [Online]. Available: https://www.dailymetalprice.com/metalpricecharts.php?c=ir&u=oz&d=10 (visited on 16/08/2023).

[48] 'Iberdrola commissions the largest green hydrogen plant for industrial use in Europe,' *Iberdrola*, [Online]. Available: https://www.iberdrola.com/about-us/what-we-do/green-hydrogen/puertollano-green-hydrogen-plant (visited on 18/08/2023).

[49] A. Hodges *et al.*, 'A high-performance capillary-fed electrolysis cell promises more cost-competitive renewable hydrogen,' *Nature communications*, vol. 13, no. 1, p. 11, Mar. 2022.

[50] 'Breakthrough opens door to low-cost green hydrogen,' *University of Wollongong (UOW)*, Mar. 2022. [Online]. Available: https://www.uow.edu.au/media/2022/breakthrough-opens-door-to-low-cost-green-hydrogen.php.

[51] I. Dincer and A. A. AlZahrani, '4.25 Electrolyzers,' in *Comprehensive Energy Systems*, I. Dincer, Ed., Oxford: Elsevier, 2018, pp. 985–1025. DOI: https://doi.org/10.1016/B978-0-12-809597-3.00442-9. [Online]. Available: https://www.sciencedirect.com/science/article/pii/B9780128095973004429.

[52] M. Mori, T. Mržljak, B. Drobnič and M. Sekavčnik, 'Integral Characteristics of Hydrogen Production in Alkaline Electrolysers,' *Strojniški vestnik-Journal of Mechanical Engineering*, vol. 59, no. 10, pp. 585–594, 2013.

[53] M. Hammoudi, C. Henao, K. Agbossou, Y. Dubé and M. Doumbia, 'New multi-physics approach for modelling and design of alkaline electrolyzers,' *International Journal of Hydrogen Energy*, vol. 37, no. 19, pp. 13 895–13 913, 2012.

[54] T. Adibi, A. Sojoudi and S. C. Saha, 'Modeling of thermal performance of a commercial alkaline electrolyzer supplied with various electrical currents,' *International Journal of Thermofluids*, vol. 13, pp. 100–126, 2022.

[55] 'Thermophysical properties of fluid systems,' *NIST Standard Reference Database*, [Online]. Available: `http://webbook.nist.gov/chemistry/fluid/` (visited on 27/03/2023).

[56] T. Dervišić and C. Engström, 'Electric infrastructure for electrolyser systems. Design proposals for AC and DC distribution systems,' M.S. thesis, Chalmers University of Technology, Göteborg, Sweden, 2021. [Online]. Available: `https://hdl.handle.net/20.500.12380/302627`.

[57] J. Kotowicz, M. Jurczyk, D. Węcel and W. Ogulewicz, 'Analysis of hydrogen production in alkaline electrolyzers,' *Journal of Power Technologies*, vol. 96, no. 3, pp. 149–156, 2016. (visited on 12/05/2023).

[58] 'Flow meters for hydrogen applications,' *Bronkhorst*, [Online]. Available: `https://www.bronkhorst.com/int/markets/renewable-energy/hydrogen/` (visited on 12/05/2023).

[59] B. Bensmann, R. Hanke-Rauschenbach and K. Sundmacher, 'In-situ measurement of hydrogen crossover in polymer electrolyte membrane water electrolysis,' *International journal of hydrogen energy*, vol. 39, no. 1, pp. 49–53, 2014.

[60] J. Divisek, J. Mergel and H. Schmitz, 'Advanced water electrolysis and catalyst stability under discontinuous operation,' *International journal of hydrogen energy*, vol. 15, no. 2, pp. 105–114, 1990.

[61] W. Hug, J. Divisek, J. Mergel, W. Seeger and H. Steeb, 'Highly efficient advanced alkaline electrolyzer for solar operation,' *International journal of hydrogen energy*, vol. 17, no. 9, pp. 699–705, 1992.

[62] I. D. de Cerio Mendaza, B. Bak-Jensen and Z. Chen, 'Alkaline electrolyzer and V2G system DIgSILENT models for demand response analysis in future distribution networks,' *2013 IEEE Grenoble Conference*, 2013. DOI: `10.1109/ptc.2013.6652429`.

[63] P. Ghosh, B. Emonts, H. Janßen, J. Mergel and D. Stolten, 'Ten years of operational experience with a hydrogen-based renewable energy supply system,' *Solar Energy*, vol. 75, no. 6, pp. 469–478, 2003.

[64] 'Electrolyzer market size, share and industry analysis, by type (traditional alkaline electrolyzer, pem electrolyzer), by application (power plants, steel plant, electronics and photovoltaics, industrial gases, energy storage or fueling for fcevs, power to gas, others), and regional forecast, 2024-2032,' *Fortune Business Insights*, 2024. [Online]. Available: `https://www.fortunebusinessinsights.com/electrolyzer-market-103919`.

[65] M. K. Gustafson, 'A computational approach to simulating the performance of a 24-hour solar-fuel cell-hydrogen electric power plant,' M.S. thesis, Wright State University, May 2013.

[66] F. Gonzalez-Longatt and J. L. Rueda Torres, *Modelling and simulation of power electronic converter dominated power systems in PowerFactory*. Springer Nature, 2021.

[67] M. Beza, *ENM061 - Power Electronic Converters*, Lecture Notes, Chalmers University of Technology, Dept. Elect. Eng., 2022.

[68] B. Yodwong, D. Guilbert, M. Phattanasak, W. Kaewmanee, M. Hinaje and G. Vitale, 'AC-DC Converters for Electrolyzer Applications: State of the Art and Future Challenges,' *Electronics 2020*, vol. 9, no. 6, May 2020. DOI: 10.3390/electronics9060912. [Online]. Available: https://www.mdpi.com/2079-9292/9/6/912.

[69] 'A One-GigaWatt Green-Hydrogen Plant Advanced Design and Total Installed-Capital Costs,' *Hydrohub Innovation Program*, [Online]. Available: https://ispt.eu/projects/hydrohub-gigawatt/ (visited on 04/10/2023).

[70] M. Chen, S.-F. Chou, F. Blaabjerg and P. Davari, 'Overview of Power Electronic Converter Topologies Enabling Large-Scale Hydrogen Production via Water Electrolysis,' *Applied Sciences*, vol. 12, p. 1906, Feb. 2022. DOI: 10.3390/app12041906.

[71] N. Mohan, T. M. Undeland and W. P. Robbins, *Power electronics: converters, applications and design*. John Wiley & Sons, 2003.

[72] Hitachi Energy, *Private communication, Hitachi Energy*, 2023.

[73] S. Lundberg, *ENM076 - Electric Drive Systems*, Lecture Notes, Chalmers University of Technology, Dept. Elect. Eng., 2022.

[74] 'IEEE Recommended Practice for Excitation System Models for Power System Stability Studies,' *IEEE Std 421.5-2016 (Revision of IEEE Std 421.5-2005)*, pp. 1–207, 2016. DOI: 10.1109/IEEESTD.2016.7553421.

[75] 'Commission Regulation (EU) 2016/1388 of 17 August 2016 Establishing a Network Code on Demand Connection,' [Online]. Available: https://eur-lex.europa.eu/eli/reg/2016/1388/oj (visited on 05/10/2023).

[76] 'IEEE Recommended Practice and Requirements for Harmonic Control in Electric Power Systems,' *IEEE Std 519-2014 (Revision of IEEE Std 519-1992)*, pp. 1–29, Jun. 2014. DOI: 10.1109/IEEESTD.2014.6826459.

[77] 'Electromagnetic compatibility (EMC) - Part 3-6: Limits - Assessment of emission limits for the connection of distorting installations to MV, HV and EHV power systems,' International Electrotechnical Commission, Tech. Rep. IEC TR 61000-3-6:2008, Feb. 2008.

[78] D. J. Meisner, B. Niemann, M. Shevchenko, E. Fombang, I. Khosravi and H. von Geymüller, 'STATCOM with Active Filter Using STATCOM as Active Filter, Improving Power Quality and reducing Harmonics,' pp. 1–5, 2020. DOI: 10.1109/TD39804.2020.9299900.

[79] M. Bongiorno, *ENM100 - Power Electronic Solutions for Power Systems*, Lecture Notes, Chalmers University of Technology, Dept. Elect. Eng., 2022.

[80] L. Morán, J. Dixon and M. Torres, '41 - Active Power Filters,' in *Power Electronics Handbook (Fourth Edition)*, M. H. Rashid, Ed., Fourth Edition, Butterworth-Heinemann, 2018, pp. 1341–1379. DOI: https://doi.org/10.1016/B978-0-12-811407-0.00046-5. [Online]. Available: https://www.sciencedirect.com/science/article/pii/B9780128114070000465.

[81] 'Harmonic filters charm,' *Hitachi Energy*, [Online]. Available: https://www.hitachienergy.com/products-and-solutions/capacitors-and-filters/high-voltage-capacitors-and-filters/harmonic-filters (visited on 05/06/2023).

[82] 'Metal enclosed capacitor banks ABBACUS,' *Hitachi Energy*, [Online]. Available: https://www.hitachienergy.com/products-and-solutions/capacitors-and-filters/medium-voltage-capacitors-and-filters/capacitor-banks/metal-enclosed-capacitor-banks-abbacus (visited on 20/08/2023).

[83] J. Solanki, N. Fröhleke and J. Böcker, 'Implementation of Hybrid Filter for 12-Pulse Thyristor Rectifier Supplying High-Current Variable-Voltage DC Load,' *IEEE Transactions on Industrial Electronics*, vol. 62, no. 8, pp. 4691–4701, 2015. DOI: 10.1109/TIE.2015.2393833.

[84] V. Azbe and R. Mihalic, 'Statcom control strategies in energy-function-based methods for the globally optimal control of renewable sources during transients,' *International Journal of Electrical Power & Energy Systems*, vol. 141, pp. 108–145, 2022. DOI: https://doi.org/10.1016/j.ijepes.2022.108145. [Online]. Available: https://www.sciencedirect.com/science/article/pii/S0142061522001843.

[85] R. Heydari *et al.*, 'Grid-Forming Control for STATCOMs – a Robust Solution for Networks with a High Share of Inverter-Based Resources,' *CIGRE*, pp. 1–11, 2022. [Online]. Available: https://www.e-cigre.org/publications/detail/c4-10822-2022-grid-forming-control-for-statcoms-a-robust-solution-for-networks-with-a-high-share-of-inverter-based-resources.html.

[86] S. Kraftnät, 'Energimarknadsinspektionens föreskrifter om fastställande av generellt tillämpliga krav för anslutning av förbrukare,' [Online]. Available: https://www.ei.se/om-oss/publikationer/publikationer/foreskrifter-el/2019/foreskrift-eifs-20196 (visited on 05/10/2023).

[87] L. Mari, 'Magnetizing and Exciting Currents Waveshapes in Transformers,' *EEPower*, Jul. 2020. [Online]. Available: https://eepower.com/technical-articles/magnetizing-and-exciting-currents-waveshapes-in-transformers/# (visited on 30/08/2023).

[88] 'Phase-shifting transformers (PST),' [Online]. Available: https://www.hitachienergy.com/products-and-solutions/transformers/power-transformers/system-intertie-transformers/phase-shifting-transformers (visited on 30/08/2023).

[89] 'Interruptibility Service,' *Red Eléctrica*, [Online]. Available: https://www.ree.es/en/activities/operation-of-the-electricity-system/interruptibility-service#:~:text=Interruptibility%20Service%20Interruptibility%20service%20is%20a%20demand%20management,%28system%20security%29%20and%20economic%20criteria%20%28reducing%20system%20costs%29. (visited on 30/08/2023).

DEPARTMENT OF ELECTRICAL ENGINEERING
CHALMERS UNIVERSITY OF TECHNOLOGY
Gothenburg, Sweden
www.chalmers.se

CHALMERS
UNIVERSITY OF TECHNOLOGY